Graduate thesis

NTNU
Norwegian University of Science and Technology
Faculty of Natural Sciences
Department of Materials Science and Engineering

Egil Ytterli Tokle

Nano-Engineering for Functional Ferroelectric Domain Walls

Graduate thesis in Nanotechnology
Supervisor: Dennis Meier
Co-supervisor: Leonie Richarz
June 2024

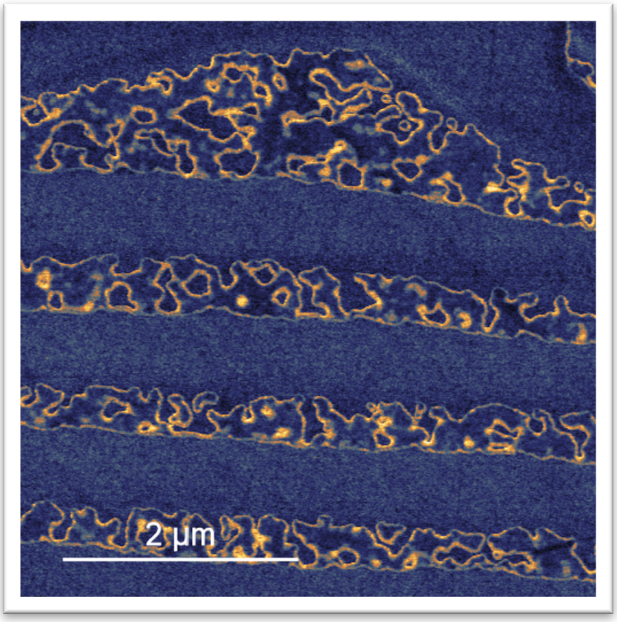

NTNU
Norwegian University of
Science and Technology

Egil Ytterli Tokle

Nano-Engineering for Functional Ferroelectric Domain Walls

Graduate thesis in Nanotechnology
Supervisor: Dennis Meier
Co-supervisor: Leonie Richarz
June 2024

Norwegian University of Science and Technology
Faculty of Natural Sciences
Department of Materials Science and Engineering

NTNU
Norwegian University of
Science and Technology

Preface

This master's thesis was written as a conclusion to the *five-year Integrated Master's Degree in Nanotechnology* study programme at the Norwegian University of Science and Technology (NTNU). The work was conducted at the Functional Materials and Materials Chemistry group (FACET), in the Functional Topological Systems subgroup (FUNTOPS).

Acknowledgements

First and foremost, I express my deepest gratitude to my supervisors for this project, Prof. Dr. Dennis Meier and Leonie Richarz. Both have provided valuable discussion and feedback, which have greatly contributed to the work. Thanks to Dennis, who welcomed me to the group, and gave me the opportunity to work hands-on in the fascinating field of ferroelectrics and topological defects. I am really glad to have been encouraged to participate and present my work at international conferences. To my co-supervisor Leonie, I am forever grateful for all the support throughout the year, and for always answering my questions, however basic they may be. Dennis and Leonie have been happy to share from their extensive knowledge in the field, and without their excellent guidance, the this master's thesis would not have been possible.

There are other people who deserve thanks for helping me through the course of this project. Special thanks go to Ruben Dragland, who has helped me perform PFM measurements, and to Ivan Ushakov and Dr. Jiali He for being available when I have encountered problems in the lab. I would also like to thank Jiali for letting me borrow her old data to demonstrate the domain structure in $ErMnO_3$. I am grateful to the engineers at IMA, including Pei Na Kui and Andrey Kosinskiy. Many thanks go to the people in FACET for providing critical questions and feedback after presentations at the weekly ferromeetings. I would also like to give thanks to Zewu Yan and Edith Bourret for making the samples that I have used throughout the year.

Finally, I have to thank my classmates and our student organization, Timini, for making these five years the amazing journey it has been.

Egil Ytterli Tokle
June 14, 2024

Abstract

For over a decade, ferroelectric domain walls have attracted substantial attention and played a key role in the search for innovative systems for future nanotechnology, motivated by the unique properties that arise in such confined areas. Particularly, the local conductance at the domain walls is of special interest, as it has shown that it can exceed that of the surrounding bulk by several orders of magnitude. In the improper ferroelectric hexagonal manganites ($R\mathrm{MnO}_3$, R = Sc, Y, In, Dy-Lu), the conductance in nominally neutral domain walls correlates with the oxygen off-stoichiometry of the system, and can be enhanced by annealing in a reductive atmosphere, *e.g.* N_2 gas.

This master's thesis investigates this annealing process, using $\mathrm{Er(Mn,Ti)O_3}$ as a model system, by systematically varying the annealing temperature and dwell time. Conductive atomic force microscopy (cAFM) was used to monitor both immediate and long-term effects of annealing. A critical annealing temperature was identified in the range between 200 °C and 300 °C required for conductive domain walls to develop. Advanced annealing experiments revealed the re-exposition to ambient air to be a crucial point in the development of domain wall conductance, indicating that the conductance emerges together with a local reoxidation at the domain walls.

Additionally, I report the observation of nanoscale bubble domains in $\mathrm{Er(Mn,Ti)O_3}$, which form during self-poling of the polarization due to a charge concentration gradient. These bubble domains present similarities to polar skyrmions in proper ferroelectrics and are metastable and manipulable by electric fields. Comparing regions subjected to external electric fields to unaffected regions reveals a memristive behavior of the bubble domains, where the spatial extent and time perspective of the applied electric fields is recorded in the density of bubble domains. The disappearance of bubble domains highlights the mobility of oxygen interstitials in hexagonal manganites, corroborating previous theoretical predictions of defect stability within neutral domain walls.

The results provide new insights into the microscopic mechanisms of the domain wall conductance and will constitute a part of an intricate line of research to give detailed guidelines for property engineering for the further development of domain wall nanotechnology.

Samandrag

I over eit tiår har ferroelektriske domenveggar fått stor merksemd i søket etter nyskapande system for framtidig nanoteknologi grunna i dei unike eigenskapane som oppstår i slike avgrensa område. Særleg er den lokale leieevna i domenveggane av spesiell interesse, då ho har vist seg å kunne overstige den i det omliggjande materialet med fleire storleiksordenar. I dei uekte ferroelektriske heksagonale manganittane (RMnO$_3$, R = Sc, Y, In, Dy-Lu) samsvarar leieevna i formelt nøytrale domenveggar med oksygenustøkiometrien til systemet, og kan aukast ved gløding i reduserande atmosfærar, som til dømes nitrogengass.

Denne masteroppgåva undersøkjer denne glødeprosessen med Er(Mn, Ti)O$_3$ som modellsystem ved å systematisk variere den gjeldande glødetemperaturen og -tida. Leiande atomærkraftmikroskopi (cAFM) er nytta for å analysere både umiddelbare og langvarige effektar av gløding. Ein kritisk glødetemperatur for å framkalle leiande domenveggar vart identifisert til å liggje mellom 200 °C og 300 °C. Avanserte glødeeksperiment viste at augeblinken materialet kjem i kontakt med oksygenhaldig luft er avgjerande for å fremje leiande domenveggar, noko som tyder på at leieevna kjem fram i takt med gjenoksidering lokalt i domeneveggane.

I tillegg rapporterer eg observasjonen av nanoskala bobledomene i Er(Mn, Ti)O$_3$, som dannar seg når materialet polar seg sjølv frå ein gradient i konsentrasjonen av ladningar. Desse bobledomena kan samanliknast med polare skyrmion i ekte ferroelektrika, og er metastabile og manipulerbare med eksterne elektriske felt. Ved å samanlikne område med og utan påverknad frå eksterne felt viser eg ein memristiv åtferd i bobledomena, der den romlege utstrekninga og tidsperspektivet til feltet er registrert i tettleiken av bobledomene. Forløysninga av desse bobledomena understrekar mobiliteten til oksygeninterstitialar i heksagonale manganittar, og støttar føregåande teoretiske utrekningar om auka defektstabilitet i nøytrale domenveggar.

Resultata gjev nytt innsyn i dei underliggjande mikroskopiske mekanismane bak elektrisk leiing i domenveggane, og utgjer ein del av ein omfattande rekkje forskingsprosjekt for å finne detaljerte retningslinjer for utforming av funksjonelle eigenskapar for vidare utvikling av domenveggbasert nanoteknologi.

Contents

Contents **vii**

1 Introduction **1**
- 1.1 Aim of Work . . . 2
- 1.2 Structure of the Thesis . . . 3

2 Theoretical Background **5**
- 2.1 Ferroelectrics . . . 5
- 2.2 Ferroelectric Domains and Domain Walls . . . 8
  - 2.2.1 Origin of Domains . . . 8
  - 2.2.2 Domain Walls . . . 10
  - 2.2.3 Conduction Mechanisms in Ferroelectric Domain Walls 11
- 2.3 Hexagonal Manganites . . . 12
- 2.4 Defects in Crystalline Materials . . . 16
  - 2.4.1 Point Defects . . . 16
  - 2.4.2 Oxygen Defects in Hexagonal Manganites . . . 18

3 Scanning Probe Microscopy **21**
- 3.1 Atomic Force Microscopy . . . 22
- 3.2 Piezoresponse Force Microscopy . . . 23
- 3.3 Conductive Atomic Force Microscopy . . . 24
  - 3.3.1 Artifacts in cAFM imaging . . . 25
- 3.4 Imaging of Ferroelectric Domains in Er(Mn, Ti)O_3 . . . 26
  - 3.4.1 Domain Contrast in cAFM . . . 27

4 Experimental Methods **29**
- 4.1 Annealing . . . 29
- 4.2 SPM Measurments . . . 30
- 4.3 Data Processing . . . 30
  - 4.3.1 Kernel Density Estimations . . . 31
  - 4.3.2 Image Thresholding . . . 32
  - 4.3.3 Bootstrap Sampling . . . 33

5 Mechanisms for Domain Wall Conductance **35**
- 5.1 Dependance on Annealing Parameters . . . 35
- 5.2 Origin of Domain Wall Conduction . . . 38
- 5.3 Constructing a Model for Oxygen Diffusion . . . 41

6 Intrinsic Reversal of Annealing Effects 45
  6.1 Bubble Domains 45
    6.1.1 Stability of Bubble Domains 48
    6.1.2 Control of Bubble Domains 50
    6.1.3 Parallels in Proper Ferroelectrics 52
  6.2 Evolution of Domain Wall Conductance 53
    6.2.1 Domain Wall Conductance 53
    6.2.2 Schottky Contrast between Domains 55

7 Conclusion and Outlook 59
  7.1 Future Work 60

Bibliography 61

Appendix 69

Appendix A: Supplementary Figures 71
  A.1 Supplementary cAFM scans 71
    A.1.1 400 °C for 24 Hours 71
    A.1.2 300 °C for 12 Hours 72
    A.1.3 300 °C for 24 Hours 72
    A.1.4 300 °C for 48 Hours 74
    A.1.5 200 °C for 24 Hours 75
    A.1.6 200 °C for 48 Hours 75
  A.2 Subsequent Annealings 76
  A.3 Schottky Contrast between Domains 77

Appendix B: Scientific Communication 79

Appendix C: Bubble Domain Paper 83

List of Figures

1.1 Conductive domain walls in $BiFeO_3$ 2

2.1 Ferroelectric Perovskites 6
2.2 Hysteresis Curve 7
2.3 Landau Free Energy Density 9
2.4 Ferroelectric Domains and Stray Fields 10
2.5 Ferroelectric Domain Walls 11
2.6 Origin of Conduction in DWs 12
2.7 Structure of the Hexagonal Manganites 13
2.8 Landau Free Energy for Hexagonal Manganites 14
2.9 Domain Structure of h-RMnO$_3$ 15
2.10 Types of Point Defects 16
2.11 Defect Concentration 17
2.12 Thermogravimetric Analysis of $DyMnO_3$ 18
2.13 Oxygen Defects 19

3.1 AFM Schematic 21
3.2 Lennard-Jones Potential 22
3.3 cAFM Schematic 24
3.4 Moiré Patterns in cAFM 25
3.5 Comparison of SPM Techniques 26
3.6 Band Diagram of a Metal-Semiconductor Interface 28

4.1 Annealing 29
4.2 Sample Mounted to Specimen Disc 30
4.3 Schematic depiction of the steps of the bootstrapping algorithm. . 33

5.1 Conduction States of Domain Walls after Annealing 36
5.2 Effect of Annealing Parameters on Domain Wall Conductance . . 37
5.3 Hypotheses for the Origing of Domain Wall Conductance 39
5.4 Subsequent Annealings 40
5.5 Modeled Oxygen Concentration Profiles 43

6.1 Defect-Induced Self-Poling 46
6.2 Suggested Growth Mechanisms for Bubble Domains 47
6.3 Reversal of Bubble Domains 49
6.4 Reversing Bubble Domains using Electric Fields 51
6.5 Controlling the Size of Bubble Domains using Electric Fields . . . 52
6.6 Evolution of Domain Conductivity Over Time 54

6.7 Increase in Schottky Contrast Over Time (Scan) 56
6.8 Increase in Schottky Contrast Over Time (Graph) 57
6.9 IV curves of opposite domains 58

List of Tables

4.1 List of Tips 30

Introduction 1

Since the invention of the first fully electronic computer in the 1940s, the development of modern electronics has undergone a long series of innovation. The first computers, such as the ENIAC (Electronic Numerical Integrator and Computer), utilized vacuum tubes as the means to perform calculations[1]. These tubes were bulky and unreliable and consumed significant amounts of power. In order to increase the performance, new technologies were required, and as such, the 1950s and 1960s saw the advent of transistors and integrated circuits (ICs). Being smaller, more energy efficient, and more reliable, these components led to a sharp rise in the potential of computers. Since then, the size of the electronic components has decreased exponentially, and computing power has gradually been made available also to households and smaller businesses. The development has until now followed Moore's law, a prediction from 1965 stating that the number of components on an integrated circuit doubling every other year[2]. Today, we are in the age of nanoelectronics, where devices operate at the nanometer scale, enabling incredibly powerful and compact computing devices like smartphones and high-performance servers to be used on a daily basis by everyone.

This evolution has transformed computers from massive, room-sized machines to the incredibly powerful and versatile technology we rely on daily, and would not have been possible without a parallel increase in knowledge about material science and engineering. Over the years, new semiconductors and functional materials are developed at a rapid pace. One type of such materials that has been extensively studied for their application as a material for electronics are the ferroelectrics. Ferroelectrics are materials with spontaneous polarization, and are considered interesting for several applications, including ferroelectric capacitors [3], energy harvesting [4], and non-volatile memory [5].

These examples take advantage exclusively of the bulk properties of ferroelectrics. However, another key characteristic of all ferroelectrics is the presence of domains with different orientations of the spontaneous polarization, which are separated by *domain walls* (DWs). These are intrinsic interfaces with a thickness of only a few unit cells[6], and because of their symmetry breaking, they are observed to have electronic properties vastly different from those of the bulk. As early as 1973, it was postulated that ferroelectric domain walls could exhibit metallic conductivity[7]; however, substantial advances in this field have only been realized in the past decade. The development started in 2009, when Seidel *et al.* were able to directly observe the presence of conductive domain walls in ferroelectric $BiFeO_3$ domain walls, and to integrate these domain walls into simple electric circuits[8]. This is shown in Figure 1.1. Since then, conductive domain walls have been reported in a range of ferroelectric materials, such as

Pb(Zr, Ti)O_3[9] and BaTiO_3[10]. To date, the highest domain wall conductance has been recorded in LiNbO_3, with a domain wall conductance exceeding that of the bulk by more than 13 orders of magnitude[11].

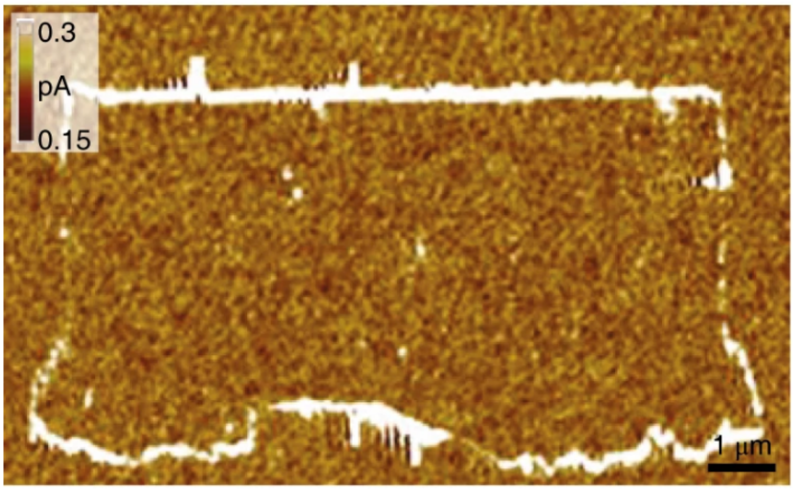

Figure 1.1: cAFM scan of conductive ferroelectric domain walls in BiFeO_3. The bright lines correspond to higher conductance, and represent the ferroelectric domain walls in the material. *Reprinted with permission from [8].*

These findings have garnered substantial attention in the scientific community as a result of their potential as a basis for next-generation electronics. Ferroelectric domains respond to sufficiently strong external electric fields by aligning their polarization; and with conductive domain walls serving as current pathways, this allows for *in situ* control of the position, density and orientation of the conductive paths by writing, erasing and moving domain walls, even after integration into a device architecture[12, 13]. Additionally, the intrinsic properties of the domain walls has been a topic of recent research, with the idea of the domain wall itself becoming the device. A particularly promising candidate for use in domain wall nanotechnology is hexagonal manganites (RMnO_3, R = Sc, Y, In, Dy-Lu), due to the plethora of interesting characteristics arising from their improper ferroelectricity[14]. Over the past decade, extensive research has been conducted on these materials with the ultimate aim of facilitating the development of devices based on domain wall nanotechnology.

1.1 Aim of Work

Recent experiments have shown that conductance in nominally neutral domain walls in Er(Mn, Ti)O_3 can be enhanced by annealing in a reducing atmosphere. Annealing in N_2 gas at 300 °C for 48 hours has proven to be a reliable method to enhance domain wall conductance, and has been extensively used in the research of conductive domain walls within our group. This is attributed to a change in the defect concentration that unequally affects the domain wall and the bulk. The process is reversible, and the enhanced domain wall conductance can be neutralized by annealing in oxidating environments. This dependence of the domain wall conductance on the surrounding atmosphere indicates a potential use of domain wall devices in atmospheric sensing applications. However, more research is needed to build a deeper understanding of the origin of conductance, and how it relates to the annealing process.

This study focuses on examining the annealing process and the impact of various annealing parameters on the domain wall conductance, particularly focusing on the annealing temperature and dwell time. The material is subsequently analyzed using different scanning probe microscopy techniques, such as conducting atomic force microscopy (cAFM) and piezoresponse force microscopy (PFM). This additional data will contribute to the understanding of the defect chemistry that influences changes in domain wall conductance and provide guidelines for property engineering at the domain walls. Furthermore, the temporal behavior of the resulting domain wall conductance is investigated to offer a comprehensive description of the evolution of defects and the resulting material properties.

1.2 Structure of the Thesis

This thesis is structured as follows: Chapter 2 provides a theoretical background to the materials, with a focus on ferroelectrics and point defects in crystalline materials. In Chapter 3, an introduction to the use of different scanning probe techniques for imaging ferroelectric domains is provided, including topographical atomic force microscopy, conductive atomic force microscopy, and piezoresponse force microscopy. Chapter 4 is devoted to a description of the experimental procedures, along with details about post-experimental data analysis.

In Chapter 5, the effect of annealing on the conductance in the ferroelectric domain walls is studied. A series of annealing experiments is performed with slightly different procedures to uncover the underlying mechanisms of domain wall conductance. Continuing from this, the material is further studied with respect to the long-term effects after annealing in Chapter 6. In particular, this chapter discusses emergent improper ferroelectric bubble domains, which arise by self-poling of the material during annealing. Finally, the discussion is concluded in Chapter 7, together with suggestions for future work to be done to further increase our understanding of how the ferroelectric domain wall conductance is modulated by the underlying defect chemistry.

Theoretical Background 2

This study focuses on ferroelectric domain walls in titanium-doped erbium manganite ($\mathrm{Er(Mn,Ti)O_3}$), one of the hexagonal manganites of the form h-$R\mathrm{MnO_3}$ (R = Sc, Y, In, Dy-Lu). To give a brief overview of the theoretical foundation used in later chapters, this chapter presents first a definition of ferroelectric, as well as key concepts regarding their domains and domain walls, before taking a closer look on the hexagonal manganites. Finally, a short overview is given of the chemistry of defects and how they relate to the previous topics.

2.1 Ferroelectrics

Ferroelectrics belong to a broad class of materials known as *ferroics*. The term "ferroic" was coined in 1969[15] upon the discovery of ferroelastic relaxation in certain materials and was used to relate this property to previously known ferromagnets and ferroelectrics. The term derives from the Latin word for *iron*, which was used for the first identified ferromagnets, all of which contained iron as a significant component. Later, the prefix was used again when ferroelectric properties were discovered in Rochelle salt ($\mathrm{KNaC_4H_4O_6} \cdot 4\mathrm{H_2O}$) in 1920[16], highlighting the strong resemblance in behavior to ferromagnets. Today, the term *ferroics* encompasses four main subclasses: ferroelectrics, ferromagnets, ferroelastics and ferrotoroidics.

A key concept to describe ferroelectrics is that of non-disruptive phase transitions. This type of phase transition, unlike disruptive ones, allows each side of the transition to be formed by continuous distortiion from the other[17]. This idea parallels other phase transitions, such as in superconductors[18] and liquid crystals[19], where the new phase emerges smoothly from the old one.

In ferroelectrics, the phase transition involves a change in thesymmetry of the crystal point group, separating it into a high symmetry point group S_0 and a lower symmetry point group S, where S is a proper subgroup of S_0, [20]

$$S \subset S_0. \tag{2.1}$$

Specifically for ferroelectrics, this symmetry change results in the loss of inversion symmetry between the two phases. The transition occurs at the Curie temperature T_C, with the high symmetry, disordered phase present at higher temperatures and the low symmetry, ordered phase present at lower temperatures. The change in symmetry is driven by the appearance of an order parameter, which takes the value of zero in the disordered phase and increases in

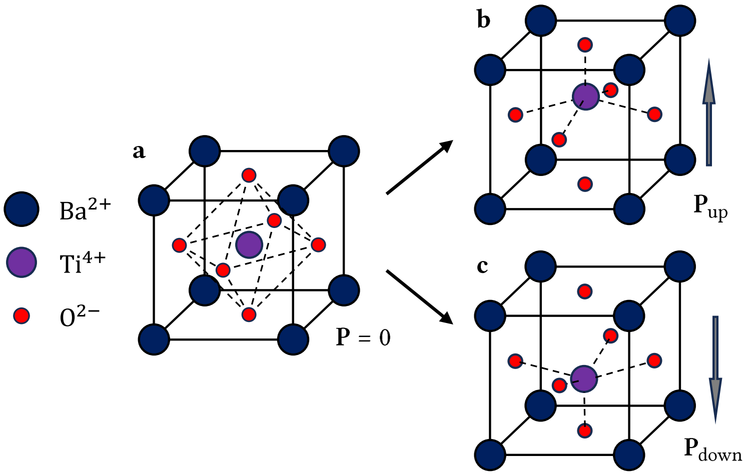

Figure 2.1: **a**. The perovskite structure of $BaTiO_3$ in the paraelectric state, with inversion symmetry and zero net polarization. **b-c.** Below T_C, the central Ti^{4+} ion is skewed relative to the grid, inducing a ferroelectric polarization in the crystal.

magnitude in proportion to the system's ordering as the temperature decreases in the ordered phase.

An example of such a ferroelectric system is $BaTiO_3$, which has the perovskite crystal structure, illustrated in Figure 2.1. The structure is cubic, with the Ba^{2+} ions in the corner position, the Ti^{4+} ions in the body center, and the O^{2-} ions on the face centers[21]. At $T > T_C$, the crystal is symmetric with respect to inversion, having the central ion in the center of the unit cell. This state is known as the paraelectric state. However, upon cooling below T_C, the Ti^{4+} ion is slightly moved away from its central position, breaking the inversion symmetry of the crystal. This reduces the number of coordinated ligands around the central ion, thereby increasing the thermodynamic stability of the crystal structure. As a consequence of this displacement, the charge centers for positive and negative charges in the unit cell no longer coincide, and are separated by a distance **l**, with direction defined from the positive center to the negative center. This gives the polarization per unit cell **p**,

$$\mathbf{p} = q\mathbf{l}, \tag{2.2}$$

where q is the magnitude of the charge of the two charge centers. Performing a space inversion on this state changes the relative position of the charge centers, and reverses the polarization $\mathbf{p}$ to $\mathbf{p}^* = -\mathbf{p}$. All microscopic polarization elements combine to give a total macroscopic polarization **P**, [22, p. 191]

$$\mathbf{P} = \sum_i \mathbf{p}_i. \tag{2.3}$$

As the temperature drops, the polarization of the unit cell increases, thus meeting the criteria to be regarded as the order parameter of the system.

Electric fields **E** can be used to change the orientation of a polarization state by inducing an energy difference between states. This switching is driven by the Helmholtz free energy F,

$$F = -\mathbf{E} \cdot \mathbf{P}, \tag{2.4}$$

which is reduced with the alignment of the polarization and electric field. The switching of ferroelectric domains under an electric field demonstrates hysteretic behavior typical of ferroics. When a net neutral poly-domain structure is exposed to an electric field, the domains progressively align as the field strength increases, leading to a rise in net polarization (dotted line), until a saturation point is reached where all domains are aligned. Upon reducing the electric field, the structure remains ordered, with a remnant polarization P_r remaining at $F = 0$. To reintroduce the poly-domain structure, a field in the opposite direction is necessary before all domains realign oppositely. The field needed to achieve a net zero polarization from a fully ordered state is termed the coercive field, E_c. This results in a multivalued function P of F, known as a hysteresis loop, illustrated in Figure 2.2[20].

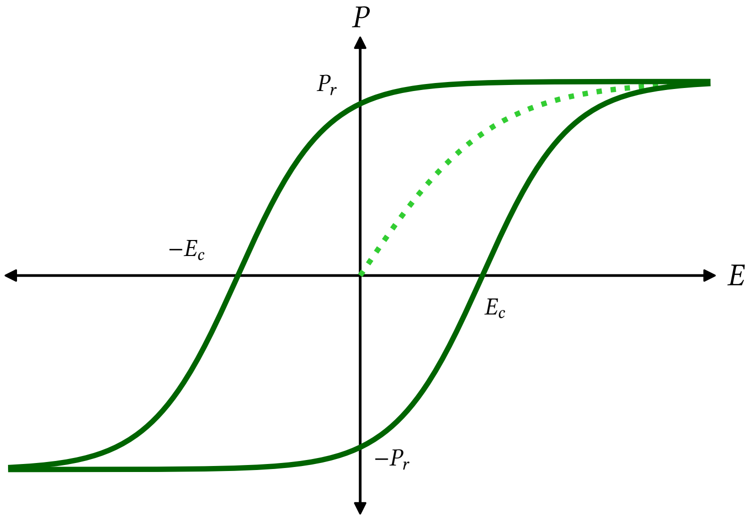

Figure 2.2: Hysteretic behavior of the polarization-induced macroscopic property P as a function of the applied electric field E. The coercive field $\pm E_c$ and remnant order $\pm P_r$ are indicated as the intersections where the curve crosses the axes.

The above case of $BaTiO_3$ is an instance of proper ferroelectricity, where the structural distortion that breaks the symmetry is directly coupled to the resulting polarization. In contrast, in improper ferroelectrics, polarization appears through its interaction with another primary order parameter, which by itself would not affect the material's electrostatics[23]. Common examples include non-ferroelectric lattice distortions and magnetic spin configurations[12]. Section 2.3 provides a more detailed discussion of the improper ferroelectricity found in hexagonal manganites.

All ferroelectric materials are also piezoelectric[24]. Piezoelectric materials are polarized under applied mechanical stress σ in certain crystallographic directions, and similarly undergo a mechanical deformation under applied electric fields. They are described by the material-specific piezoelectric constant d_{ijk} by the relation $P_i = d_{ijk}\sigma_{jk}$. The piezoelectric property has a wide range of applications, one of which is piezoresponse force microscopy (PFM), one of the most widely used methods for measuring and mapping ferroelectric domains[25].

2.2 Ferroelectric Domains and Domain Walls

In the absence of external electric fields, regions exist in all ferroelectric materials in which spontaneous polarization is uniformly aligned in a specific direction. Such regions are called ferroelectric domains.

2.2.1 Origin of Domains

A mathematical explanation of the formation of domains is given by the Landau theory, which provides a general description of the behavior of ferroelectric materials close to T_C[21, p. 563-566]. The theory is founded on the assumption that the dependence of the Helmholtz free energy density on the ferroelectric polarization and temperature, $F(P, T)$, can be represented using the same power series expansion for both the paraelectric phase at high temperatures and the ferroelectric phase at low temperatures:

$$F = F_0 + \frac{1}{2}\alpha_2(T)P^2 + \frac{1}{4}\alpha_4(T)P^4 + \frac{1}{6}\alpha_6(T)P^6 + \dots, \tag{2.5}$$

with $\alpha_i(T)$ being temperature dependent coefficients. The odd powered terms of P are disregarded, as the the inversion symmetry of the paraelectric phase induces no preference for any of the polarization directions. $F(P, T)$ must therefore be even, with $F(P) = F(-P)$. For ferroelectric phase transitions, the fourth-order term is positive, and is assumed to be independent on temperature, $\alpha_4(T) = a_4$.

The equilibrium state is determined by the minima of the free energy density, which in the absence of any conjugate field is at $P = 0$ above T_C, and at a non-zero value of P below T_C. A schematic of $F(P)$ at various temperatures is shown in Figure 2.3. This behavior is governed by the coefficient of the second order term α_2, which must change from positive to negative as the temperature changes from above to below T_C. A Taylor expansion of the temperature around T_C gives

$$\alpha_2 = a_2(T - T_C). \tag{2.6}$$

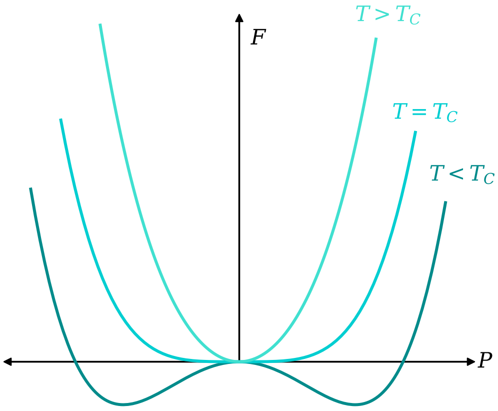

Figure 2.3: Schematic illustration of the dependence of the free energy density F on the order parameter P at temperatures above, equal to and below the transition temperature in a second order transition.

Assuming the order parameter is near the transition, we neglect terms of the sixth order and beyond, leaving the expression

$$F = a_0 + \frac{1}{2}a_2(T - T_C)P^2 + \frac{1}{4}a_4P^4, \tag{2.7}$$

where a_2 and a_4 are positive constants. The various orientations of spontaneous polarization in ferroelectrics have intrinsically the same energy level. As such, after cooling below T_C, the specific state if the system is determined by a stochastic process, with equal probability for each state. Energy fluctuations during the transition cause spontaneous polarization to initiate at certain points, from which it grows through the material as regions with uniform orientation. This results in the formation of domains with different orientations throughout the material.

In addition to the internal factors when ferroelectricity form, ferroelectric domains act as a mechanism for mitigating stray fields external to the material, shown in Figure 2.4. The stored energy U within an electric field relies on the strength of the electric field following the equation

$$U = \frac{1}{2}\iiint_V \varepsilon\,|\mathbf{E}|^2\,\mathrm{d}V, \tag{2.8}$$

where ε is permittivity of the medium[22]. Minimizing the stored energy of a ferroelectric material involves a compromise between the interfacial energy between the domains and the reduction of the stored energy in the stray fields. In general, the size of the domains, σ, follow Kittel's law, scaling proportionally to the square root of the size of the grain in which they are contained, d, [26, 27]

$$\sigma \propto \sqrt{d}. \tag{2.9}$$

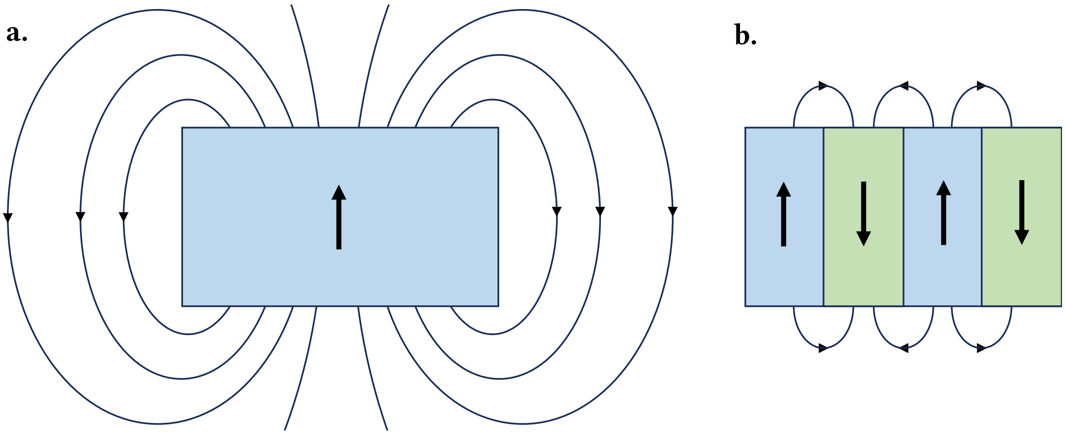

Figure 2.4: The extent of stray fields in a multi-domain crystal (**a.**) and a single domain crystal (**b.**). The extent of the field, and thereby the stored energy, is significantly reduced in the multi-domain crystal.

2.2.2 Domain Walls

The interfaces separating domains of different orientations of the polarization are known as ferroelectric domain walls. Figures 2.5a-c show three main ways of transition[27, 28]. In Bloch- and Néel-type domain walls, the polarization rotates gradually across the domain wall with little variation in magnitude, along an axis normal to and with the domain wall plane, respectively. Such rotations of the order parameter create additional symmetry breaking in the walls: Bloch walls are chiral, so that two domain walls may differ from each other by handedness. On the other hand, Néel walls create areas of opposite bound charge density on the sides of the domain wall center, resulting from the non-zero divergence of the polarization. The third type is known as ising domain walls, where the transition occurs only in the magnitude of the polarization while remaining parallel to the polarization in the adjacent domains (Figure 2.5c)[28]. A majority of 180° domain walls are of ising type domain walls with thickness in the nanometer or sub-nanometer regime[27].

Due to the local environment on the domain wall being different from that of the surrounding domain, they may exhibit properties different from those of the surrounding bulk domain, including electrostatic and electronic properties[13, 28, 29]. Depending on the relative change in the direction of the polarization on either side of the wall, the domain walls can be classified in terms of neutral and charged walls, indicated in Figures 2.5d-f[12]. Cases where the polarization on either side of the domain wall points away from or towards the wall (tail-to-tail and head-to-head, respectively) results in an accumulation of bound charges, ρ_{bound}, [22, p. 191]

$$\nabla \cdot \mathbf{P} = \rho_{\text{bound}}, \tag{2.10}$$

requiring screening by moving mobile charge carriers towards or away from the domain wall. The exact behavior depends on the conduction regime of the species. For example, in p-type ferroelectric semiconductors, holes

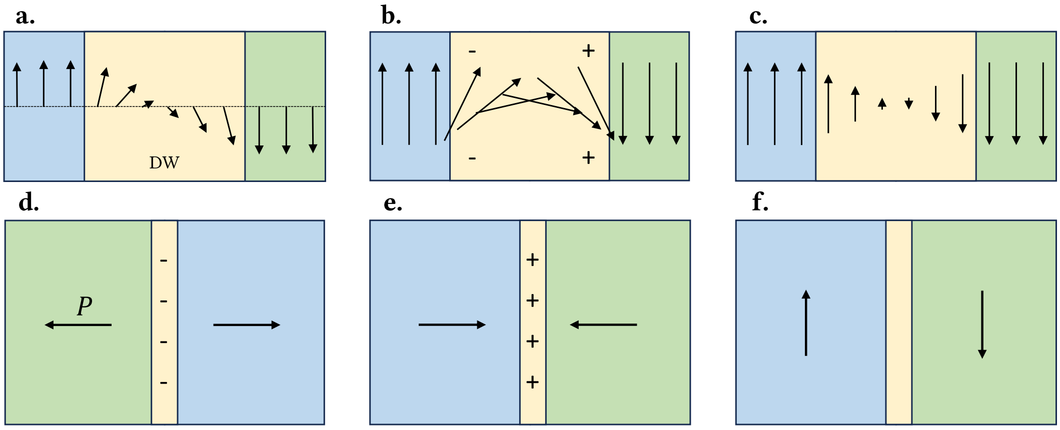

Figure 2.5: a. Néel type domain wall with polarization orientations rotating along an axis within the domain wall plane. **b.** Bloch type domain wall with polarization orientations rotating along an axis normal to the domain wall plane. **c.** Ising domain wall, with a transition in magnitude polarization instead of orientation. **d.** Negatively charged tail-to-tail domain wall. **e.** Positively charged head-to-head domain wall. **f.** Neutral side-by-side domain wall.

gather at negatively charged domain walls, enhancing conductance, and move away from positively charged walls, reducing conductance. Conversely, in n-type semiconductors, conductance is enhanced and reduced at positively and negatively charged domain walls, respectively. Neutral side-by-side domain walls where $\nabla \cdot \mathbf{P} = 0$ experiences no such accumulation of charges.

2.2.3 Conduction Mechanisms in Ferroelectric Domain Walls

Conductance in ferroelectric domain walls has been intensely studied with regard to the underlying mechanisms of conduction[13, 14, 28, 29] after the first observation in 2009[8], and can be classified into three contributions[29]. First, calculations based on density functional theory (DFT) and investigations of the density of states using scanning tunneling spectroscopy have demonstrated that the conduction band energy can be reduced in the domain walls without altering the valence band energy level (Figure 2.6a). This alteration is attributed to the differences in atomic and electronic configurations and symmetry between the domain wall and the bulk material. However, it is debated whether this relatively small reduction in conduction band energy is sufficient to account for the observed increase in conductivity, leading to the belief that domain wall conduction results from a combination of bandgap reduction and other effects[29].

In charged (head-to-head and tail-to-tail) domain walls, the accumulation of bound charges impacts the band structure beyond reducing the conduction band energy (Figure 2.6b). The divergence of the electric field can significantly lower the band energy in head-to-head walls, with the conduction band minimum potentially dipping below the Fermi energy, E_F. In n-type semiconductors, electrons accumulate in these dips in the conduction band, serving as charge

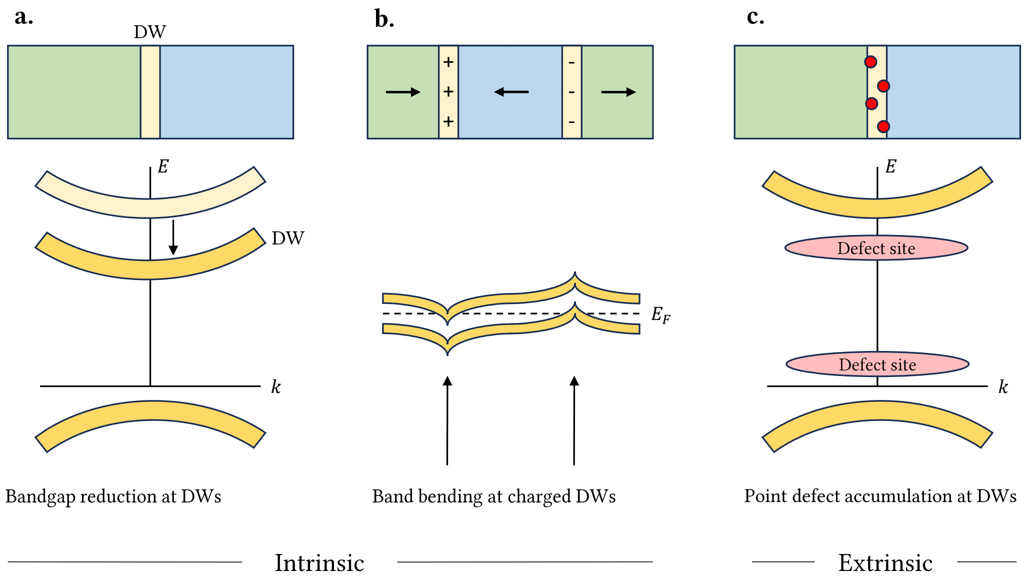

Bandgap reduction at DWs

Band bending at charged DWs

Point defect accumulation at DWs

Figure 2.6: Conduction in domain walls (DWs) is primarily attributed to three factors. **a.** Modification in the band structure within the domain wall resulting in a reduced band gap between the valence band (bottom semicircle) and the conduction band (top semicircle). **b.** Local charge accumulation at the domain wall causing an increase (tail-to-tail) or decrease (head-to-head) in the band structure. **c.** Defects may introduce intra-bandgap states acting as donor or acceptor bands. E and k represent the energy and wave vector, respectively. *Adapted from [29].*

carriers for conduction, while holes deplete in p-type semiconductors. Similarly, the band energy increases in tail-to-tail walls, attracting holes and repelling electrons[29].

These mechanisms are intrinsic to the material and are not contingent on defects or other external influences. A third extrinsic factor is proposed, involving the accumulation of defects at the domain walls (Figure 2.6c). Domain walls can achieve altered stability for certain defects[30], and depending on the specific type of defect, this introduces donor or acceptor states to the bad structure, reducing the gap between the valence band and the conduction band, resulting in enhanced conduction[29].

Conductive domain walls, which are easily poled by external electric fields, can act as flexible routes for current flow in novel devices, in which interfaces can be dynamically adapted even after integration into a device architecture[13, 14].

2.3 Hexagonal Manganites

Hexagonal rare earth manganites are geometrically improper ferroelectrics of the form $R\text{MnO}_3$, where R belongs to scandium, yttrium, indium, or one of the rare earth metals between and including dysprosium and lutetium. These materials are considered interesting model systems for studying domain wall conductance for the application in novel nanoelectronics, based on several factors. For example, they exhibit various charge states of the domain walls, from fully charged positive head-to-head walls to tail-to-tail walls in their natural state[14], and are susceptible to defect formation [31], which are both promising attributes for domain wall conduction. In addition, the extensive research conducted on them has contributed to a comprehensive understanding of their properties and characteristics.

The crystal structure of hexagonal manganites is built from corner-sharing MnO_5 trigonal bipyramids, separated by hexagonally ordered planes of rare-earth ions, illustrated in Figure 2.7[32]. These materials exhibit improper ferroelectricity resulting from a structural instability below the transition temperature that ranges from $T_C \approx 950\,^\circ\mathrm{C}$ in $YMnO_3$[33] to $T_C \approx 1450\,^\circ\mathrm{C}$ in $LuMnO_3$[34]. Three adjacent MnO_5 polyhedra collectively tilt toward or away from their shared rare earth ion, causing a vertical distortion in the R-ion layer and a tripling of the unit cell[35, 36]. The trimerization is indicated in Figure 2.7b by the inserted triangles. This breaks the $P6_3/mmc$ symmetry of the high-temperature phase and reduces it to $P6_3cm$. When viewed along the a-axis, the distorted rare earth layer surfaces as an alternating pattern, where every third ion is distorted in one direction, while the remaining ions are distorted in the other direction, indicated by different colors of the ions in Figure 2.7. This effect creates the charge imbalance that serves as the origin of the ferroelectric polarization. Two ions displaced downwards and one upwards (●●●) results in downwards polarization, while two ions displaced upwards and one downwards (●●●) results in upwards polarization.

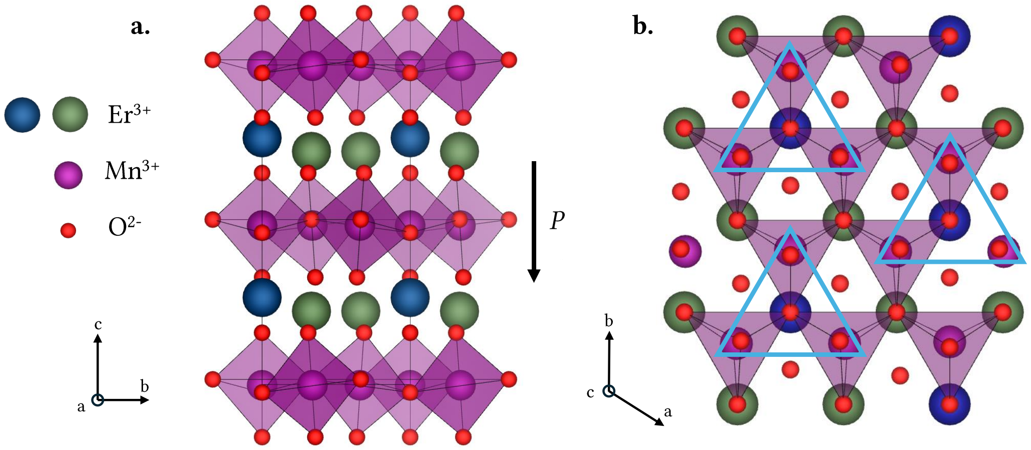

Figure 2.7: Crystal structure of $ErMnO_3$ viewed along the hexagonal a-axis (**a.**) and c-axis. The triangels in subfigure **b** indicate the trimerized polyhedra resulting in the ferroelectric polarization. *Constructed in VESTA[37] using crystallographic data from Ref. [38].*

There are two main order parameters governing the ferroelectric behavior of the hexagonal manganites [39]. Primarily, the two-dimensional order parameter $\mathbf{Q}$ describes the tilting of the MnO_5 bipyramids and can be broken down into the tilt amplitude Q and the azimuthal tilt orientation Φ. A secondary order parameter $\mathcal{P}$ emerges due to the coupling between the tilting and the displacement of the rare earth ion layer relative to the MnO_3 layer, and corresponds proportionally to the polarization. These order parameters combine into the Landau free energy density by the following simplified equation, [36]

$$\begin{aligned} F = \frac{1}{2}a_2(T - T_C)Q^2 + \frac{1}{4}a_4Q^4 + \frac{1}{6}Q^6(a_6 + a_6' \cos 6\Phi) \\ - gQ^3\mathscr{P} \cos 3\Phi + \frac{1}{2}g'Q^2\mathscr{P}^2 + \frac{1}{2}a_{\mathscr{P}}\mathscr{P}^2, \quad (2.11) \end{aligned}$$

where a_2, a_4, a_6, a_6', g, g' and $a_{\mathscr{P}}$ are the Landau coefficients for the various terms. Here, only power terms are included, and any terms containing the gradients are excluded. This equation represents a surface that, for $T < T_C$, features six non-zero minima corresponding to six degenerate equilibrium states with varying tilt angles. A plot of $F(\mathbf{Q})$ is shown in Figure 2.8. The equilibrium states represent the trimerization patterns centered around three different rare earth ion sites, referred to as the antiphases α, β, and γ. In each antiphase, the polyhedra can tilt either towards or away from the central ion, resulting in two possible polarization states, + and −.

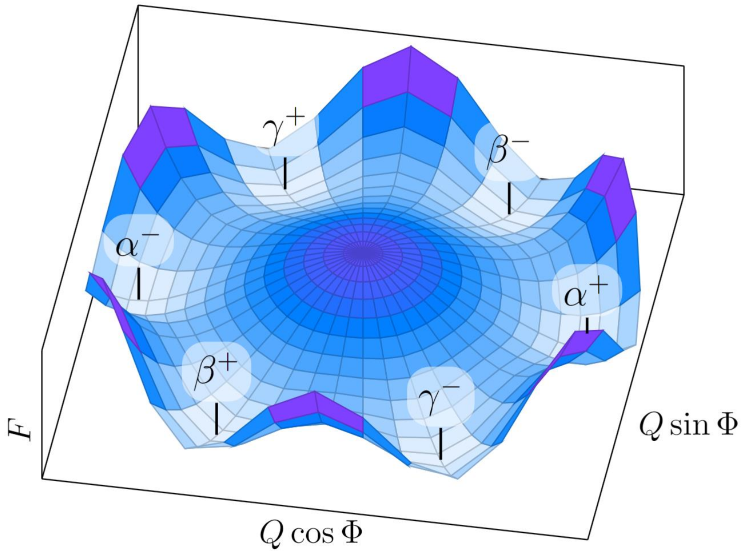

Figure 2.8: Surface plot of the Landau free energy below the transition temperature as a function of the two-dimensional order parameter $\mathbf{Q}$, with radial component Q and angular component Φ. The six equilibrium states are indicated in their respective minima.

In principle, domain walls in hexagonal manganites occur in three flavors depending on the difference in polarization and antiphase between the domains: they can be pure ferroelectric (*e.g.* α^+-α^-), purely antiphase (*e.g.* α^+-β^+), or a combination of the two, having the domain differing in both polarization and antiphase (*e.g.* α^+-β^-). However, because of the large distance in the order parameter space and the high inter-state energy between the purely ferroelectric domain walls and the purely antiphase domain walls, these domain walls are associated with a large transitional energy, and only the latter type of domain wall type is commonly observed experimentally.

As a result of this energy landscape, the most stable method of intersecting two or more domain walls is to have all six domains meet in cloverleaf-like vortex structures, as shown in Figure 2.9. The domain walls can arrange themselves around the vortex core in two chiral patterns, clockwise as a vortex ($\alpha^+, \beta^-, \gamma^+, \alpha^-, \beta^+, \gamma^-$), or anti-clockwise as an antivortex ($\alpha^+, \gamma^-, \beta^+, \alpha^-, \gamma^+, \beta^-$).

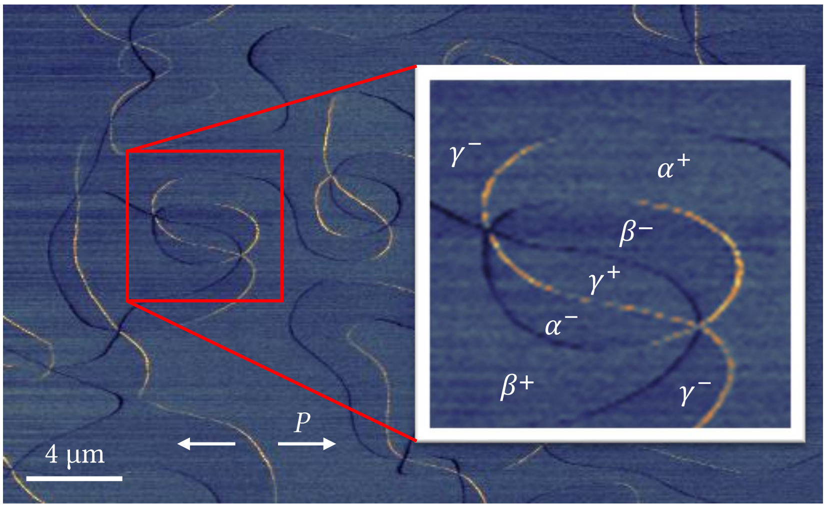

Figure 2.9: cAFM image of the typical domain structure in the hexagonal manganites, with domain walls meandering between the cloverleaf-like vortices. The polarization is indicated by the arrows. The brighter and darker lines represent conductive tail-to-tail domain walls and insulating head-to-head domain walls respectively. The inset shows a vortex-antivortex pair with the surrounding domains labeled according to their antiphase and polarization. *Data courtesy of Jiali He.*

The vortices form as lines throughout the material that separate different orientations of **Q** as a first step in the transition over the ferroelectric Curie temperature even before the domains are well defined[40]. These vortices are considered topological defects as they cannot be removed by simple continuous transformations, which makes them stable features in the domain structure of the material. Subsequently, domain walls form to connect the vortices in a meandering pattern throughout the material. Due to the topological stabilization of the vortices, all charge states of the domain walls (see Figure 2.5) are stable and occur naturally[41], making these materials interesting model systems for studying the electronic properties of the domain walls. For example, ErMno3 is a p-type semiconductor, and positive screening charges are attracted to negative tail-to-tail walls, leading to a non-uniform charge carrier density and enhanced conductance in the domain walls[14]. The opposite is true for positively charged walls, in which conductance is reduced. As a result, hexagonal manganites hold great potential for the future development of domain wall nanoelectronic.

2.4 Defects in Crystalline Materials

Perfect crystals where all atoms occupy their respective correct position in the crystal structure are hypothetically possible only at the absolute zero temperature. At finite temperatures all crystals are imperfect, and defects naturally occur in all crystallic materials. Crystallic defects are defined as lattice irregularity with at least one dimension at the order of magnitude of an atomic radius[42, p. 81], and are classified by the number of dimensions extending to beyond the atomic scale. 2D defects normally separate areas of the crystal with different crystal structures or orientations of the lattice vectors, and include grain boundaries, stacking faults and external surfaces. 1D defects extend linearly through the material, and include defects such as edge dislocation and screw dislocations. Lastly, there are 0D defects, often referred to as point defects, which are confined within a single or a few atomic position[42].

2.4.1 Point Defects

Point defects are imperfections within a solid that are confined to a single point. Three types of point defects that are encountered within ionic solids are illustrated in Figure 2.10. Substitutional ions are occasionally considered to be impurities that need to be eliminated, while other times they are intentionally introduced as dopants to impart new properties to the material that are absent in the pure crystal. These are extrinsic defects that result from the addition of species not part of the regular crystal structure. Intrinsic defects, on the other hand, include ion vacancies and interstitial ions, where ions are either removed from or inserted into the crystal lattice. By themselves, these defects introduce a charge to the material, which must be balanced for the crystal to remain electrically neutral. This can be achieved by pairing a vacancy with an interstitial ion to uphold the stoichiometric composition of the material, or through oxidation or reduction processes, thereby rendering the material off-stoichiometric.

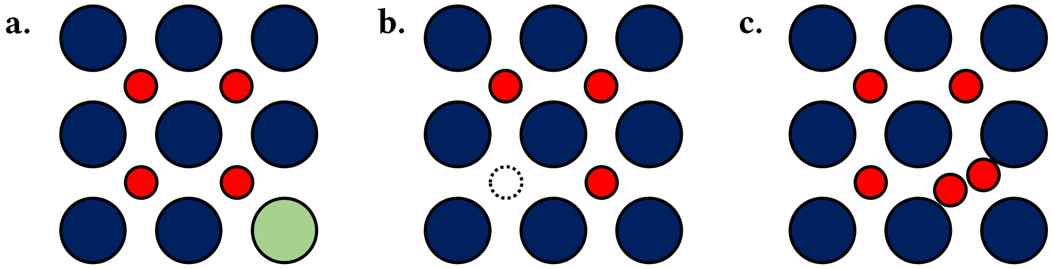

Figure 2.10: Schematic of three types of non-stoichiometric point defects in ionic solids, constituting **a**. substitutional ions, **b**. vacancies, and **c**. interstitional ions.

The formation of intrinsic defects is driven by a reduction of the free energy ΔG of the material, given by

$$\Delta G = \Delta H - T\Delta S, \tag{2.12}$$

where ΔH is the enthalpy, T is the temperature, and ΔS is the entropy[43]. The enthalpy is considered the number of broken chemical bonds while forming a vacancy, or the energy required to insert an ion into an interstitial poisition, and therefore, it scales linearly with the concentration of defects for low defect concentrations. The entropy is by a statistical-mechanical approach given by the Boltzmann law,

$$S = k_B \ln W, \tag{2.13}$$

where k_B is the Boltzmann constant, and W is the number of possible configurations of a system with a given number of defects[43]. By this relation, the entropy increases rapidly for low defect concentrations, but flattens out at higher concentrations where adding additional defect will not as drastically increase the order of magnitude of configurations. As a result, there is a minimum in the total free energy where the energy required to add new defects is no longer accounted for by the increase in entropy, defining the equilibrium defect concentration in the material[43]. A graph of the minimum is shown in Figure 2.11.

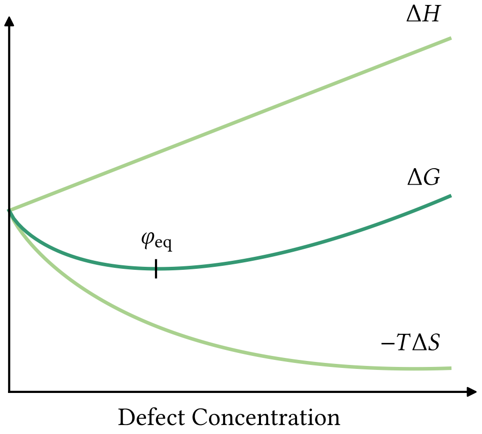

Figure 2.11: The free energy ΔG with its enthalpic and entropic components, ΔH and $-T\Delta S$, respectively, as a function of defect concentration. The equilibirum concentration, φ_{eq} of intrinsic defects is indicate at the minimum of the free energy curve.

The entropy term of the free energy depends on the temperature of the system. Therefore, the influence of the entropy increases with increasing temperature, which also affects the free energy minimum. A model of this temperature dependence of the equilibrium concentration of intrisic defects is given by the relation

$$N_d = N \exp\left(-\frac{Q_V}{k_B T}\right), \tag{2.14}$$

where Q_V is the defect formation energy, and k_B is the Boltzmann constant. The proportionality factor N represents the total number of defect sites available in the material[42, p. 81].

2.4.2 Oxygen Defects in Hexagonal Manganites

The hexagonal manganite structure has shown to be very flexible in regards to oxygen defect chemistry, and can accommodate large concentrations of both oxygen vacancies and interstitial oxygen ions[31]. The formation energy of oxygen defects strongly depends on the thermal and atmospheric history of the material. For example, high temperature and low partial pressure of O_2 in the surrounding atmosphere favours formation of oxygen vacancies, while low temperature and high oxygen partial pressure favours interstitial oxygen ions. Remsen *et al.* have found that depending on the oxidative state and annealing temperature of $DyMnO_{3+\delta}$, the oxygen off-stoichiometry can vary with a δ range of up to 0.7 using thermogravimetric analysis (TGA)[31]. TGA is a technique in which the mass of a powdered material is continuously measured under heating, to give information on the temperature dependence of the mass. For $DyMnO_3$, the dysprosium and manganese ions are not affected by heating, so the mass is directly correlated with the oxygen content. The measured curve is shown in Figure 2.12.

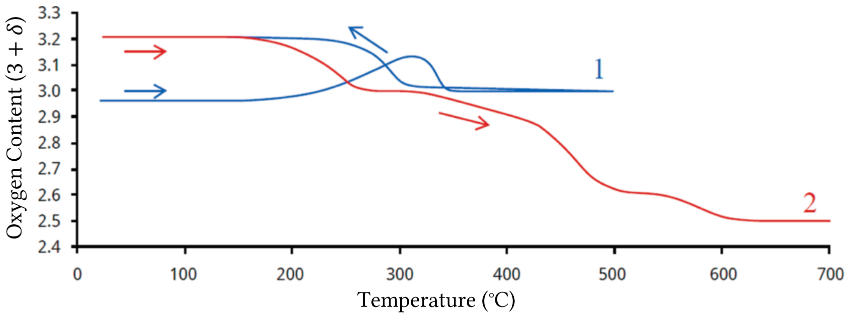

Figure 2.12: TGA measurements of $DyMnO_3$ under oxidation in 21 % O_2 (curve 1) and subsequent reduction in 42 % H_2 (curve 2). *Reprinted with permission from [31]. Copyright 2011 American Chemical Society.*

Oxygen excess and deficiency manifest themselves in the material as oxygen interstitials (O_i) and vacancies (v_O) respectively. The general crystal structure remains the same regardless of the oxygen off-stoichiometry, with the variance occurring only by the number of oxygen ions dispersed throughout the crystal. In fact, oxygen defects are only found in the plane with manganese ions [30], creating sporadic MnO_6 octahedra and MnO_4 disphenoids (seesaw structures) in place of the common tetragonal bipyramids. The imbalance in charge is then accounted for by altering the oxidation states of the cations[44].

Introduction of oxygen vacancies decreases the concentration of negatively charged ions, which in turn would leave the crystal with a net positive charge.

This is compensated by a reduction of the Mn following the reaction[45]

$$2\,\mathrm{Mn}_{\mathrm{Mn}}^{\times} + \mathrm{O}_{\mathrm{O}}^{\times} \rightleftharpoons 2\,\mathrm{Mn}_{\mathrm{Mn}}^{\prime} + \mathrm{v}_{\mathrm{O}}^{\bullet\bullet} + \frac{1}{2}\,\mathrm{O}_2(\mathrm{g}) \tag{2.15}$$

This equation is expressed in the Kröger-Vink notation[46], where a prime ($'$) denotes a negative relative charge, a circle ($^{\bullet}$) denotes a positive relative charge, a cross ($^{\times}$) denotes a neutral relative charge. The subscript indicates the lattice site that the species occupies. Similarly, formation of interstital oxygen ions is accompanied by oxidation of the Mn ions, [44]

$$\frac{1}{2}\,\mathrm{O}_2(\mathrm{g}) + 2\,\mathrm{Mn}_{\mathrm{Mn}}^{\times} \rightleftharpoons 2\,\mathrm{Mn}_{\mathrm{Mn}}^{\bullet} + \mathrm{O}_{i}^{\prime\prime}. \tag{2.16}$$

Density functional theory (DFT) calculations suggest that the stability of oxygen interstitials and vacancies varies between nominally neutral domain walls and the bulk in $\mathrm{YMnO_3}$[30]. For oxygen excess, interstitial oxygen is predicted to gather at domain walls, enhancing conductivity by modifying the electronic structure and creating donor states, as shown in Figure 2.6. Conversely, oxygen vacancies are expected to migrate away from the domain walls and accumulate in the bulk domains. This behavior is depicted schematically in Figure 2.13.

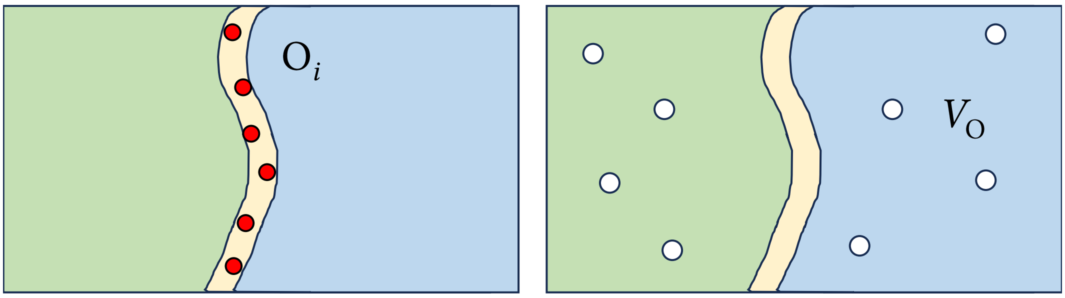

Figure 2.13: Predicted imbalanced behaviour of oxygen defects in neutral domain walls in hexagonal manganites compared to the bulk. Oxygen interstitials (O_i) accumulate in domain walls (left), while oxygen vacancies (V_O) accumulate in the bulk (right).

Recent studies have shown that annealing can be used to regulate the conduction state of neutral domain walls. Annealing in a reducing atmosphere, such as $\mathrm{N_2}$, transforms the conduction state from non-conductive to conductive. Conversely, annealing in oxidizing atmospheres, like $\mathrm{O_2}$, eliminates the conduction property, rendering the domain walls non-conductive or even insulating. These changes are attributed to oxygen off-stoichiometry, believed to be induced by annealing in a manner similar to that depicted in Figure reffig:oxdefects. However, the mechanisms by which annealing enhances conductance in neutral domain walls in hexagonal manganites remain unclear. Although DFT predicts that oxygen-rich conditions are required for enhanced domain wall conductance, experimental observations indicate that conductance is actually enhanced after annealing in reducing atmospheres. Several hypotheses have been proposed to reconcile the discrepancy between these findings without discrediting either of them. Due to the increased stability of interstitials in the domain walls, reduction may primarily affect the bulk, increasing the difference in oxygen off-stoichiometry between the two areas. Consequently, the coexistence of oxygen interstitials in the domain walls and vacancies in the bulk leads to enhanced domain wall conductance. Alternatively, reduction may completely affect the entire surface when submerged in N_2, but as the surface is exposed to oxygen in the air after annealing, the domain walls reoxidize more quickly than the bulk.

Scanning Probe Microscopy

3

Scanning probe microscopy (SPM) is a collection of techniques used to acquire detailed information about the surface properties of samples, ranging from the micrometer to the atomic level. Since its invention in the 1980s [47], SPM has found applications in various fields, including material characterization, electronics, biology, and biomaterials. These techniques have revolutionized surface analysis by providing high-resolution images and measurements that were previously unattainable [48].

A typical SPM setup is schematically shown in Figure 3.1, and consists of a flexible cantilever probe equipped with a sharp tip that is used to scan the surface of the sample to measure the local properties on the surface. These interactions frequently cause the cantilever to bend or vibrate depending on the contact between the tip and the sample. To monitor the reaction of the cantilever, a laser beam reflects off the cantilever and hits a position-sensitive photodetector. The sample is mounted on a piezoelectric scanner, which allows precise control of the position of the sample in the x, y and z directions. When scanning the tip over the surface, an electronic feedback mechanism provides detailed instructions to the piezoelectric scanner, allowing it to maintain the tip at a constant force or a constant height above the sample surface, ensuring accurate and consistent measurements [48].

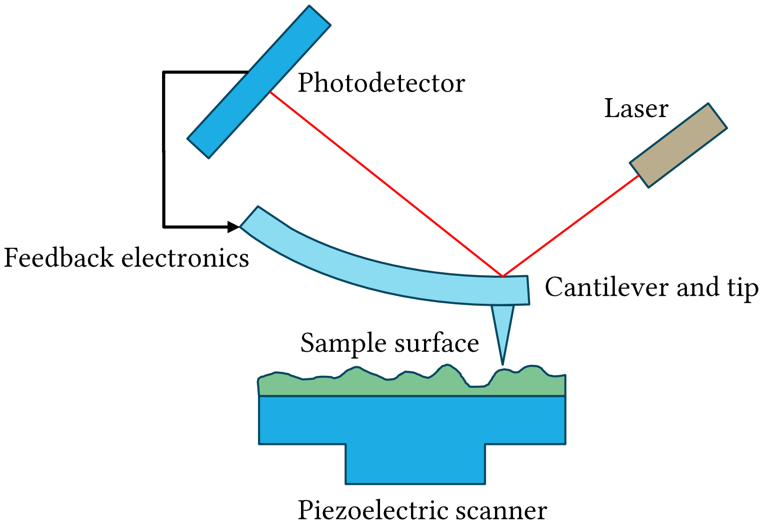

Figure 3.1: Simplified schematic illustration of the key components constituting a scanning probe setup.

3.1 Atomic Force Microscopy

The simplest form of scanning probe techniques is the atomic force microscopy (AFM). This technique maps the surface topography of the sample by reacting to the interatomic force between the tip and the sample, which is mainly attributed to van der Waals interactions. The force is non-linearly dependent on the distance between the tip and the sample, r, with a short-range repulsive force and a longer-range attractive force, and is often modeled by the Lennard-Jones potential;

$$U(r) = 4\varepsilon\left[\left(\frac{\sigma}{r}\right)^{12} - \left(\frac{\sigma}{r}\right)^{6}\right], \tag{3.1}$$

where ε is the magnitude of the lowest potential value, and σ is the separation distance at which the energy is zero[49]. A simple sketch of the potential is given in Figure 3.2. In constant force mode, a control mechanism is employed to manage the cantilever deflection as measured by the photodetector, ensuring that the AFM probe tip and sample consistently stay in contact at a specified force. The measured signal is divided into two channels: the vertical regulation of the controller is recorded as the height, and the error signal used as input for the controller is recorded as the deflection[50, p. 13].

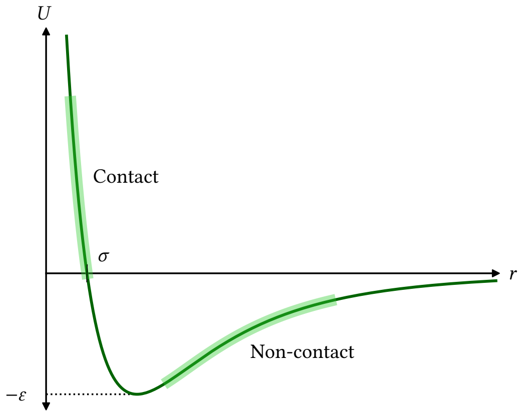

Figure 3.2: Lennard-Jones potential as a function of distance r between the tip and the sample. ε and σ are the parameters used in the mathematical expression of the potential given in Equation 3.1, being the magnitude of the lowest potential and the separation distance at which the energy zero, respectively. The regions of the curve used in contact and non-contact mode AFM are indicated.

The spatial resolution in AFM imaging is highly dependent on the tip size[50, p. 153]. Larger tips tend to flatten out finer features, and completely fail to detect holes and crevasses smaller than the tip radius. Although atomic resolution has been achieved by engineering the tip apex with atomically well-defined terminations[51], most practical applications do not require such a degree of precision. Since sharp tips tend to be less durable and less suitable for certain advanced techniques, various types of tips with distinct characteristics are employed for specific applications.

AFM utilizes three primary operational modes: contact mode, tapping mode, and non-contact mode, each characterized by the force-distance relationship of the cantilever interaction (Figure 3.2)[48]. In tapping and non-contact modes, a piezoelectric actuator induces vibrations at the cantilever base, causing the tip to oscillate. The optical detection system then records the variations in the amplitude and phase of these oscillations as a result of interactions with the sample surface. In contrast, in contact mode, the deflection is relayed back to the control system to regulate the vertical distance between the tip and sample, ensuring a constant interaction force. The primary disadvantage of contact mode is the increased wear on both the tip and sample as a result of the shear forces of the lateral movement of the tip. Consequently, the contact mode is not suitable for delicate samples, such as biological samples, polymer surfaces, and nanoparticles[48]. However, the proximity between the tip and the sample in contact mode enables the use of more advanced techniques to obtain detailed information about other the surface properties.

3.2 Piezoresponse Force Microscopy

Besides mapping the topography of the surface, scanning probe techniques can be applied to measure a range of physical properties of a sample, including ferroelectric domains. The standard tool for ferroelectric domain imaging is piezoresponse force microscopy (PFM)[25]. This technique utilizes the piezoelectric property shared by all ferroelectrics as basis for measuring the orientation of the ferroelectric polarization.

PFM operates in contact mode, with an oscillating voltage applied through the conductive tip. The electric field induced by the voltage provokes a piezomechanical response in the material, causing it to undergo a slight deformation from its original state. The tip oscillates with the sample, and these oscillations are detected by the laser beam reflected by the tip on the photodetector of the AFM setup. Finally, the signal from the photodetector is treated by a lock-in amplifier to extract the amplitude and phase of the data[25].

The oscillations in the tip is categorized into three contributions, which correlates to ferroelectric polarization in the three spatial dimensions. Out-of-plane polarization causes deflection of the cantilever, analogous to changes in topography, in-plane polarization parallel to the cantilever creates a shear force, causing a buckling of the cantilever, while in-plane polarization orthogonal to the cantilever applies a torque on the cantilever. The three contributions are recorded on a two-dimensional photodetector, where deflection and buckling are recorded as vertical signals and torsion is recorded as a lateral signals. As the two vertical signals can not easily be distinguished from each other, scans need to be recorded of a sample at in-plane rotations of 0°, 90° and 180° to be able to unambiguously discriminate each component of the polarization: a rotation of 90° interchanges the contributions from buckling and torsion, and a rotation of 180° inverts the response of buckling while leaving deflection intact. This technique of fully classifying the direction of the ferroelectric polarization is known as vector PFM[25].

Despite the rich number of possibilities for qualitative characterization using PFM, the technique has limited application for accurate quantitative measurements. This is often attributed to a strong dependence of the PFM contrast on the frequency of the applied voltage. Because of this, PFM data is commonly presented with arbitrary units for piezomechanical deformation[25].

3.3 Conductive Atomic Force Microscopy

A slightly different technique used for local electric characterization of materials is conductive atomic force microscopy (cAFM). In cAFM, the sample is scanned in contact mode, while a bias voltage is applied between the back electrode and the tip. The resulting current is measured at each probe position, creating a map of the local conductivity at the surface. A schematic of a cAFM setup is shown in Figure 3.3.

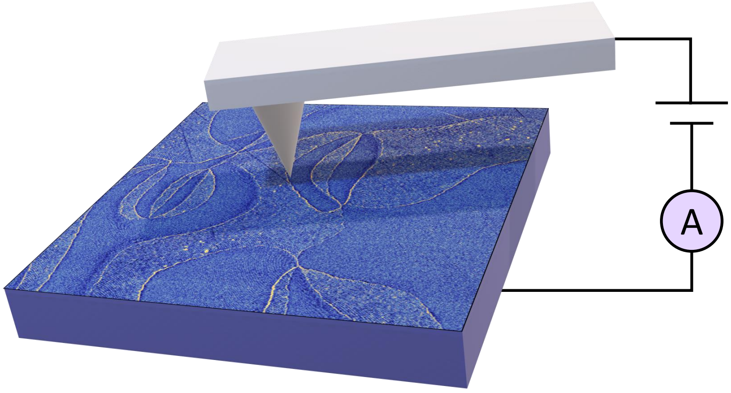

Figure 3.3: Simplified schematic of a cAFM setup. The image in the scan shows ferroelectric domains separated by conductive domain walls, indicated by the brighter lines.

However, one should exercise caution when interpreting the absolute numerical values obtained from cAFM. Several tip-dependenct factors influence the measured conductance, including the quality of the contact between the tip and the sample and other barriers. Additionally, decay of the conductive coating as the tip is dragged across the sample surface, leading to a reduction in measured current; and with a tip having an anomalous spring constant in the cantilever, a thin water film may form at the tip-sample junction[52].

Furthermore, within the bulk, the current spreads throughout the whole sample, and is only spatially confined close to the surface where the electric field from the tip is more localized. This is especially relevant for hexagonal manganites, where the hexagonal vortices divides the current between multiple paths within the domain wall network. Simulations on a virtual $ErMnO_3$ sample have showed that in a conductive tail-to-tail domain wall, 90 % of the cAFM contrast originates from a critical depth L_C of less than ~50 nm[41]. This depth varies with varies with the relative conductance of the domain compared to the bulk, and has been shown to scale with the intrinsic domain wall conductance σ_{DW} by the relation [41]

$$L_C \propto \sigma_{DW}^{0.7}. \tag{3.2}$$

3.3.1 Artifacts in cAFM imaging

As with every form of imaging, various artifacts emerge also in cAFM imaging, and it is omportant to keep these in mind to prevent drawing false conclusions.

cAFM is a rasterized technique, meaning that the data is obtained from scanning points distributed on a regular grid across the surface. This can cause issues of the sample contains periodic features with low periodicity compared to the scan grid. Such features are only be properly captured if the scan is able to sample the feature twice within a period. Otherwise, aliasing will occur, and the feature will appear to have a period in the scan larger than the physical reality. This effect is commonly encountered in other fields such as audio sampling. In cAFM, such aliasing occurs when the grid of sample positions overlaps with intrinsic periodic properties of the sample, and as a result, scanning Moiré patterns emerge in the final scan. For example, in layered materials such as $ErMnO_3$, the current signal varies depending on whether the surfacing layer consists of Er or MnO_5 polyhedra[53]. An illustration of this phenomenon is shown in Figure 3.4. The stripe-like Moiré fringes are an extrinsic feature of the scan, rather than a physical representation of the surface conductance.

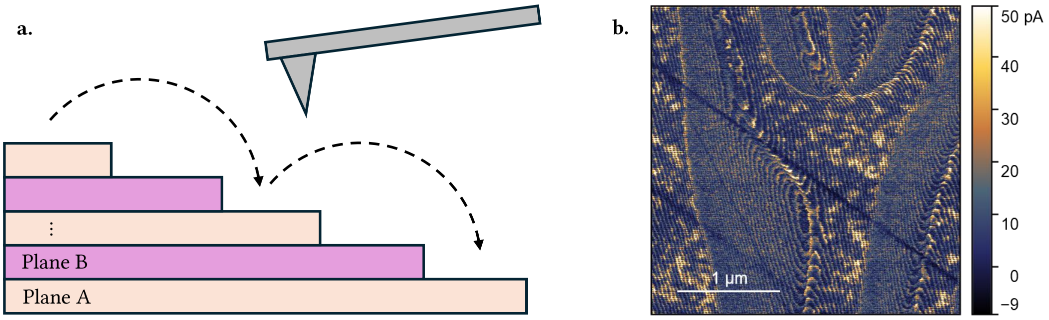

Figure 3.4: a. Schematic of a scanning probe measurement on a surface of a layered material with a periodic pattern in the surface termination layer between the two layers. The material is scanned with a periodicity close to the periodicity of the surface, and as a result only layer A is represented in the data. **b.** cAFM scan of a sample prevalent Moiré fringes. The scan was taken using a scan voltage of 2 V applied to the back electrode

Another effect that occurs when scanning ferroelectric domains is a scan-direction dependent increase in conduction when passing from an area with low conductance to an area with higher conductance. This creates an asymmetry in the data acquired by the forward and backward scan direction, and creates a pair of images where what looks like conductive domain walls is in compementary distribution across the domain walls. The origin of this artifact is possibly related to the sample topography, where a change in elevation influences the contact between the tip and the sample. Due to this, one should make sure features such as conductive domain wall are congruent in both scan directions.

3.4 Imaging of Ferroelectric Domains in Er(Mn, Ti)O_3

We have now introduced AFM, PFM and cAFM as three scanning probe techniques to be used for characterization of surfaces. A comparison of the data for each technique applied on out-of-plane domains in Er(Mn, Ti)O_3 is shown in Figure 3.5.

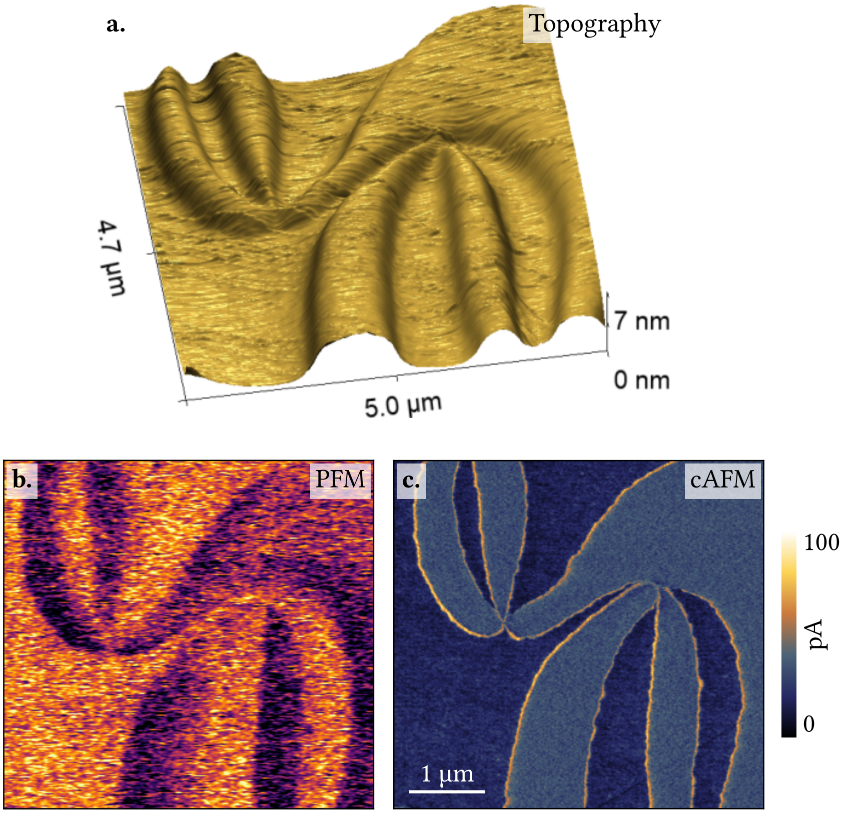

Figure 3.5: Comparison of three SPM techniques for domain imaging on Er(Mn, Ti)O_3. **a.** Contact mode AFM. **b.** PFM. **c.** cAFM. The cAFM scan was taken using a scan voltage of 3 V applied to the back electrode, and was acquired simultaneaously with the topographic scan.

The AFM scan shown in Figure 3.5a shows a topographical variation on the surface that aligns with the ferroelectric domain structure. High elevation correlates to the down domain, whereas low eleveation correlates to the up domain. The topographical variation between the high plateaus and low valleys has an order of magnitude around 10 nm. This variation arises during the sample preparation process, where bound charges form the ferroelectric polarization at the surface interact with various strenghts to the abrasive nanoparticles employed while chemomechanically polishing the surface, leading to a selective etching of the two domains.

Figure 3.5b shows a vertical PFM image of the same area as shown in the topographical scan, showing the contrast in piezoresponse from the two domains. This shows that the topographical variation of the AFM scan does indeed represent the ferroelectric polarization. Achieving high quality PFM data from Er(Mn, Ti)O$_3$ has proved challenging, as all PFM contrast is lost after scanning once. This allows for little wiggle room and possibility to fine tune scan parameters when scanning a specific area.

Figure 3.5c shows a cAFM scan acquired simultaneously with the topographical scan. As well as showing a domain contrast that can be correlated with the ferroelectric polarizations, cAFM provides information on the conductance of the domain walls. In this particular sample, the domain walls have enhanced conductance compared to the bulk, which is shown in the cAFM scan with a brighter color, as higher current passing through the domain wall.

3.4.1 Domain Contrast in cAFM

The cAFM contrast that can be correlated with the polarization of the ferroelectric domains is a feature unique to the case where there is an out-of-plane component of the polarization. This contrast is formed due to a mismatch in the work function of the metallic tip and the semiconducting ferroelectric at the interface between the two materials. At the surface of the ferroelectric semiconductor with out-of-plane polarization, there exists bound charges induced by the polarization discontinuity that alter the conduction and valence bands, E_C and E_V to maintain a uniform Fermi level E_F as shown in Figure 3.6a. This affects the Schottky barrier ϕ_B formed when the semiconductor and the metal are brought into contact, which for a p-type semiconductor is defined as the energy difference between E_C and E_F (Figure 3.6b). The ferroelectric modulation of the Schottky barrier $\Delta\phi_B$ relates to the proportion of current signal between the two domains by the relation

$$\Delta\phi_B = n k_\mathrm{B} T \ln\left(\frac{I_S^{\uparrow}}{I_S^{\downarrow}}\right), \tag{3.3}$$

where n is a constant called the ideality factor, k_B is the Boltzmann constant, T is the temperature, and $I_S^{\uparrow}$ and $I_S^{\downarrow}$ are the saturation currents of the up and

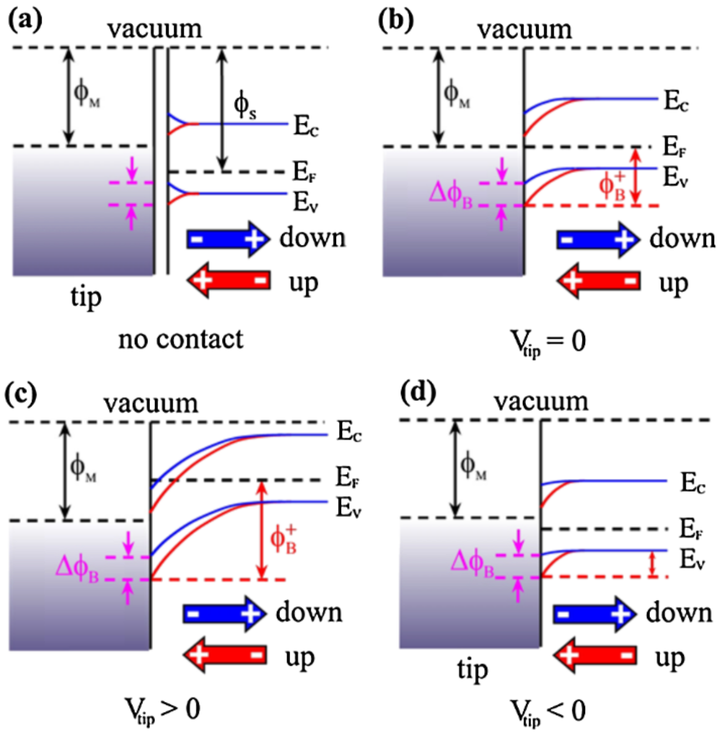
(a)
vacuum
ϕM
ϕs
Ec
EF
Ev
down
up
tip
no contact
(b)
vacuum
ϕM
Ec
EF
Ev
Δϕ_B
ϕ_B^+
down
up
V_tip = 0
(c)
vacuum
ϕM
Ec
EF
Ev
Δϕ_B
ϕ_B^+
down
up
V_tip > 0
(d)
vacuum
ϕM
Ec
EF
Ev
Δϕ_B
down
up
tip
V_tip < 0

Figure 3.6: Schematics of interfacial band diagrams between a metallic tip and a ferroelectric semiconductor with a component of the ferroelectric polarization normal to the surface. ϕ_M and ϕ_S are the work functions of the metal and semiconductor, respectively. E_V, E_C and E_F are the energies of the valence band, conduction band and the Fermi level, respectively. ϕ_B^+ is the Schottky barrier of the up domain, and $\Delta\phi_B$ is the difference in Schottky barrier between the two domains. The figure shows four situations: **a.** No contact between the tip and the ferroelectric. **b**. Contact between the tip and the ferroelectric, but no voltage applied. **c-d.** Contact between the tip and the ferroelectric with a bias voltage applied from the tip (c) and from the back electrode (d). *Reprinted with permission from Ref. [54].*

down domains, respectively[54].

When a bias voltage is applied over the sample, a change in E_F causes an equivalent change in the Schottky barrier, as shown in Figure 3.6c-d. The barrier increases when the bias is applied from the tip ($V_{\text{tip}} > 0$), while it decreases when the bias is applied from the back electrode ($V_{\text{tip}} < 0$). At high enough bias from the back electrode, the barrier is completely reduced, resulting in a shift in conduction mechanism to a space-charge limited conduction. In such cases, the contrast can invert between the two domains[54].

Experimental Methods 4

This work performed using the same samples as in my project work the previous semester, which are prepared and treated with identical procedures. For this reason, the experimental sections of this chapter are in their entirety borrowed from the equivalent section from my specialization thesis [55].

High quality monocrystalline $ErMn_{0.998}Ti_{0.002}O_3$ (from now on referred to as $Er(Mn, Ti)O_3$) crystals grown by the pressurized-floating zone method. They were then oriented using a Laue camera, and cut into bricks with a thickness of ~1 mm. To achieve a high quality surface for SPM measurements, the samples were chemomechanically lapped and polished using Al_2O_3 microparticles and SiO_2 nanoparticles, respectively.

4.1 Annealing

An Entec Tube Furnace was used for the annealing processes. The sample was placed in a sample holder and positioned in the middle of the tube, before closing the oven. As the temperature deviates from the set temperature towards the end of the tube, it is important to place the sample in the middle of the oven in order to be able to accurately control the heat subjected to the sample. The tube was evacuated with a vacuum pump until the pressure reached less than 0.5 mbar, and refilled with N_2 gas until near atmospheric pressure. The evacuation process was performed in total three times to ensure a pure atmosphere devoid of oxygen. N_2 gas was continuously flown through the tube throughout the annealing. Finally, a program was written on a Eurotherm EPC 3008 controller, with heating and cooling rates of 200 °C per hour, and dwell time and temperature depending on the experiment.

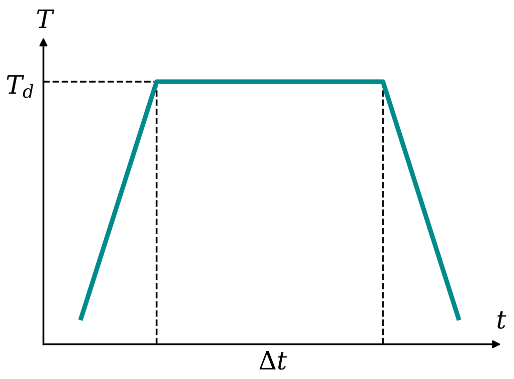

Figure 4.1: Schematic plot of an annealing with temperature T as a function of time t. Dwell time Δt and annealing temperature T_d are marked as the varied parameters.

4.2 SPM Measurments

Before doing SPM measurements, the sample was mounted to a specimen disc using either copper tape or silver paint. The surface was then cleaned using lens cleaning tissue soaked in acetone and methanol, before the sample was inserted into the microscope.

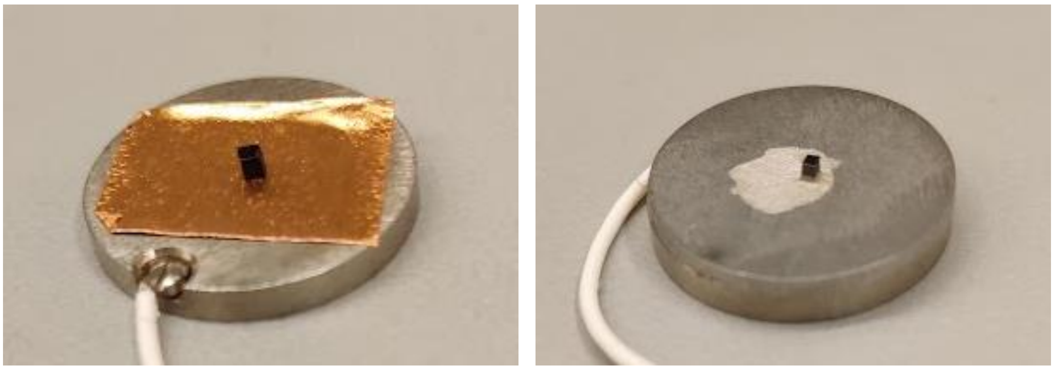

Figure 4.2: The sample mounted to the specimen disc using copper tape (left) and silver paint (right).

cAFM measurements were performed with a Cypher ES Environmental AFM by Asylum Research, and PFM measurements were performed using an NTEGRA Prima AFM by NT-MDT. A list of tips used in this project is shown in Table 4.1.

Table 4.1: List of tips used in this project. In the material column, a slash is used to indicate coatings; *e.g.* Pt/Si means platinum coated silicon. C indicates diamond.

Name	Manufacturer	Material	Tip Radius	Application
CDT-NCHR	NanoWorld[56]	C	< 200 nm	cAFM
DEP01	TipsNano[57]	C/Si	< 10 nm	cAFM & PFM
SPARK 70 Pt	NuNano[58]	Pt/Si	< 30 nm	PFM

In certain experiments, it was necessary to perform SPM scans at the same location within separate sessions. This was accomplished by marking the surface with a diamond scribing pen, which created reference points to locate and locate the scan sites. A topographic AFM overview image was captured in a distinct area that was easily identifiable from its surroundings. From this image, the desired scan location was selected and used for further imaging

4.3 Data Processing

The data from the scanning probe imaging was extracted using Gwyddion[59], either as images or raw data for further data processing.

cAFM data are 2-dimensional arrays of current values that show the local conductance over a selected are on the surface. While these data are commonly presented as images to give a visual impression of the surface electronical properties, they can as well serve as a basis for quantitative methods. As cAFM generally gives data with a considerable degree of noise, a method is needed that can express the range of current values while also showing the density over the range. As such, the resulting distribution can be divided into multiple contributions for various domains and domain walls.

4.3.1 Kernel Density Estimations

Kernel density estimation (KDE)[60] is a method of ascribing a density function, or estimating the probability function of a given set of values. The estimation revolves around by adding a collection of non-negative kernel functions $K(x)$ at each data point. The kernel weights the area close to the individual data points in such a way that the resulting function describes the density of the data.

For a mathematically rigid description of the estimation, we assume that there exists a distribution with an unknown density f at any pont x. From this distribution, we draw n independent samples, $(x_1, x_2, \dots, x_n)$, which will be used to create a reconstruction $\hat{f}$ of the original distribution. The kernel density estimation is then given by

$$\hat{f}_h(x) = \frac{1}{nh}\sum_{i=1}^{n} K\left(\frac{x - x_i}{h}\right), \tag{4.1}$$

where $h > 0$ is a smoothing parameter determining the width of each kernel, and thereby the roughness of the estimated distribution[60]. The optimal numerical value of h is dependent on the given distribution and sample size n, and is found by performing a variable sweep and subsequently observing the result. There exists a range of commonly used kernels, however particularly common is the standard normal distribution, [60]

$$K(x) = \frac{1}{\sqrt{2\pi}} e^{-\frac{x^2}{2}}. \tag{4.2}$$

The estimation was implemented in `Python` with the code given in Listing 1. This function takes three varables as input: `data` is the array of current values collected in the cAFM scan, and may be either two-dimensional or one-dimensional depending on previous processing. The optional parameters are the smoothing parameter `h` and the number of values in the final array `n`, which by default take the values 1 and 1000, respectively. The function calculates the density between the extreme values of the the input, and outputs arrays with corresponding x- and y-values.

```
import numpy as np

def kde(data: np.ndarray, h: float = 1, n: int = 1000)
                            -> tuple[np.ndarray, np.ndarray]:
    # Define the standard normal distribution as the kernel
    norm = 1 / np.sqrt(2 * np.pi)
    def kernel(z):
        return np.exp(-z*z / 2) * norm

    # Construct arrays for x and y
    x = np.linspace(data.min(), data.max(), n)
    y = np.zeros(n)

    # Add the kernel of each data point to y
    for val in data.flatten():
        y += kernel((x - val) / h)

    # Normalize the distribution
    y *= 1 / (data.size * h)

    return x, y

```

Listing 1: `Python` code showing the implementation of the kernel density estimations.

4.3.2 Image Thresholding

cAFM images of the samples include information from both the semiconducting background domains and the conductive domain walls of the sample. To distinguish between these domains and domain walls, a threshold is required to establish the boundary between the two categories. The Otsu method[61], a prevalent technique for image thresholding, aims to minimize the intra-class variance σ_w^2, defined as a weighted sum of the variances of the two classes,

$$\sigma_w^2(t) = \omega_0(t)\sigma_0^2(t) + \omega_1(t)\sigma_1^2(t), \tag{4.3}$$

where $\omega_i(t)$ and $\sigma_i^2(t)$ are the probabilities and variances of each class i (where $i = 0, 1$) with a given threshold t. This is equivalent to maximizing the inter-class variance, which is computationlly cheaper

$$\sigma_b^2(t) = \sigma^2 - \sigma_w^2(t) = \omega_0(t)\omega_1(t)\left[\mu_0(t) - \mu_1(t)\right]^2, \tag{4.4}$$

where $\mu_i(t)$ is the mean value for each class with theshold t[61]. Thresholding of the cAFM data was performed in `Python` with `scikit-image` image processing library[62], using the function `skimage.filters.threshold_otsu(hist = y)`, where `y` is the histogram of current values obtained from the kernel density estimation.

4.3.3 Bootstrap Sampling

While the Otsu thresholding algorithm is a great method for partitioning data, there is no inherent measure of uncertainty in the method. To find a metric for the uncertainty, we use a statistical bootstrapping[63]. This is a rather computationally intensive technique, but allows us to make inferences about from the data without making any strong assumptions about the distribution or statistics of the data. In this method, we construct new bootstrap samples by picking n random values with replacement from the original dataset with size n, until a total of m resamples are created. The Otsu threshold t_i is then calculated from each resampled dataset i, and the uncertainty of the threshold is inferred from the standard deviation of the set $(t_1, t_2, \ldots, t_m)$. This process is schematically illustrated in Figure 4.3.

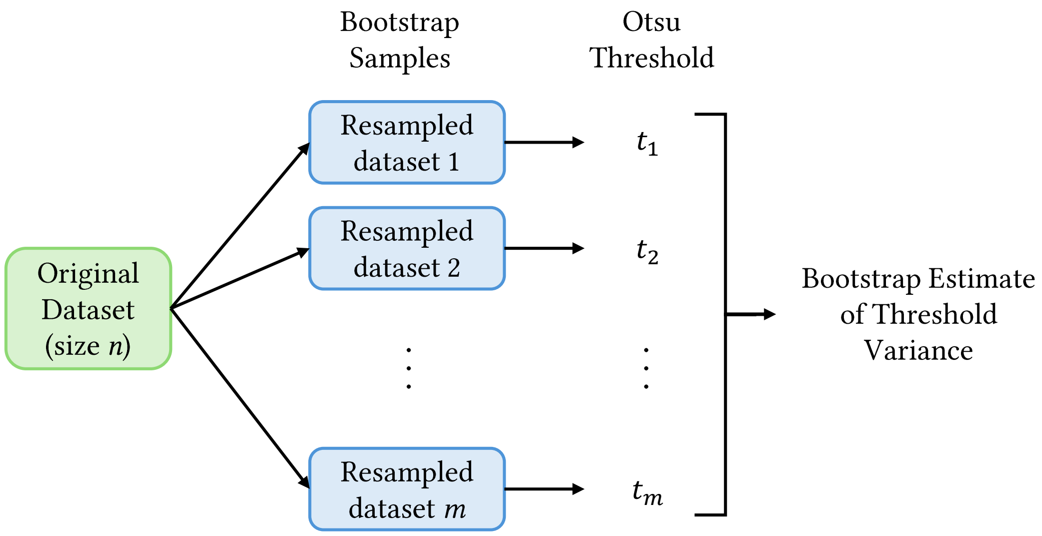
Bootstrap Samples
Otsu Threshold
Original Dataset (size n)
Resampled dataset 1
Resampled dataset 2
Resampled dataset m
t_1
t_2
t_m
Bootstrap Estimate of Threshold Variance

Figure 4.3: Schematic depiction of the steps of the bootstrapping algorithm.

Resampling of the cAFM data was performed in `Python` using the function `sklearn.utils.resample()` from the `scikit-learn` library[64] on the array of current values.

Mechanisms for Domain Wall Conductance

5

Previous work on Er(Mn, Ti)O_3 has shown that the electronic properties of the ferroelectric domain walls can be altered by annealing. By annealing in a reducing N_2 atmosphere, the electric conductance is enhanced to a greater extent than in the surrounding bulk. This process is reversible, and by annealing in an oxidating environment, for example in O_2, the enhanced conductance is neutralized. This tuning of the domain wcoolingnce is related with a chemical alteration of the material, and is therefore a strong implication that the enhanced domain wall conductance is ultimately rooted in the defect chemistry of the sample. However, the fundamental defect chemistry that governs the electronic properties of the domain walls is not well understood. Until now, a method of annealing at 300 °C has been used as a reliable method to generate Er(Mn, Ti)O_3 samples with enhanced domain wall conductance for more advanced research on domain wall electronics.

In this study, annealing experiments were conducted on Er(Mn, Ti)O_3 single crystals to generate samples featuring a variety of oxygen off-stoichiometries. Subsequently, the electronical properties within the domain walls were examined using cAFM. This study aimed to elucidate the correlation between defect chemistry and electronic properties of the domain walls and to deepen our understanding of the underlying mechanisms governing conductance in nominally neutral domain walls. As such, we can fine-tune the process in order to optimize sample preparation for future work on conductive domain walls.

5.1 Dependance on Annealing Parameters

The oxygen off-stoichiometry in hexagonal manganites can be controlled by managing the thermal and atmospheric history of the material [44, 45]. In particular, higher temperatures coupled with low partial oxygen pressure favor a reduction of the material and a decrease in the concentration of oxygen interstitials[45]. Furthermore, the process of annealing in oxygen-depleted atmospheres has been demonstrated to enhance domain wall conductance in Er(Mn, Ti)O_3, thereby indicating an interesting interplay between the defect chemistry and the electronic properties of the domain walls, with possible application in atmospheric sensing devices.

Annealing experiments were performed, systematically altering the annealing parameters. In particular, the parameter space spanned by the dwell time and annealing temperature was mapped, with the goal of constructing a “phase diagram” of the resulting conduction states of the domain walls. Such a map could give new insight into the relationship between the defect chemistry and the electronical properties that they bring on. All annealings were performed within a N_2 atmosphere, and with heating and cooling rates of 200 °C h^{-1}.

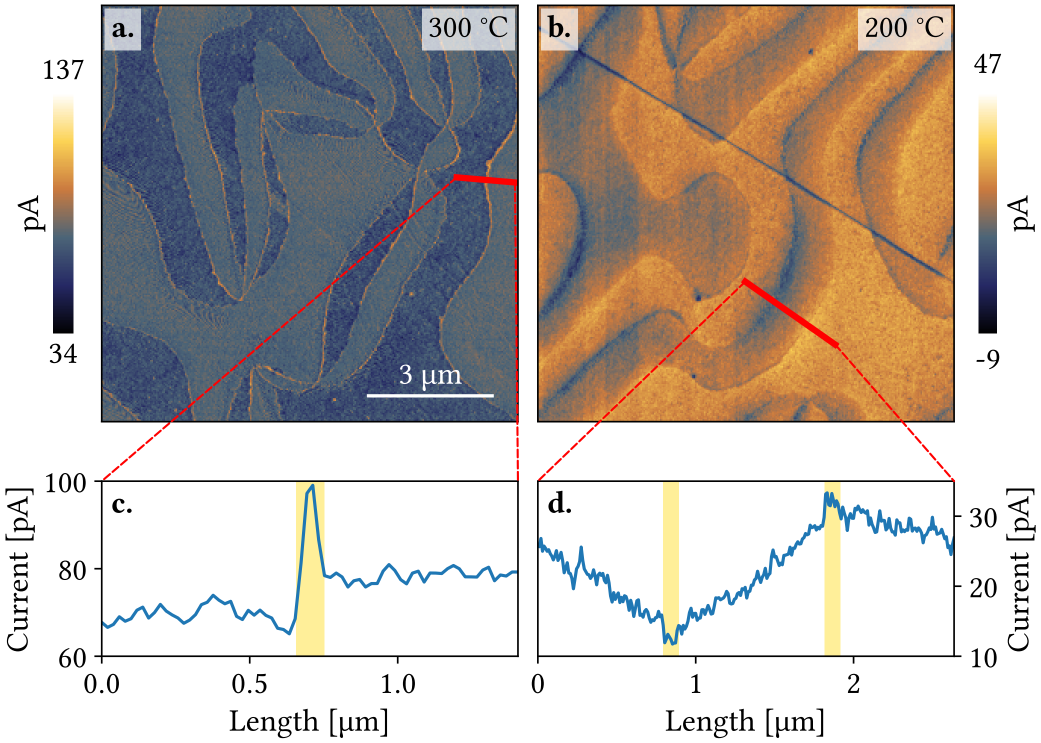

Figure 5.1: Conduction states of domain walls after annealing. **a.** cAFM scan of conductive domain walls induced by annealing at 300 °C for 24 hours. **b.** cAFM scan of insulating domain walls induced by annealing at 200 °C for 24 hours. The cAFM scans were taken using diamond coated silicon tips (DEP01) and with 4 V bias voltage applied to the back electrode. **c-d.** Current profiles of the domain walls marked by red lines in subfigure a and b, respectively. Yellow highlights indicate the position of the domain walls. The profiles are averaged over a width of 20 (c) and 40 (d) pixels (both resulting in a width of 400 nm due to different resolution of the images) to reduce noise in the data.

In a first step, the influence of the annealing temperature is investigated. Figure 5.1a shows a cAFM scan of a sample annealed at 300 °C for 24 hours, accompanied by a corresponding current profile along a domain wall shown in Figure 5.1c. The domain walls appear as bright lines in the scan, representing the locally enhanced conductance. This surfaces in the current profile as a sharp peak at the interface between the two domains.

A very different conductive behavior manifests in the domain walls when the sample is annealed at lowered temperatures. Figure 5.1b shows a cAFM scan of a sample annealed at 200 °C for 24 hours, accompanied by the corresponding current profile depicted in Figure 5.1d. In this case, the domain walls do not show the enhanced conductance exhibited by the sample annealed at the higher temperature. Instead, two distinct behaviors are prevalent: Some domain walls are more insulating than the surrounding bulk domains, whereas other domain walls are slightly more conductive than the bulk. These form an alternating pattern of increased and reduced conductance over a certain axis. This pattern has previously been reported[30], where subtle shifts in the orientation of the domain wall relative to the hexagonal c axis result in deviations from the charge neutral state, thereby altering the conductance of the domain wall. In principle, this variation in domain wall conductance applies to all samples, although it becomes more pronounced in the absence of an underlying conductive baseline.

Additionally, the current contrast of the domains between the domain walls acts as a gradient between the extrema the domain walls. A similar phenomenon is observed when imaging ferroelectric domains in scanning electron microscopy (SEM), where the underlying domain wall morphology influences the electron interactions within the sample to create a distinct contrast at the surface[65]. This behavior of the current profiles might originate from a similar interaction.

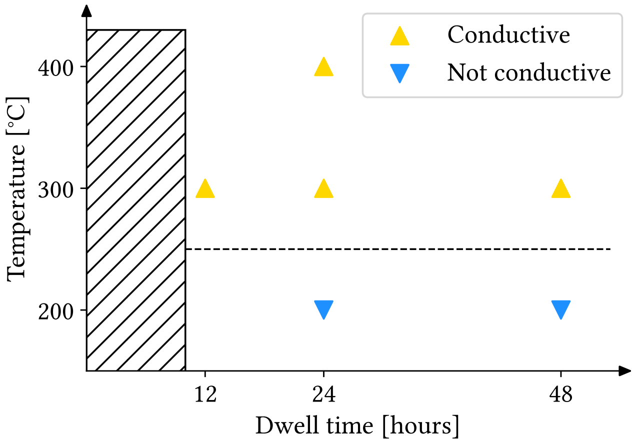

Figure 5.2: Summary of the performed annealing experiments, indicating the dwell time, temperature and the resulting domain wall conduction state. The dashed line indicates a hypothesized transition region between the sets of parameters giving conductive domain walls and the parameters that do not. The area representing dwell times of less than 12 hours are not considered in the following discussion due to a lack of data in the region.

We have collected data on the conduction states of the domain walls, derived from a diverse array of annealing parameters, which are summarized in Figure 5.2. For further detail, scans of each sample are shown in the supplementary figures in Appendix A.1. With this set of annealing parameters, we observe no immediate effects of the dwell time on the electronic properties of the domain walls. Instead, the variation correlates with the temperature under which the samples were kept. In particular, all annealings performed at 300 °C or higher were able to successfully enhance the conductance of all domain walls; whereas annealings at 200 °C resulted in the alternative state, where the conductive behavior of the domain walls is modulated to a greater extent by the intrinsic domain wall morphology. This reveals the existence of a critical temperature or a transitional range that must be exceeded in order for enhanced domain wall conduction to emerge in the range between 200 °C and 300 °C, although the thermal resolution of the experiments does not allow a more detailed determination of this transition.

We compare this to Remsen *et al.*'s work on gravimetric analysis of (Dy, Y)MnO_3, a similar hexagonal manganite[31]. When heating this material in oxygen, the oxygen off-stoichiometry increases between 200 °C and 300 °C, before desorbing oxygen at higher temperatures to reach the stoichiometric $P6_3cm$ phase at around 375 °C. Subsequently, oxygen reabsorbs into the material upon cooling to room temperature. In contrast, when annealing in a reductive H_2/N_2 atmosphere, the oxygen off-stoichiometry present at room temperature is reduced to reach the stoichiometric $P6_3cm$ phase between 200 °C and 300 °C, where it remains stable for an extended temperature range, before further decreasing. This corroborates our results that a change occurs within the material between these temperatures and that the stoichiometric phase is required for enhanced conductance to emerge at the domain walls.

5.2 Origin of Domain Wall Conduction

The conductance in nominally neutral domain walls is not affected by band bending at charged domain walls and must therefore be attributed to extrinsic effects, such as point defects providing donor or acceptor bands. DFT calculations on $YMnO_3$ predict an enhanced stability of interstitial oxygen ions in the domain walls, leading to an accumulation of oxygen ions, and thus enhanced conductance in the domain walls provided by the increase in negative charge carriers provided by these ions.[30] However, there is no experimental proof for this result. The theoretical calculations were performed in a bulk environment, and the presence of triple phase junctions where the domain walls meet the surface presents a completely different environment, which could lead to significant changes in the stability of defects and the electronic structure. In the absence of more detailed groundwork on this specific system, we work with the assumption that increased concentration of oxygen interstitial ions is the primary contributing factor toward enhanced conductance at the domain walls.

Although unintuitive at first glance, reducing the oxygen concentration in the sample is one method to enhance the domain wall conductance by creating an increased concentration of oxygen interstitials at the domain walls. Currently, there are two hypotheses about how reductive annealing enhances the conductance of the domain wall, which are illustrated in Figure 5.3. Firstly, the oxygen concentration on the entire surface of the sample is reduced from the initial value φ_0 to a lower value φ_s. The concentration would then increase on the domain wall by local reoxidation when the sample is reexposed to air (Figure 5.3a). Alternatively, annealing could cause a partial reduction in the sample, where more oxygen remains at the domain wall (Figure 5.3b). In either case, the relative oxygen concentration at the domain wall exceeds that of the bulk in the final state, resulting in the enhanced domain wall conductance.

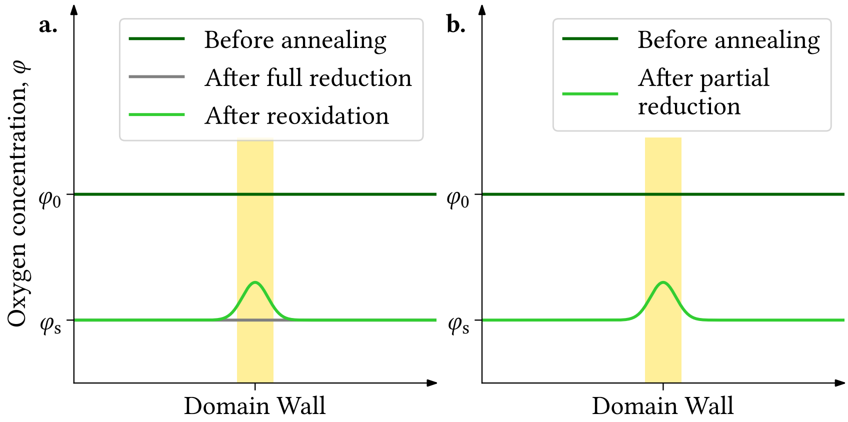

Figure 5.3: Oxygen concentration profiles over a domain wall describing two hypotheses for the origin of domain wall conductance. **a.** Annealing reduces the oxygen concentration universally across the sample, followed by a reoxidation at the domain walls. **b.** Annealing reduces the sample to various extents for domain walls and bulk, resulting in a higher concentration

In Section 5.1, we demonstrate two distinct states of domain wall conductance that can be induced by reductive annealing. In the following experiment, we perform further experiments to check if the samples undergo a change at room temperature. This could give further indications of the origin of the domain wall conductance and its relation to the annealing process.

The sample depicted in Figure 2.6b had previously been annealed at 200 °C for 24 hours, and thereby did not develop any enhanced domain wall conductance. Subsequently, we performed a second annealing at 300 °C for 24 hours, a treatment previously shown to increase domain wall conductance as illustrated in Figure 2.6a. A schematic of the annealing history and the resulting conductive behavior of the sample is shown in Figure A.9a, c and e. The sample exhibits the alternating behavior of insulating and slightly conductive domain walls seen in Figure 2.6b. The slightly enhanced conductance in some domain walls is not recorded in the opposite scan direction and stems in this case from an imaging artifact where the current signal is disproportionally increased in the transition into a region of relatively higher conductance in the scan direction. Additional data from a separate sample with an equal annealing history is shown in Appendix A.2.

In essence, it was not possible to treat the sample to induce conductive domain walls using techniques similar to those used with an "as-grown" sample. This hints that something changes in the underlying defect chemistry before the second annealing that prohibits further enhancement of the domain wall conductance in subsequent annealings.

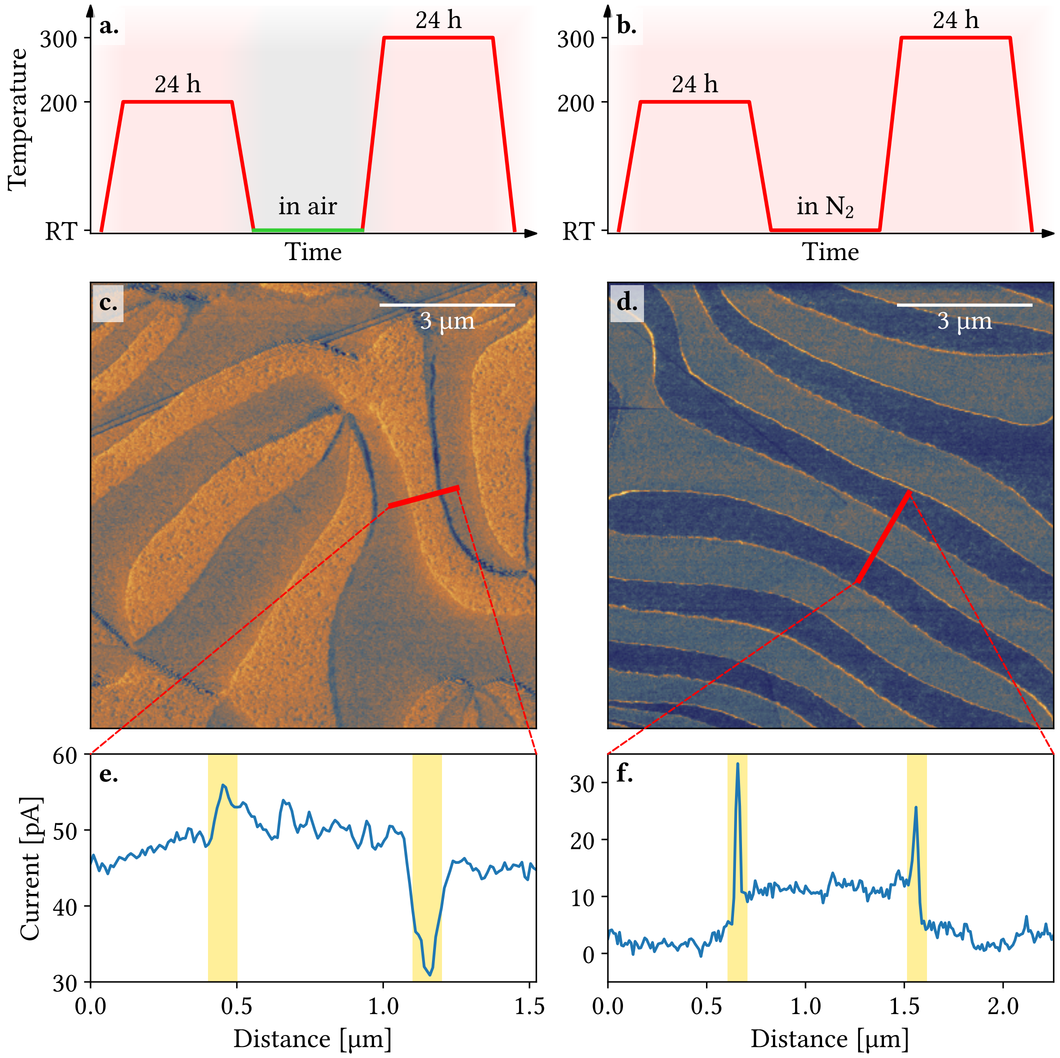

Figure 5.4: a-b. Annealing history of two samples. Both samples were first annealed at 200 °C for 24 hours, followed by an annealing at 300 °C for 24 hours; but in **a.** the sample was removed from the furnace between annealings, while in **b.** the sample was kept in the N_2 atmosphere. **c-d.** cAFM scans of the samples after the final annealing. The scans were taken using diamond coated silicon tips (DEP01) and with 6 V (c) and 2 V (d) bias voltages applied to the back electrode. **e-f.** Current profiles of the domain walls marked by red lines in subfigure a and b, respectively. Yellow highlights indicate the position of the domain walls. The profiles are averaged over a width of 40 pixels (equivalent to ~400 nm) to reduce noise in the data.

To explore the impact of annealing on the functional properties of domain walls, a novel annealing procedure was developed, merging the two processes into a single one: A new sample underwent a similar annealing process, initially at 200 °C for 24 hours, followed by 300 °C for another 24 hours. However, this time, the sample was maintained in a N_2 atmosphere without exposure to ambient air in a 24-hour rest period at room temperature between the annealing steps. A schematic of this annealing, together with a cAFM scan and a current profile over the domain walls is shown in Figure A.9b, d and f, respectively. In this case, the cunductance at the domain walls increased as expected from the latter annealing according to the results in Section 5.1.

These relatively similar annealing paths result in vastly different conductive behaviors of the domain walls. Being different only in the atmosphere in which the samples rest between annealings, the results stress the importance of the atmospheric history of the sample and the fact that important changes in the defect chemistry occur when the sample is exposed to ambient air after annealing. This supports the hypothesis that reoxidation at the domain walls after a full reduction of the sample is the key step for conductive domain walls to appear (Figure 5.3a). This result is corroborated by a previous finding that $Y(Mn, Ti)O_3$, a similar hexagonal manganite, is not "dead" with respect to oxygen diffusion even close to room temperature, and responds quickly to abrupt changes in the atmosphere[66].

Questions still remain regarding how the defect chemistry induced by exposing the sample to ambient air after annealings at 200 °C is able to block reoxidation to such an extent that conductive domain walls do not emerge. All of this suggests that the underlying mechanisms are more complex than what we can uncover by annealing and scanning with cAFM and that more specialized techniques are required to develop a full picture. Previous work has attempted to characterize the defect chemistry of the conductive domain walls using advanced techniques such as atom probe tomography (APT) and time-of-flight secondary ion mass spectrometry (TOF-SIMS), but no altered defect chemistry has been observed. This lack of conclusive evidence could be attributed to the high mobility of oxygen defects in the hexagonal manganites[66], and possibly relatively low defect concentrations. However, no such analysis has been performed on the insulating walls that arise from annealing at lower temperatures. If the insulation at the domain walls is caused by a separate mechanism, this could yield intriguing outcomes.

5.3 Constructing a Model for Oxygen Diffusion

After having tested a range of annealing parameters, we explore the diffusion mechanics of oxygen in an attempt to shed light on the internal defect chemistry governing the electrical properties at the domain walls. The reduction process undergone by the sample during the annealing is complex and depends on several material-dependent coefficients, including the diffusion coefficient, the exchange rate, and the defect formation energy. The following discussion will present a simplified model, and while we may not be able to draw definitive conclusions regarding the system, the model can point in the right direction for understanding the effects of the annealing parameters.

The diffusion of oxygen within a crystal lattice is described by Fick's second law, given by

$$\frac{\partial \varphi}{\partial t} = D\nabla^2\varphi, \tag{5.1}$$

where φ is the oxygen concentration, and D is the diffusion coefficient[42, p. 115]. If the bulk of the sample is sufficiently large compared to the surface region affected by diffusion, we can assume that the concentration is uniform across the surface and simplify the problem to a one-dimensional case. The solution to this partial differential equation depends largely on the initial and boundary conditions set for the system. To establish these conditions, we must adopt several assumptions: the initial oxygen content φ_0 is assumed to be uniform across the sample before any diffusion occurs. The concentration will remain at φ_0 in the bulk limit, *i.e.* the region sufficiently far from the surface will remain unaffected by the reduction in oxygen content. Lastly, the concentration at the surface φ_s is assumed to be temperature dependent and governed by the thermodynamic equilibrium given in Equation 2.14. The last assumption is made on the basis of the reducing N_2 atmosphere, which readily accepts the oxygen released from the material.

With these assumptions, Equation 5.1 solves analytically to give

$$\varphi(x,t) = \varphi_\mathrm{s}(T) + \varphi_\mathrm{v}(T)\,\mathrm{erf}\left(\frac{x}{2\sqrt{D(T)t}}\right), \tag{5.2}$$

where x is the distance from the surface into the bulk, $\varphi_\mathrm{v}(T) = \varphi_0 - \varphi_\mathrm{s}(T)$ is the equilibrium concentration of oxygen vacancies at the surface, and $\mathrm{erf}(x)$ is the error function evaluated at the point x. Disregarding the heating and cooling phases of the annealing process, this model outlines the oxygen concentration profile close to the surface and its dependence on the dwell time t and the temperature T. There are two temperature-dependent terms: the diffusion constant $D(T)$,

$$D \propto \exp\left(-\frac{E_\mathrm{A}}{k_\mathrm{B}T}\right), \tag{5.3}$$

where E_A is the activation energy for diffusion and k_B is the Boltzmann constant[42, p. 119]; and the equilibrium oxygen vacancy concentration $\varphi_\mathrm{v}(T)$ at the surface,

$$\varphi_\mathrm{v} \propto \exp\left(-\frac{Q_\mathrm{V}}{k_\mathrm{B}T}\right), \tag{5.4}$$

where Q_V is the formation energy of oxygen vacancies[42, p. 81]. As the reduction of the material occurs both via formation of oxygen vacancies and reduction of oxygen interstitials, we operate here with the vacancy concentration relative to the hypothetical fully oxidized $Er_3Mn_3O_{10}$[44], which is backed up by previous experimental observations in other hexagonal manganites[31, 67].

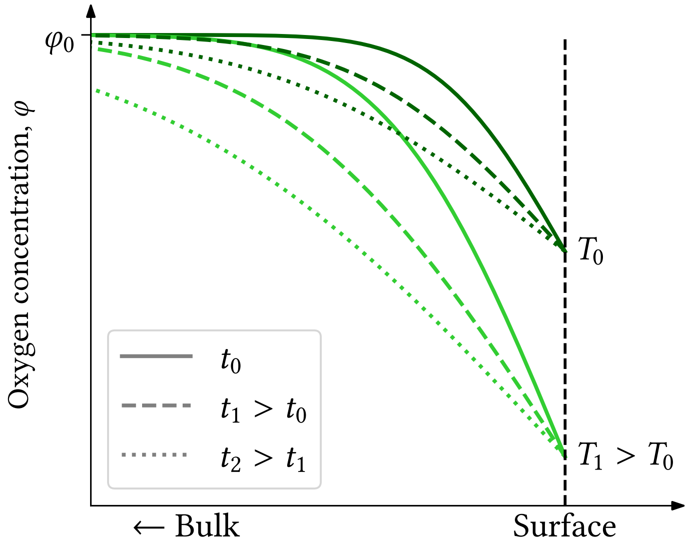

Figure 5.5: Oxygen concentration profiles according to the model described in this section for two temperatures T_0 and T_1, and three dwell times t_0, t_1 and t_2.

The predicted concentration profiles of oxygen are shown in Figure 5.5 for two annealing temperatures and three dwell times. At the surface, the concentration stays constant for the various dwell times, while increasing the temperature increases the number of vacancies. Deeper into the bulk, the concentration profiles are affected by both annealing parameters: Higher temperatures allow for more rapid diffusion, and together with prolonged dwell times, this allows the reduction in oxygen concentration to reach deeper into the bulk. If the defect chemistry of the surface is the main driving force determining the electronic properties of the domain walls, this agrees with the observed dependence on the annealing parameters shown in Figure 5.2, where the temperature was found to be the main influencing factor.

However, considerable simplifications have been implemented at the interface between the surface of the material and the air. In this model, only the thermodynamics of the junction is taken into account, specifically ensuring that the interface remains in a state that minimizes the surface free energy. A critical aspect influencing system behavior is the kinetics of mass transfer between phases, which critically influences whether any reaction occurs. Notably, this model would not have anticipated the plateau in thermogravimetric response around 300 °C as documented by Remsen *et al.* [31]. Nonetheless, it might be suitable to provide a qualitative intuition of the underlying processes. In addition, the numerical values of the parameters are key to developing a complete picture of the system. Further work is needed to construct a more complete model for oxygen diffusion that can accurately describe the dynamics of the defect chemistry and how it relates to the domain walls.

In conclusion, the results indicate that the moment of contact with air is crucial to enhance the conductance at the domain walls, and that passing a temperature between 200 °C and 300 °C is required during annealing for such development to occur. This is likely correlated with the formation of a stoichiometric $P6_3cm$ phase at this temperature.

Intrinsic Reversal of Annealing Effects

6

In Chapter 5, we studied the influence of the annealing parameters by monitoring the domain wall conductance of the samples shortly after the annealing. In addition to enhancing the domain wall conductance, a plethora of other changes occur while annealing Er(Mn, Ti)O_3 in an oxygen-depleted atmosphere that also can be observed using cAFM, including an increase of overall sample conductance and movement of domain walls. In this chapter we study a selection of these phenomena with regards to long-term effects as the samples expose to ambient condition over time.

An additional effect of the annealing in Chapter 5 is the formation of bubble domains. These are small, circular domains that forma a result of self-poling of the ferroelectric domains under annealing, and can provide us with information regarding the long-term behavior of the domain wall conductance, as well as defects.

6.1 Bubble Domains

A well-documented effect in the hexagonal manganites is the self-poling of domains on the surface due to electric fields caused by a charged particle concentration gradient: radiating the surface with an electron beam using scanning electrin microscopy (SEM)[68] and transmission electron microscopy (TEM) [69], and ion radiation in a focused ion beam (FIB) [70] have been shown to cause a change in the ferroelectric domain structure. Furthermore, this can be achieved by oxygen off-stoichiometry following a chemical reduction or oxidation. [71] A schematic of this process is shown in Figure 6.1a. When annealing in a reductive N_2 atmosphere, the concentration of oxygen ions at the surface decreases as oxygen exits the material, thereby inducing an inward directed electric field toward the bulk. This field favors the formation of down domains, and can manifest itself in local switching of the ferroelectric polarization. In contrast, annealing in an oxidating environment favors growth of the up domain[71].

Most commonly when we observe self-poling in Er(Mn, Ti)O_3, the polarization of the unit cells immediately next to the domain wall is switched, effectively moving the already present domain wall. This is exemplified in Figure 6.1b. In this illustration, the domain structure present before the annealing is identified by correlating the cAFM data with the topography of the surface. The surface coverage of the down domain is increased, potentially resulting in the merging of previously disjoint domains, provided that they share an equal antiphase.

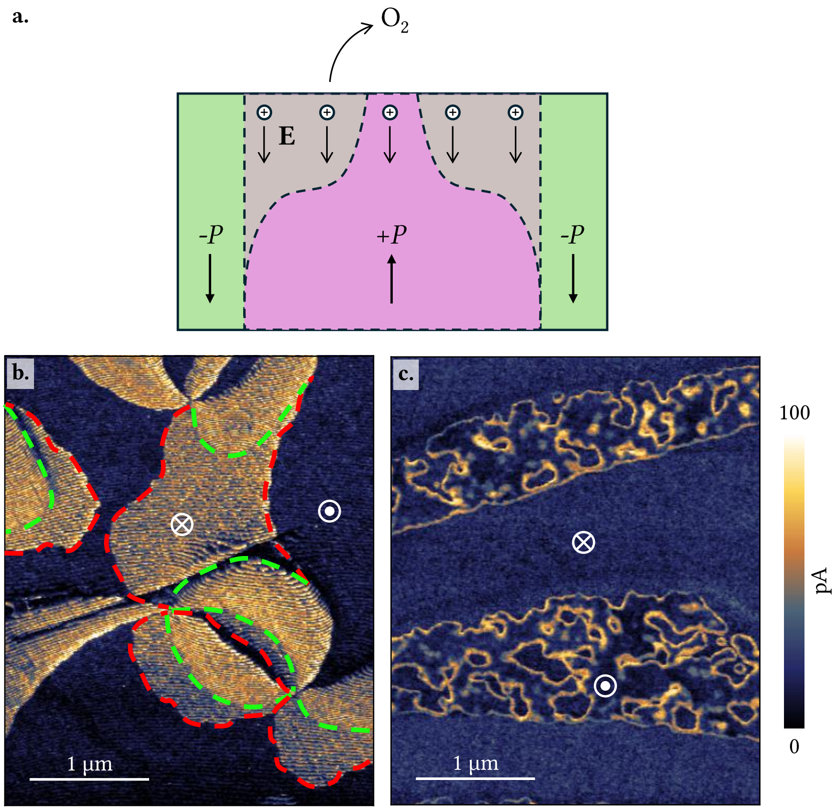

Figure 6.1: a. Schematic of the driving mechanism behind the growth of the down domain at the surface: When the oxygen concentration at the surface is reduced, a charge concentration gradient is formed, inducing an inward-directed elecric field **E** which switches the ferroelectric polarization at the surface. **b.** Domain growth with domains extending over the already present domain walls. The green and red lines highlight the domain wall configurations before and after annealing, respectively; while unmarked domain walls are unchanged. **c.** Bubble domains form by reductive The scans were acquired using a diamond coated silicon tip (DEP01) and with 4 V (b) and 3 V (c) bias voltages applied to the back electrode.

Another pattern of self-poling was also observed, where islands emerge within the up domain, forming bubble domains at the surface (Figure 6.1c). These bubble domains appear exclusively in the up domain with the interior having equal Schottky contrast with the down domain, confirming that these areas are indeed ferroelectric domains with opposite polarization to the domain in which they appear. Interestingly, the cAFM data show conductive domain walls surrounding the bubble domains, implying that also these domain wall have attracted interstitial oxygen over the course of the annealing. Similar bubble domains induced by switchin in SEM have previously been reported in $ErMnO_3$[70], but their properties have not yet been investigated in detail.

The morphology and behavior of the bubble domains varies between samples, and hint toward two possible growth mechanisms. The bubble domains of the sample shown in Figure 6.1c occasionally merge with the neighboring domains. In particular, bubble domains exclusively affiliate with only one of the neighboring domains, suggesting the existence of a preferred antiphase of the emergent domains. However, because of the symmetry of the system, such asymmetric behavior would be impossible, and the bubble domains would be expected to be equally distributed between the two antiphase states adjacent to the surrounding domain in the Landau free energy landscape (Figure 2.8). This preference may arise due to growth from underlying domains extending towards the surface, imparting the antiphase of the underlying domain to the bubble domains. Other samples show no such preference, suggesting that the bubble domains are truly isolated regions that nucleate and grow at the surface. The two proposed mechanisms for the formation of bubble domains are shown as a schematic in Figure 6.2.

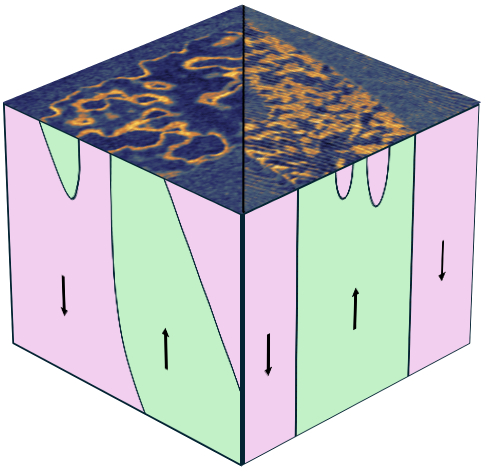

Figure 6.2: Schematic of the suggested growth mechanisms for bubble domains, showing plume growth (left) and island growth (right).

The formation of these bubble domains does not reveal any correlation with the annealing temperature or dwell time used in the annealing process to enhance the domain wall conduction. Extensive formation of bubble domains was observed in samples annealed at 300 °C for both 12 hours and 24 hours, while other samples with identical annealing routes did not develop bubble domains at all. Therefore, the formation of bubble domains is likely caused by other intrinsic factors. For example, electronic interactions on the ferroelectric surface are significantly influenced by the morphology of subsurface domain walls[41, 65], and the domain architecture of $ErMnO_3$ is modulated by externally applied mechanical pressures[72]. As such, we suggest that underlying domain structure, crystal strain and chemistry may be the primary driving force determining the specific mechanism for annealing-induced self-poling of the ferroelectic domains, and whether or not they occur in the first place.

Remarkably, the domain walls arising from self-poling also have enhanced conductance, similar to the already present domain walls. As the pattern of conductive domain walls reflects the post-annealed domain configuration rather than the pre-annealed configuration or an intermediate state, this presents another feature of annealing that could support the reoxidation hypothesis for the origin of domain wall conductance presented in Figure 5.3a. However, this phenomenon does not by itself exclude the possibility of contributions from other factors, such as oxygen migration both over the course of and after the annealing proceess.

6.1.1 Stability of Bubble Domains

To investigate the stability of the emergent bubble domains, we study a sample with cAFM at various times after the initial annealing. The resulting cAFM scans are shown in Figures 6.3a-d. For better visibility, the down domain which does not contain any bubble domains is grayed out. From inspecting the images, we see a reduction in the surface fraction of the bubble domains with time.

Figure 6.3e shows the current distribution of the up domain of each of the scans found using a kernel density estimation, to be used as a tool to quantify the bubble domains. To effectively quantify the extent of the bubble domains, the Otsu thresholding algorithm described in Section 4.3.2 is employed to separate the distribution of current values into two contributions, of which the part containing the lower current values is assigned to the background domain, and the higher current values represent the conductive domain walls surrounding the bubble doamins. As the bubble domains in this particular sample are small enough that the interior is not visible in the cAFM scans, the surface fraction of the surrounding conductive domain walls serve as a good approximation of the bubble domains, making thresholding a simple task. In the histograms in Figure 6.3e, the contribution identified as bubble domains is visually distinguished with a lighter overlay.

The area under the curves serves as a metric to quantify the percentage of the domain covered by bubble domains, which we use to quantify the decrease. As no inherent measure of uncertainty exists in the Otsu's algorithm, a series of bootstrap samples were resampled from the original data as described in Section 4.3.3, constructing a total of 100 bootstrap samples from each of which an the Otsu threshold is calculated. This gives us an array of values for the bubble domain coverage, from which we find the standard deviation. The resulting partitions of surface area between the bubble domains and the background domain with the corresponding uncertainty estimates over time is shown in Figure 6.3f. This confirms the visual interpretation of the raw scans, showing a decreasing trend with strong statistical significance.

This reduction of the bubble domains can be explained by the reoxidation of the sample after annealing. After being reexposed to ambient conditions following a reducing annealing, the material will gradually revert towards the original

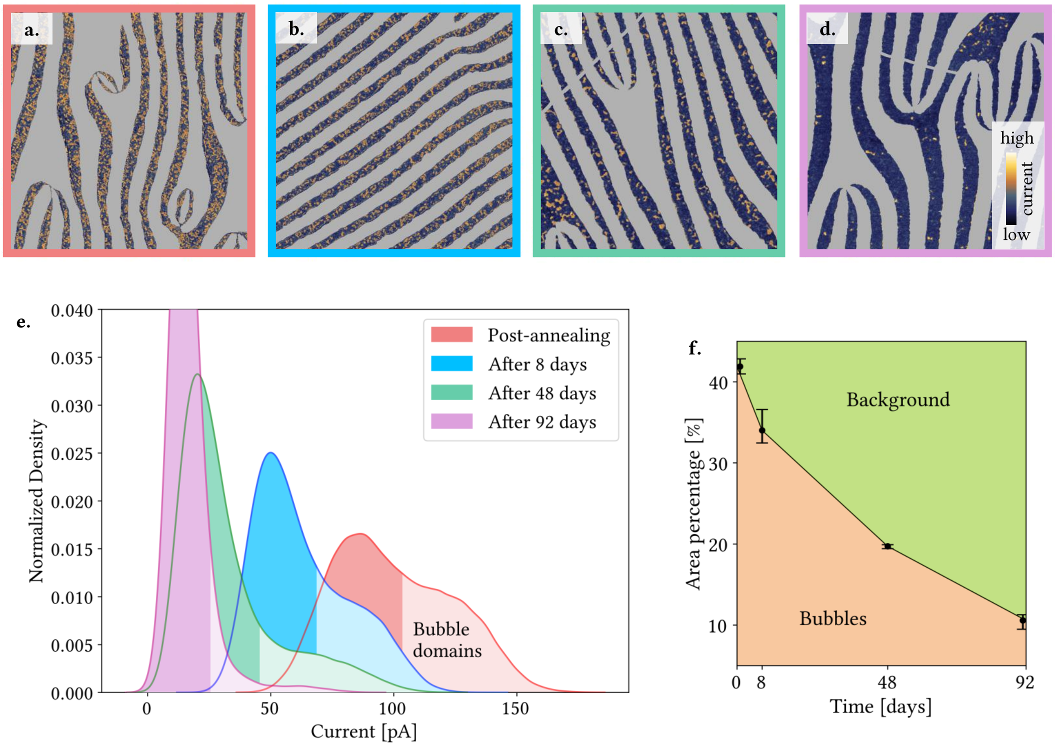

Figure 6.3: a-d. cAFM images of bubble domains in the up domain taken at various times after the initial annealing. The grey areas represent the down domains has been removed from the data. The images have dimensions $10 \times 10\ \mu m^2$ and were acquired using a diamond coated silicon tip (DEP01) and with a 4 V bias voltage applied to the back electrode. **e.** Histograms of current values of of the data in subfigures a-d with colors corresponding to the edge color of the respective scan. The curves are separated into two segments by treating the current values with the Otsu thresholding algorithm. Higher current values are associated with the domain walls surround the bubble domains. The sections representing the bubble domains are highlighted in a lighter color.

defect chemistry in the preannealed state by absorbing oxygen from the air. As the material is refilled with oxygen ions, the electric field induced by the ionic concentration gradient at the surface is neutralized, destabilizing the bubble domain. Consequently, the bubble domains gradually disappear, resulting in a lower fraction of the surface being covered.

Our analysis also showa that the enhanced conductance moves and disappears with the domain walls surrounding the bubble domains. Given that the heightened conductance at the neutral domain walls is associated with an increase in the number of negative charge carriers donated by oxygen interstitial ions[73], the passivation of the conductance necessarily suggests the simultaneous movement of oxygen defects with the domain walls. This shows the remarkable mobility of oxygen defects in the material, allowing the defects to move with the domain walls, which is less probable in other ferroelectrics[74]. As such, the walls of the neutral domain act as anchor points for oxygen defects, which then disperse throughout the material once they are no longer confined by the domain wall.

6.1.2 Control of Bubble Domains

In a next step, we attempt to actively manipulate the bubble domains by applying electric fields. As the bubble domains emerge from an electric field created by a charge gradient on the surface, it is expected that their number can be reduced by external electric fields counteracting the internal field. Such fields can be applied through a scanning probe[75]. Therefore, we use cAFM as an approach for local domain control, by applying a bias to the back electrode.

Figure 6.4a compares cAFM data of an area scanned for the first time (hence referred to as *pristine*) with an area subjected to external bias immediately prior to the scan. Visual inspection of the scan reveals the overall sample conductance to be reduced, both in the domains and domain walls. The overall density of bubble domains in the scanned area remains similar to the density in the pristine area.

In contrast, Figure 6.4b similarly compares a previously scanned area to its pristine surroundings, but in this case, there is a time span of 27 days between the first and the second scan. For comparison, Figure 6.4c shows the initial cAFM image taken of the pristine domains during the initial poling, corresponding to the boxed area in Figure 6.4b. Nearly all bubble domains originally present in the pristine scan have disappeared in the second scan, while the primary domain domain structure remains unchanged. The absolute current values are not comparable between Figure 6.4b and c, as the scans are taken using different biases. This contrasts starkly with the bordering pristine area (left side of Figure 6.4b), where the bubble domains are still present in the up domain, and the overall conductance of the sample is significantly higher than that of the previously scanned area.

This suggests that the degradation of bubble domains is not directly caused by, but is rather accelerated by the application of external electric fields. This demonstrates a spatially and temporally memristive behavior of the bubble domains, wherein the conductance of the sample informs on the spatial extent of the applied electric fields, while the concentration of bubble domains provides insights into the history of applied fields.

For further investigation, data from the pristine and scanned regions in Figure 6.4b were consolidated into the current distributions depicted in Figure 6.4d. The graphs resemble the distributions shown in Figure 6.3e, however, as we now include current values from both domains, the distributions distictly show two populations of current values, one for each domain. The intensity of each peak differs between the two regions, owing to the domain distributions influenced by the inherent domain structure of the sample. The impact of applying an external electric field mirrors that of letting the sample dwell in ambient conditions, creating narrower peaks centered at lower current values and with

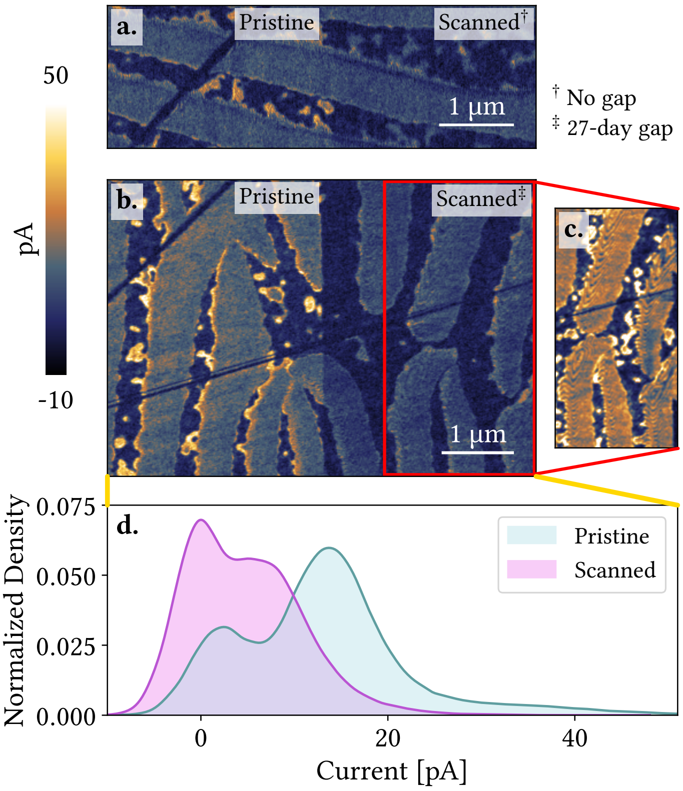

Figure 6.4: a-b. cAFM images containing two distinct halves: one pristine region not previously affected by external electric fields (left), and one area over which a cAFM scan has previously (right). The previously scanned area in (a) was scanned immediately prior, while the scanned area in (b) was scanned with a 27 day time gap. **c.** Pristine cAFM image of the scanned area in a., taken 27 days prior. The images were taken using diamond coated silicon tips (DEP01) and with 3 V (a-b) and 4 V (c) bias voltages applied to the back electrode. **d.** Density of current values from the pristine and scanned regions in (b).

less pronounced tails at higher current values representing conductive domain walls.

Our results reveal an exceptional flexibility for manipulation of the bubble domains. We next study the behavior of the bubble domains in the dependence of the applied voltage. Figure 6.5a shows a cAFM scan with a progressively increasing voltage over the horizonthal axis from left to right, enabling the examination of the immediate effects of the applied voltage. Naturally, a higher bias enhances the current flow through the sample, manifesting as a darker color on the left and a brighter color on the right.

The bubble domains demonstrate a remarkable shift in morphology as the bias increases: at lower scan biases, the bubbles surface mostly as domain wall rings with a visible interior; while at higher biases, the bubbles are smaller and dominated by the domain wall conductance. To quantify this, we partition the scan into four regions, and present the sizes of each region in violin plot in Figure 6.5b. The thickness of each violin presents the size distribution of the bubble domains of each population, found using a gaussian kernel density estimation. The areas between 1 V and 2 V were excluded from this measurement

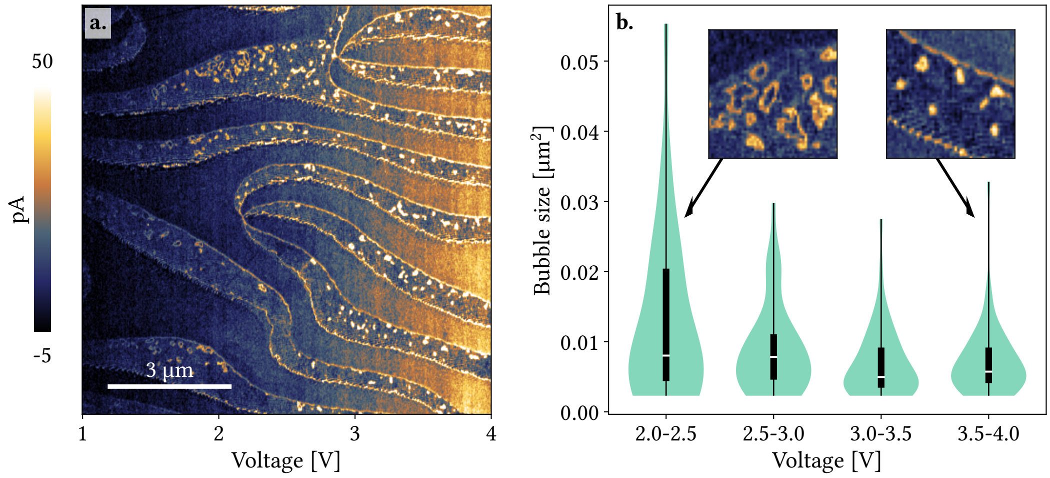

Figure 6.5: Reduction of bubble domain size with increased scan bias. **a.** cAFM scan with increasing bias voltage from 1 V to 4 V with evenly spaced increments of 0.1 V. The scan is performed using diamond coated silicon tips (DEP01) and with the voltage applied from the back electrode. **b.** Violin plot of the bubble domain size distribution, with the median and interquartile range marked in white and a thicker central line respectively. The insets exemplify the domains found in the respective bins and show areas of $1 \times 1\ \mu m^2$. A threshold of six pixels was set to eradicate contributions from noise. The sample size is $n \approx 50$ for all bins.

due to the inefficiency of thresholding in the low contrast regime. The bulk of the distributions are situated closely together, with the tails extending upwards of the lower biases being significantly more pronounced.

The local conduction contrast inverts between the up and down domains when increasing the bias voltage over a certain threshold around 3 V. At low bias, the current signal is brigher, *i.e.* the local conduction is higher in the up domains compared to the down domains. On the contrary, the down domains are brighter at higher biases. Wu *et al.* describes a similar shift in cAFM scans of $HoMnO_3$ as a change of conduction mechanism between the two regimes[54]. Low bias favors Schottky-like conduction with $I \propto \exp(V)$ due to the existence of a Schottky barrier at the tip-surface interface. At high bias, the system overcomes the Schottky barrier, and transitions to a space-charge limited conduction behavior with $I \propto V^2$. Due to the difference in Schottky barriers in the two polarization states, the transition is not synchronized between the states, enabling the conduction contrast to invert. However, on $HoMnO_3$ shows opposite behaviour from $ErMnO_3$, having increased local conduction in the up domains at high bias. The details of this contrast inversion go beyond the scope of this thesis, and will not be discussed further.

6.1.3 Parallels in Proper Ferroelectrics

Bubble domains are also reported in proper ferroelectrics like $Bi_{0.5}Na_{0.5}TiO_3$[76], $PtTiO_3$[77, 78], $PtZn_{0.5}Ti_{0.5}O_3$[79–81], and $BiFeO_3$[82]. In most cases, these polar structures require the low-dimensional stabilization of thin films, bilayers and heterostructures, but they have also been observed to form in a bulk environment[76]. These bubble domains are built from complex polar textures, including one or more of Néel and Bloch characteristics, and are commonly known as polar skyrmions. A common feature of all these proper ferroelectric bubble domains is a non-zero topological charge, or skyrmion number, N_{sk}, which plane-by-plane is given by

$$N_{\mathrm{sk}} = \frac{1}{4\pi} \iint \mathbf{n} \cdot \left(\frac{\partial \mathbf{n}}{\partial x} \times \frac{\partial \mathbf{n}}{\partial y} \right) \mathrm{d}x \, \mathrm{d}y, \tag{6.1}$$

where $\mathbf{n}$ is the normalized local dipole moment[83]. This provides them with a topological protection, which creates an energy barrier hindering the removal of the skyrmion.

Er(Mn, Ti)O_3, being an improper ferrolectric, exhibits a ferroelectric polarization restrained by the tilting of the MnO_5 bipyramids. As such, only the two orientations of the polarization parallel to the hexagonal c-axis are allowed in a relaxed structure, and the transition width between the uniaxial domains is effectively zero[84]. Whether or not these constraints permit the formation of skyrmionic structures is not yet clear.

6.2 Evolution of Domain Wall Conductance

According to our leading hypothesis, the enhanced conduction in the ferroelectric domain walls in Er(Mn, Ti)O_3 originates from a reduction of oxygen interstitial ions in the material during annealing. Subsequently, as the material relaxes in ambient conditions, oxygen will reenter the material as interstitial ions over time. This was concluded to be the primary factor attributing to the reduction in bubble domain coverage. Similarly, we would expect the conductance at the domain walls to be reduced as the material reoxidizes. In this section explores how the cAFM signal of the different domains changes over time

6.2.1 Domain Wall Conductance

In addition to the decrease in bubble domain coverage, the current signal of both the domain and the domain walls is reduced, as shown by the histograms in Figure 6.3e. To extract quantitative data from these distributions, we need a metric that consistently applies limits separating the current extent of the domain and the domain walls. We assume that the current signal from each population is normally distributed, with a well defined mean and standard deviation. Although fitting the histograms with a sum of Gaussian curves seems like a good strategy at first glance, this technique yields unphysical results in the extreme cases of the distributions. For example, the best Gaussian fit for the lower tails of the distributions representing the domain walls is a short but wide normal distribution which extends dubiously far into the lower current values associated with the background domains. Instead, we utilize a convenient property of the normal distribution that the mean and standard deviation is located on the first and second order critical points of the distribution function, respectively. All the current distributions in Figure 6.3e share a similar shape, having one first-order critical point at the global maximum which we define as the mean of the domain contribution; and four second-order critical points. These are distributed as shown in Figure 6.6a, with one located on the left side of the maximum, and three on the right side where they outline the tail constituting the domain wall contribution. We choose the first and second second-order critical point to represent the uncertainty of the domain contribution. The mean of the domain wall contribution is chosen to be the third second-order point, which marks the flattest point of the graph, and the forth point represents the upper uncertainty. Finally, only the lower uncertainty of the domain wall contribution remains, which is chosen to be on the Otsu threshold, which is located between the second and third second order critical points for all distributions.

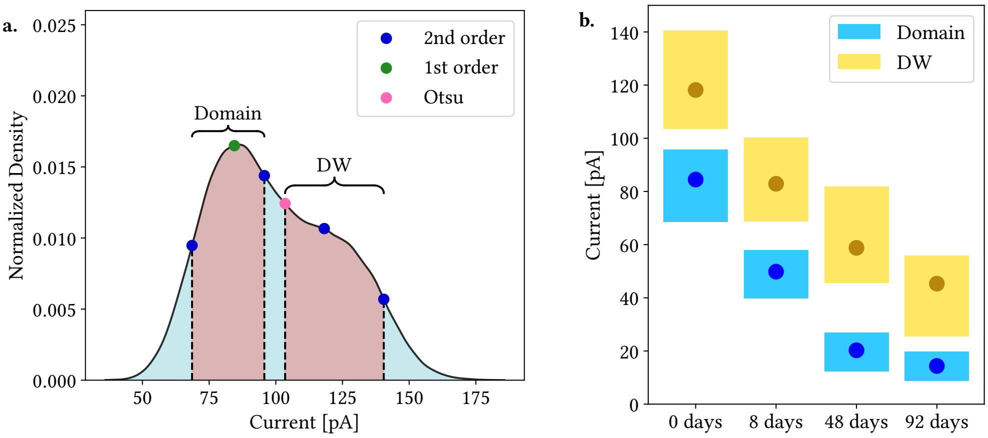

Figure 6.6: a. Histogram of current values from the cAFM scan in Figure 6.3a. The reference points used to identify the contribution from the domain and the domain walls are marked. **b.** Evolution of the domain and domain wall conductance over time.

Figure 6.6b shows the evolution of the conductance in the background up domain and the domain walls of the cAFM scans shown in Figure 6.3. The conductance shows a descending trend of exponential like decay over time for both populations. The reduction in overall sample conducance parallels an opposite change induced as an effect of annealing, where the overall conductance of the sample is reduced by an order of magnitude[73]. Therefore, it would be reasonable to conclude from the experimental observations that a reduction of oxygen interstitials increases the conductance of the material. However, this behavior is paradoxal when compared to previous DFT calculations, where insterstital oxygen was shown to be the primary source of p-type conductivity in the hexagonal manganites by governing the concentration of charge carrier holes[44]. Although the mechanisms for the increase in sample conductance after annealing remain unclear, we can still conclude that the material undergoes a change in the annealing which is slowly reversed as it dwells at room temperature.

6.2.2 Schottky Contrast between Domains

The evolution of the current signal over time present thus far follows a relatively simple pattern of reversing the increase in conductance obtained from annealing. However, a more complex story presents when considering both the domains, hinting at a profound connection between the defect chemistry of the sample and the physics governing the measured cAFM signal.

Figure 6.7 shows the same cAFM scans as in Figure 6.3, now with both domains included. The distributions of current values are calculated, and presented beside its respective scan. The distributions are fitted to a sum of two Gaussian curves to represent the two primary populations of each scan. Due to differences in contrast of the two domains and the large contribution from domain walls in the first scans, the populations that are fitted by the curves are not the same: In Figures 6.7b and 6.7d, one Gaussian curve fits the domain walls, while the other curve fits the combined peak of the up and down domains. In Figures 6.7f and 6.7h, the fitted peaks correspond to the two domains separately, and the contribution from the domain walls are not accounted for, or over-shadowed by one of the down domain. Similar presentations of data from different samples are shown in in the supplementary data in Appendix A.3.

The current values obtained from the two domains are summarized in Figure 6.8. The means and standard deviations are found from the normal distributions represented by the fitted Gaussian functions in Figure 6.7. The first two data points are the same for the two domains due the impracticality of separating the current distribution into distinct contributions. However, in the latter two scans, the domains behave differently. The conductance of the up domain decreases in exponential-like manner, as discussed in Section 6.2.1. In contrast, the conductance of the down domain remains constant, with minor variations that do not surpass the threshold for statistical significance.

The increase in Schottky contrast between the two domains may originate from several mechanisms. If reoxidation is the driving force for the decreased conductance of the down domain as discussed in Section 6.2.1, the absorbtion of oxygen could occur with different rates depending on the polarity of the bound charges at the surface. As indicatied by the chemical equation for formation of oxygen interstitials given in Equation 2.16, formation of oxygen interstitials is accompanied by oxidation of the Mn ions to form ions with a positive relative charge. Such positive ions would then be destabilized by the negative bound

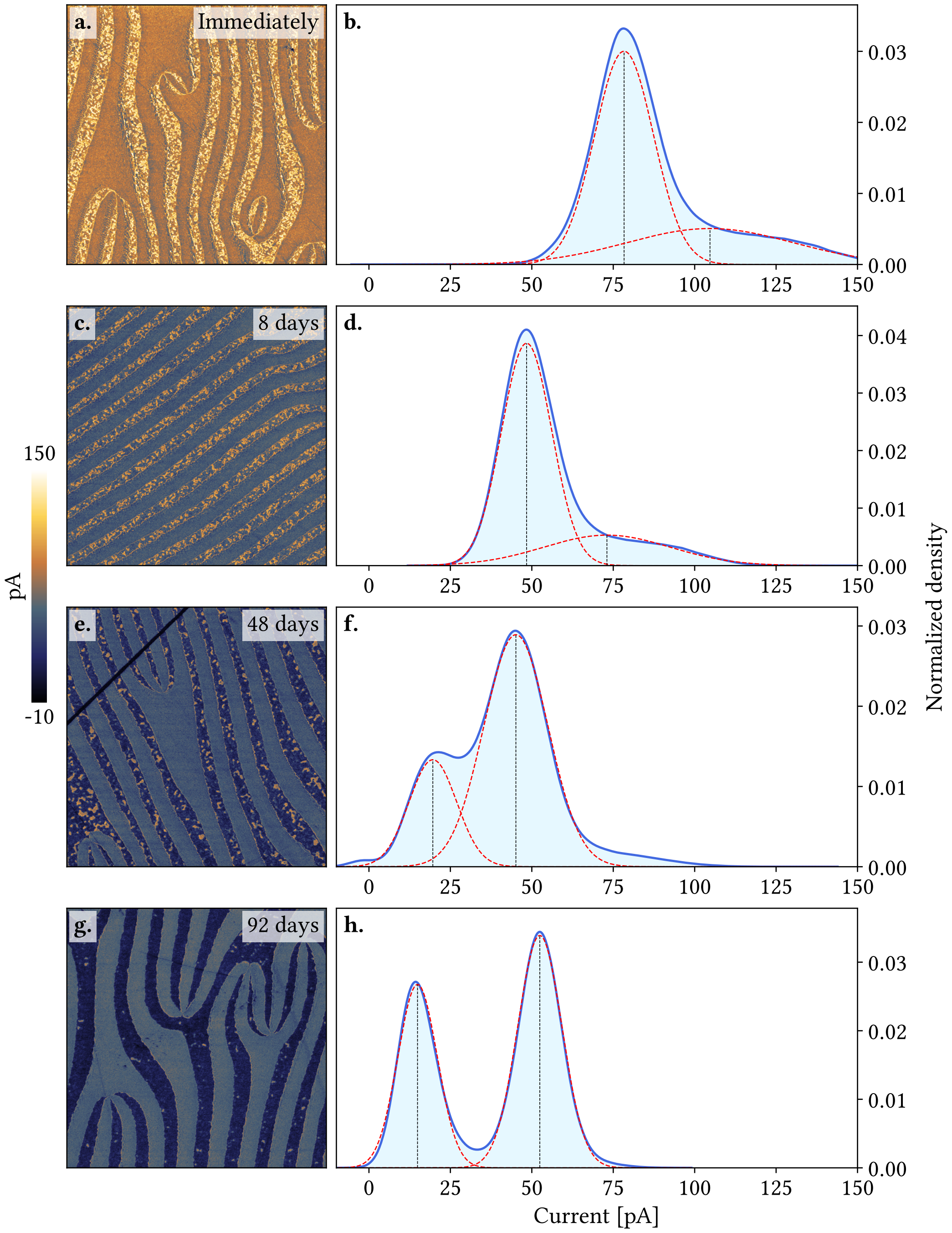

Figure 6.7: cAFM scans and corresponding current histograms of a sample acquired at different times after the original annealing. **a-b.** Immeaditely after annealing. **c-d.** 8 days after annealing. **e-f.** 48 days after annealing. **g-h.** 92 days after annealing. The histograms are fitted with two Gaussian functions to represent the two dominant populations of each scan. The peak of each Gaussian curve is marked with a black dotted line. The images have dimensions $10 \times 10\ \mu m^2$ and were acquired using a diamond coated silicon tip (DEP01) and with a 4 V bias voltage applied to the back electrode.

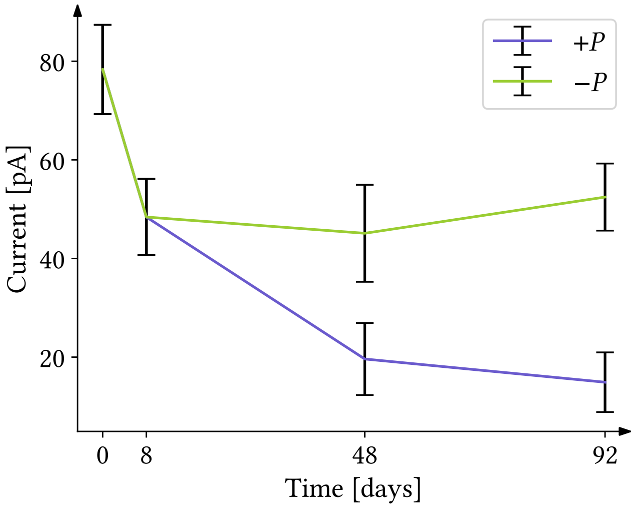

Figure 6.8: Evolution of the current signal from the domains over the four scans shown in Figure 6.7. The mean and standard deviations are extracted from the fitted Gaussian distributions in Figure 6.7.

charges at the surface, and cause an asymmetric reoxidation of the material. A similar argument could be applicable for the negatively charged interstitial oxygen formed among the positive surface charges in the up domain, however, the stability of these ions in their respective environments and the ability to diffuse away from the bound charges could influence the reaction rate in the different domain.

Another possible explanation is related to the change in the conduction mechanism over time. This relates back to Figure 6.5a, where an increase in voltage altered the mechanism for electronic conduction, causing an invertion of cAFM contrast between the two domains. The cAFM scan was recorded with evenly distributed increments of 0.1 V, and the current values from each voltage in the scan were combined to give an IV-curve comparing the two domains, shown in Figure 6.9. The measurement was started at 1 V, below which no contrast was discernable over the background noise. The measured conductance of the two domains is equal around 3 V, represented by the intersection of the curves. A similar inversion of current contrast was observed in multiple samples, though the inversion voltage varies from sample to sample, and might in some cases even be lower than the voltage needed to obtain domain contrast, resulting in no observable contrast inversion. The inversion voltage has shown to be annealing dependent: samples annealed at 300 °C have an inversion voltage close to the contrast threshold, while the inversion voltage is higher for samples annealed at 200 °C. However, this have not been studied in detail[55].

The increase in Schottky contrast could possibly be attributed to a lowering of the inversion voltage concurrent with the reoxidation of the material, and hint toward an intricate connection between the defect chemistry and electronic properties of the material beyond enhanced domain wall conductance. Although intriguing at first glance, this effect likely offers limited practical application,

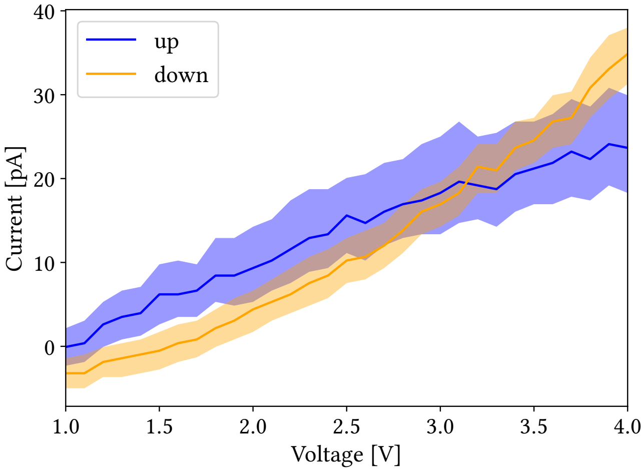

Figure 6.9: IV curves for the different constructed from the spatial medians of cAFM values from the scan shown in Figure 6.5a. The ranges of the values represent the inter-quartile range in each area. The bubble domains in the up domain are not accounted for, resulting in the wider range of values.

and would rather pose as an obstacle for precise quantitative analysis of domain walls in cAFM.

In this chapter, we have studied the long-term behavior of various effects caused in $Er(Mn, Ti)O_3$ by reductive annealing. Most importantly, a description of nanoscale bubble domains is given. These are metastable features of the material that gradually disappear over time, likely due to a reoxidation of the material. This reoxidation is also the source of other changes in the material, including a decrease in overall sample conductance and an increase in Schottky contrast between out-of-plane domains over time.

Conclusion and Outlook 7

This work aims to map the influence of reductive N_2 annealing on the conductance in nominally neutral domain walls in $Er(Mn, Ti)O_3$ by using various sets of annealing parameters. In particular, the parameter space spanned by the annealing temperature and dwell time was explored in relation to domain wall conductance, and the outcomes were analyzed using cAFM considering both immediate and long-term effects.

Annealing experiments demonstrated that the immediate conduction state of the domain walls depends primarily on the annealing temperature, with a threshold between 200 °C and 300 °C marking the boundary between processes that induce conductance and those that do not. This is corroborated by previous findings that report a reduction in oxygen interstitials to form a stoichiometric $P6_3cm$ phase in this temperature range[31]. More advanced annealing experiments were performed to delve deeper into the origin of domain wall conductance, revealing the reexposure of the sample to ambient conditions to be a key step in the development of conductive domain walls. The results indicate that the enhanced domain wall conductance is a result of a re-oxidation upon exposure to ambient conditions after the annealing cycle is completed. As a consequence, the function of the annealing primarily revlolves around preparing the defect chemistry of the material for subsequent contact with oxygen in the surrounding atmosphere.

The work also presents an overview of nanoscale bubble domains in $Er(Mn, Ti)O_3$ that emerge when the sample self-poles as a result of a charge concentration gradient formed during the reduction of the samples, which are the closest analog to polar skyrmions found in improper ferroelectrics. The bubble domains disappear over time, vulnerable to applied electric fields, and are therefore classified to be metastable features of the domain structure. Comparing regions subjected to external electric fields to unaffected regions reveals a memristive behavior of the bubble domains, where the spatial extent and time perspective of the applied electric fields is recorded in the density of bubble domains.

The behavior of the bubble domains solidifies previous findings of the remarkable mobility of oxygen interstitials in hexagonal manganites[66], and provides additional insight into the behavior of oxygen defects within ferroelectric domain walls. In agreement with the enhanced stability of oxygen defects in the neutral domain walls predicted by DFT[30], the domain walls act as anchor points for oxygen defects, and when the domain wall is removed, the oxygen defects that account for the increased domain wall conductance disperse into the material.

7.1 Future Work

The results lay the groundwork for studies of domain wall conductance by reporting the conduction state of the domain walls induced by the various annealing processes. However with these measurements we can only make vague assumptions about the underlying defect chemistry that govern the changes, and conclusions require to be drawn on the basis of calculations. To prove the presence of defects at the domain walls, advanced positional and elemental characterization techniques like APT and TOF-SIMS have been attempted, but evidence of any defect population at the domain walls has thus far been elusive due to the high mobility or relatively low concentration of oxygen interstitials. Going forward, the way to conclusively prove the will be through detailed modeling of the system, accounting for both oxygen migration within the material as well as over the surface-air boundary, and taking into account the different environment of the domain walls. Such modelling will require computationally demanding calculations due to the number of unit cells required to accurately represent the system, but could yield substantial support to the experimental findings.

With a thorough understanding of the underlying physics and engineering techniques for manipulating domain wall conductance, advanced research on the application of ferroelectric domain walls can be conducted. By connecting domain walls to external circuitry and exploiting their electronic capacities, we steadily advance toward domain wall based nanoelectronics.

Bibliography

Here are the references in citation order.

[1] John Presper Eckert Jr. and John W Mauchly. US3120606A. 1947 (cited on page 1).

[2] Gordon E. Moore. 'Cramming more components onto integrated circuits, Reprinted from Electronics, volume 38, number 8, April 19, 1965, pp.114 ff.' In: *IEEE Solid-State Circuits Society Newsletter* 11.3 (2006), pp. 33–35. DOI: `10.1109/N-SSC.2006.4785860` (cited on page 1).

[3] Jorge Íñiguez et al. 'Ferroelectric negative capacitance'. In: *Nature Reviews Materials* 4.4 (Apr. 2019), pp. 243–256. DOI: `10.1038/s41578-019-0089-0` (cited on page 1).

[4] Tae Yun Kim, Sung Kyun Kim, and Sang-Woo Kim. 'Application of ferroelectric materials for improving output power of energy harvesters'. In: *Nano Convergence* 5.1 (Nov. 2018), p. 30. DOI: `10.1186/s40580-018-0163-0` (cited on page 1).

[5] Cheol Seong H and Thomas Mikolajick. '11 - Ferroelectric memories'. In: *Advances in Non-Volatile Memory and Storage Technology (Second Edition)*. Ed. by Blanka Magyari-Köpe and Yoshio Nishi. Second Edition. Woodhead Publishing Series in Electronic and Optical Materials. Woodhead Publishing, 2019, pp. 393–441. DOI: `https://doi.org/10.1016/B978-0-08-102584-0.00012-7` (cited on page 1).

[6] M. Foeth, P. Stadelmann, and P.-A. Buffat. 'Quantitative determination of the thickness of ferroelectric domain walls using weak beam transmission electron microscopy'. In: *Ultramicroscopy* 75.4 (1999), pp. 203–213. DOI: `https://doi.org/10.1016/S0304-3991(98)00060-6` (cited on page 1).

[7] G. M. Guro B. M. Vul and I. I. Ivanchik. 'Encountering domains in ferroelectrics'. In: *Ferroelectrics* 6.1 (1973), pp. 29–31. DOI: `10.1080/00150197308237691` (cited on page 1).

[8] J Seidel et al. 'Conduction at Domain Walls in Oxide Multiferroics'. In: *Nature materials* 8 (Feb. 2009), pp. 229–34. DOI: `10.1038/nmat2373` (cited on pages 1, 2, 11).

[9] Peter Maksymovych et al. 'Tunable Metallic Conductance in Ferroelectric Nanodomains'. In: *Nano Letters* 12.1 (Jan. 2012), pp. 209–213. DOI: `10.1021/nl203349b` (cited on page 2).

[10] Tomas Sluka et al. 'Free-electron gas at charged domain walls in insulating BaTiO3'. In: *Nature Communications* 4.1 (May 2013), p. 1808. DOI: `10.1038/ncomms2839` (cited on page 2).

[11] Christoph S. Werner et al. 'Large and accessible conductivity of charged domain walls in lithium niobate'. In: *Scientific Reports* 7.1 (Aug. 2017), p. 9862. DOI: `10.1038/s41598-017-09703-2` (cited on page 2).

[12] Dennis Meier and Sverre M. Selbach. 'Ferroelectric domain walls for nanotechnology'. In: *Nature Reviews Materials* 7.3 (Mar. 2022), pp. 157–173. DOI: `10.1038/s41578-021-00375-z` (cited on pages 2, 7, 10).

[13] Lukas Puntigam et al. 'Strain Driven Conducting Domain Walls in a Mott Insulator'. In: *Advanced Electronic Materials* 8.10 (2022), p. 2200366. DOI: `https://doi.org/10.1002/aelm.202200366` (cited on pages 2, 10–12).

[14] D. Meier et al. 'Anisotropic conductance at improper ferroelectric domain walls'. In: *Nature Materials* 11.4 (Apr. 2012), pp. 284–288. DOI: `10.1038/nmat3249` (cited on pages 2, 11–13, 15).

[15] Kêitsiro Aizu. 'Possible Species of "Ferroelastic" Crystals and of Simultaneously Ferroelectric and Ferroelastic Crystals'. In: *Journal of The Physical Society of Japan - J PHYS SOC JPN* 27 (Feb. 1969), pp. 387–396. DOI: `10.1143/JPSJ.27.387` (cited on page 5).

[16] Joseph Valasek. 'Piezoelectric and Allied Phenomena in Rochelle Salt'. In: *Minutes of the Washington Meeting, April 23 and 24, 1920* XV.6 (Apr. 1920), pp. 537–538. DOI: `10.1103/physrev.15.505` (cited on page 5).

[17] V. K. Wadhawan. 'Towards a rigorous definition of ferroic phase transitions'. eng. In: *Phase transitions* 64.3 (1998), pp. 165–177 (cited on page 5).

[18] K. Bennemann and J.B. Ketterson. *Superconductivity*. eng. Berlin ; 2008 (cited on page 5).

[19] Shri Singh. 'Phase transitions in liquid crystals'. In: *Physics Reports* 324.2 (2000), pp. 107–269. DOI: `https://doi.org/10.1016/S0370-1573(99)00049-6` (cited on page 5).

[20] V. Wadhawan. *Introduction to Ferroic Materials*. Taylor & Francis, 2000 (cited on pages 5, 7).

[21] S. Elliott. *The Physics and Chemistry of Solids*. Wiley, 1998, pp. 563–566 (cited on pages 6, 8).

[22] G.L. Pollack and D.R. Stump. *Electromagnetism*. Addison Wesley, 2002 (cited on pages 6, 9, 10).

[23] J. Nordlander et al. 'The ultrathin limit of improper ferroelectricity'. In: *Nature Communications* 10.1 (Dec. 2019), p. 5591. DOI: `10.1038/s41467-019-13474-x` (cited on page 7).

[24] Frank Peter. *Piezoresonse Force Microscopy and Surface Effects of Perovskite Ferroelectric Nanostructures*. Vol. 11. Forschungszentrum Jülich GmbH, 2006 (cited on page 7).

[25] Elisabeth Soergel. 'Piezoresponse force microscopy (PFM)'. In: *Journal of Physics D: Applied Physics* 44.46 (2011), p. 464003. DOI: `10.1088/0022-3727/44/46/464003` (cited on pages 8, 23, 24).

[26] G. Catalan et al. 'Domain wall nanoelectronics'. In: *Rev. Mod. Phys.* 84 (1 Feb. 2012), pp. 119–156. DOI: `10.1103/RevModPhys.84.119` (cited on page 9).

[27] Donald Evans et al. 'Domains and domain walls in multiferroics'. In: *Physical Sciences Reviews* -1 (Apr. 2020). DOI: `10.1515/psr-2019-0067` (cited on pages 9, 10).

[28] Salia Cherifi-Hertel et al. 'Shedding light on non-Ising polar domain walls: Insight from second harmonic generation microscopy and polarimetry analysis'. In: *Journal of Applied Physics* 129 (Feb. 2021), p. 81101. DOI: `10.1063/5.0037286` (cited on pages 10, 11).

[29] G. F. Nataf et al. 'Domain-wall engineering and topological defects in ferroelectric and ferroelastic materials'. In: *Nature Reviews Physics* 2.11 (Nov. 2020), pp. 634–648. DOI: `10.1038/s42254-020-0235-z` (cited on pages 10–12).

[30] J. Schultheiß et al. 'Intrinsic and extrinsic conduction contributions at nominally neutral domain walls in hexagonal manganites'. In: *Applied Physics Letters* 116.26 (July 2020), p. 262903. DOI: `10.1063/5.0009185` (cited on pages 12, 18, 19, 37, 38, 59).

[31] Steven Remsen and Bogdan Dabrowski. 'Synthesis and Oxygen Storage Capacities of Hexagonal $\mathrm{Dy}_{1-x}\mathrm{Y}_x\mathrm{MnO}_{3+\delta}$'. In: *Chemistry of Materials* 23.17 (Sept. 2011), pp. 3818–3827. DOI: `10.1021/cm2006956` (cited on pages 13, 18, 38, 43, 59).

[32] B. Lorenz. 'Hexagonal Manganites—($R\mathrm{MnO}_3$): Class (I) Multiferroics with Strong Coupling of Magnetism and Ferroelectricity'. In: *ISRN Condensed Matter Physics* 2013 (Feb. 2013), p. 497073. DOI: `10.1155/2013/497073` (cited on page 13).

[33] Sandra H. Skjærvø et al. 'Unconventional Continuous Structural Disorder at the Order-Disorder Phase Transition in the Hexagonal Manganites'. In: *Phys. Rev. X* 9 (3 July 2019), p. 031001. DOI: `10.1103/PhysRevX.9.031001` (cited on page 13).

[34] S. C. Chae et al. 'Direct Observation of the Proliferation of Ferroelectric Loop Domains and Vortex-Antivortex Pairs'. In: *Phys. Rev. Lett.* 108 (16 Apr. 2012), p. 167603. DOI: `10.1103/PhysRevLett.108.167603` (cited on page 13).

[35] Manfred Fiebig et al. 'The evolution of multiferroics'. In: *Nature Reviews Materials* 1.8 (July 2016), p. 16046. DOI: `10.1038/natrevmats.2016.46` (cited on page 13).

[36] Sergey Artyukhin et al. 'Landau theory of topological defects in multiferroic hexagonal manganites'. In: *Nature Materials* 13.1 (Jan. 2014), pp. 42–49. DOI: `10.1038/nmat3786` (cited on pages 13, 14).

[37] Koichi Momma and Fujio Izumi. '*VESTA3* for three-dimensional visualization of crystal, volumetric and morphology data'. In: *Journal of Applied Crystallography* 44.6 (Dec. 2011), pp. 1272–1276. DOI: `10.1107/S0021889811038970` (cited on page 13).

[38] Bas B. Van Aken, Auke Meetsma, and Thomas T. M. Palstra. 'Hexagonal $ErMnO_3$'. In: *Acta Crystallographica Section E* 57.6 (June 2001), pp. i38–i40. DOI: `10.1107/S160053680100811X` (cited on page 13).

[39] Quintin N. Meier et al. 'Manifestation of structural Higgs and Goldstone modes in the hexagonal manganites'. In: *Phys. Rev. B* 102 (1 July 2020), p. 014102. DOI: `10.1103/PhysRevB.102.014102` (cited on page 13).

[40] Jun Li et al. 'Homotopy-Theoretic Study & Atomic-Scale Observation of Vortex Domains in Hexagonal Manganites'. In: *Scientific Reports* 6.1 (June 2016), p. 28047. DOI: `10.1038/srep28047` (cited on page 15).

[41] Erik D. Roede et al. 'The Third Dimension of Ferroelectric Domain Walls'. In: *Advanced Materials* 34.36 (2022), p. 2202614. DOI: `https://doi.org/10.1002/adma.202202614` (cited on pages 15, 25, 47).

[42] William D. Callister. *Materials Science and Engineering: An Introduction, 7th Edition*. Wiley, 2007 (cited on pages 16, 18, 42, 43).

[43] K.A. Dill and S. Bromberg. *Molecular Driving Forces: Statistical Thermodynamics in Biology, Chemistry, Physics, and Nanoscience*. Garland Science, 2011 (cited on page 17).

[44] Sandra H Skjærvø et al. 'Interstitial oxygen as a source of p-type conductivity in hexagonal manganites'. In: *Nature communications* 7 (Dec. 2016), p. 13745. DOI: `10.1038/ncomms13745` (cited on pages 18, 19, 35, 43, 55).

[45] Sandra H. Skjærvø et al. 'Oxygen vacancies in the bulk and at neutral domain walls in hexagonal $YMnO_3$'. In: *Phys. Rev. B* 98 (18 Nov. 2018), p. 184102. DOI: `10.1103/PhysRevB.98.184102` (cited on pages 19, 35).

[46] F.A. Kröger and H.J. Vink. 'Relations between the Concentrations of Imperfections in Crystalline Solids'. In: ed. by Frederick Seitz and David Turnbull. Vol. 3. Solid State Physics. Academic Press, 1956, pp. 307–435. DOI: `https://doi.org/10.1016/S0081-1947(08)60135-6` (cited on page 19).

[47] G. Binnig, C. F. Quate, and Ch. Gerber. 'Atomic Force Microscope'. In: *Phys. Rev. Lett.* 56 (9 Mar. 1986), pp. 930–933. DOI: `10.1103/PhysRevLett.56.930` (cited on page 21).

[48] Nader Jalili and Karthik Laxminarayana. 'A review of atomic force microscopy imaging systems: application to molecular metrology and biological sciences'. In: *Mechatronics* 14.8 (2004), pp. 907–945. DOI: `https://doi.org/10.1016/j.mechatronics.2004.04.005` (cited on pages 21, 23).

[49] Johann Fischer and Martin Wendland. 'On the history of key empirical intermolecular potentials'. In: *Fluid Phase Equilibria* 573 (2023), p. 113876. DOI: `https://doi.org/10.1016/j.fluid.2023.113876` (cited on page 22).

[50] Fangzhou Xia, Ivo W. Rangelow, and Kamal Youcef-Toumi. *Active Probe Atomic Force Microscopy: A Practical Guide on Precision Instrumentation*. Cham: Springer International Publishing, 2024 (cited on page 22).

[51] Leo Gross et al. 'The Chemical Structure of a Molecule Resolved by Atomic Force Microscopy'. In: *Science* 325.5944 (2009), pp. 1110–1114. DOI: `10.1126/science.1176210` (cited on page 22).

[52] Lanlan Jiang et al. 'Understanding Current Instabilities in Conductive Atomic Force Microscopy'. en. In: *Materials (Basel)* 12.3 (Feb. 2019) (cited on page 24).

[53] L. Richarz et al. 'Moiré fringes in conductive atomic force microscopy'. In: *Applied Physics Letters* 122.16 (Apr. 2023), p. 162903. DOI: `10.1063/5.0145173` (cited on page 25).

[54] Weida Wu et al. 'Polarization-Modulated Rectification at Ferroelectric Surfaces'. In: *Phys. Rev. Lett.* 104 (21 May 2010), p. 217601. DOI: `10.1103/PhysRevLett.104.217601` (cited on pages 28, 52).

[55] Egil Ytterli Tokle. 'Oxygen-Driven Nano-Engineering for Functional Ferroelectric Domain Walls'. Project thesis. Trondheim: NTNU, Dec. 2023 (cited on pages 29, 57, 76).

[56] NanoWorld®. *CDT-NCHR — nanoworld.com*. `https://www.nanoworld.com/pointprobe-conductive-diamond-coated-tapping-mode-afm-tip-cdt-nchr`. [Accessed 11-06-2024] (cited on page 30).

[57] TipsNano®. *DEP01 — tipsnano.com*. `https://tipsnano.com/catalog/afm-special/scd/dep01/`. [Accessed 11-06-2024] (cited on page 30).

[58] NuNano®. *SPARK 70 Pt - Conductive AFM probe — NuNano AFM Probes — nunano.com*. `https://www.nunano.com/store/spark-70-pt`. [Accessed 11-06-2024] (cited on page 30).

[59] David Nečas and Petr Klapetek. 'Gwyddion: an open-source software for SPM data analysis'. In: *Central European Journal of Physics* 10 (1 2012), pp. 181–188. DOI: `10.2478/s11534-011-0096-2` (cited on page 30).

[60] V. A. Epanechnikov. 'Non-Parametric Estimation of a Multivariate Probability Density'. In: *Theory of Probability & Its Applications* 14.1 (1969), pp. 153–158. DOI: `10.1137/1114019` (cited on page 31).

[61] Nobuyuki Otsu. 'A Threshold Selection Method from Gray-Level Histograms'. In: *IEEE Transactions on Systems, Man, and Cybernetics* 9.1 (1979), pp. 62–66. DOI: `10.1109/TSMC.1979.4310076` (cited on page 32).

[62] Stefan Van der Walt et al. 'scikit-image: image processing in Python'. In: *PeerJ* 2 (2014), e453 (cited on page 32).

[63] Jason S. Haukoos and Roger J. Lewis. 'Advanced Statistics: Bootstrapping Confidence Intervals for Statistics with "Difficult" Distributions'. eng. In: *Academic emergency medicine* 12.4 (2005), pp. 360–365 (cited on page 33).

[64] F. Pedregosa et al. 'Scikit-learn: Machine Learning in Python'. In: *Journal of Machine Learning Research* 12 (2011), pp. 2825–2830 (cited on page 33).

[65] Jiali He et al. 'Non-Destructive Tomographic Nanoscale Imaging of Ferroelectric Domain Walls'. In: *Advanced Functional Materials* (Feb. 2024). DOI: `10.1002/adfm.202314011` (cited on pages 37, 47).

[66] Elise Ramleth Østli. *Optimization of Chemical Composition of Novel Manganite Oxides for Oxygen Permeable Membranes*. Master's thesis. Trondheim, Norway, June 2015 (cited on pages 41, 59).

[67] Outi Parkkima et al. 'New $R\mathrm{MnO}_{3+\delta}$ (R=Y, Ho; $\delta \approx 0.35$) phases with modulated structure'. In: *Journal of Solid State Chemistry* 221 (2015), pp. 109–115. DOI: `https://doi.org/10.1016/j.jssc.2014.09.012` (cited on page 43).

[68] J. Li et al. 'Ferroelectric annular domains in hexagonal manganites'. In: *Phys. Rev. B* 87 (9 Mar. 2013), p. 094106. DOI: `10.1103/PhysRevB.87.094106` (cited on page 45).

[69] Zibin Chen et al. 'Manipulation of Nanoscale Domain Switching Using an Electron Beam with Omnidirectional Electric Field Distribution'. In: *Phys. Rev. Lett.* 117 (2 July 2016), p. 027601. DOI: `10.1103/PhysRevLett.117.027601` (cited on page 45).

[70] Erik D. Roede et al. 'Contact-free reversible switching of improper ferroelectric domains by electron and ion irradiation'. In: *APL Materials* 9.2 (Feb. 2021), p. 021105. DOI: `10.1063/5.0038909` (cited on pages 45, 46).

[71] Xueyun Wang et al. 'Self-poling with oxygen off-stoichiometry in ferroelectric hexagonal manganites'. In: *APL Materials* 3.4 (Feb. 2015), p. 041505. DOI: `10.1063/1.4908159` (cited on page 45).

[72] Olav W. Sandvik et al. 'Pressure Control of Nonferroelastic Ferroelectric Domains in ErMnO3'. In: *Nano Letters* 23.15 (Aug. 2023), pp. 6994–7000. DOI: `10.1021/acs.nanolett.3c01638` (cited on page 47).

[73] Leonie Richarz. 'in prep'. In: (2024) (cited on pages 49, 54).

[74] I. Stolichnov et al. 'Persistent conductive footprints of 109° domain walls in bismuth ferrite films'. In: *Applied Physics Letters* 104.13 (Mar. 2014), p. 132902. DOI: `10.1063/1.4869851` (cited on page 49).

[75] Lukas Kuerten et al. 'Local control of improper ferroelectric domains in YMnO_3'. In: *Phys. Rev. B* 102 (9 Sept. 2020), p. 094108. DOI: `10.1103/PhysRevB.102.094108` (cited on page 50).

[76] Jie Yin et al. 'Nanoscale bubble domains with polar topologies in bulk ferroelectrics'. In: *Nature Communications* 12.1 (June 2021), p. 3632. DOI: `10.1038/s41467-021-23863-w` (cited on pages 52, 53).

[77] A. K. Yadav et al. 'Observation of polar vortices in oxide superlattices'. In: *Nature* 530.7589 (Feb. 2016), pp. 198–201. DOI: `10.1038/nature16463` (cited on page 52).

[78] Feng-Hui Gong et al. 'Absence of critical thickness for polar skyrmions with breaking the Kittel's law'. In: *Nature Communications* 14.1 (June 2023), p. 3376. DOI: `10.1038/s41467-023-39169-y` (cited on page 52).

[79] S. Prokhorenko et al. 'Motion and teleportation of polar bubbles in low-dimensional ferroelectrics'. In: *Nature Communications* 15.1 (Jan. 2024), p. 412. DOI: `10.1038/s41467-023-44639-4` (cited on page 52).

[80] Qi Zhang et al. 'Nanoscale Bubble Domains and Topological Transitions in Ultrathin Ferroelectric Films'. In: *Advanced Materials* 29.46 (2017), p. 1702375. DOI: `https://doi.org/10.1002/adma.201702375` (cited on page 52).

[81] Vivasha Govinden et al. 'Stability of ferroelectric bubble domains'. In: *Phys. Rev. Mater.* 7 (1 Jan. 2023), p. L011401. DOI: `10.1103/PhysRevMaterials.7.L011401` (cited on page 52).

[82] Vivasha Govinden et al. 'Ferroelectric solitons crafted in epitaxial bismuth ferrite superlattices'. In: *Nature Communications* 14.1 (July 2023), p. 4178. DOI: `10.1038/s41467-023-39841-3` (cited on page 52).

[83] Yu-Tsun Shao et al. 'Emergent chirality in a polar meron to skyrmion phase transition'. In: *Nature Communications* 14.1 (Mar. 2023), p. 1355. DOI: `10.1038/s41467-023-36950-x` (cited on page 53).

[84] Yu Kumagai and Nicola A. Spaldin. 'Structural domain walls in polar hexagonal manganites'. In: *Nature Communications* 4.1 (Feb. 2013), p. 1540. DOI: `10.1038/ncomms2545` (cited on page 53).

APPENDIX

Appendix A: Supplementary Figures

A.1 Supplementary cAFM scans

This section presentes cAFM images used for the summary in Figure 5.2. The scans are shown in an order going from top to bottom, and left to right.

A.1.1 400 °C for 24 Hours

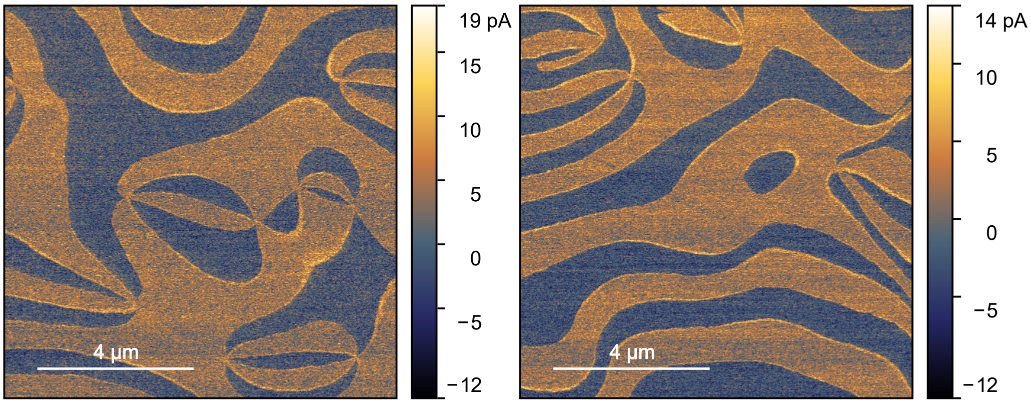

Figure A.1: Post-annealing cAFM scan of sample 245, which was annealed at 400 °C for 24 hours. The domain walls are conductive. The scans were taken using diamond coated silicon tips (DEP01) and with 4 V bias voltage applied to the back electrode.

A.1.2 300 °C for 12 Hours

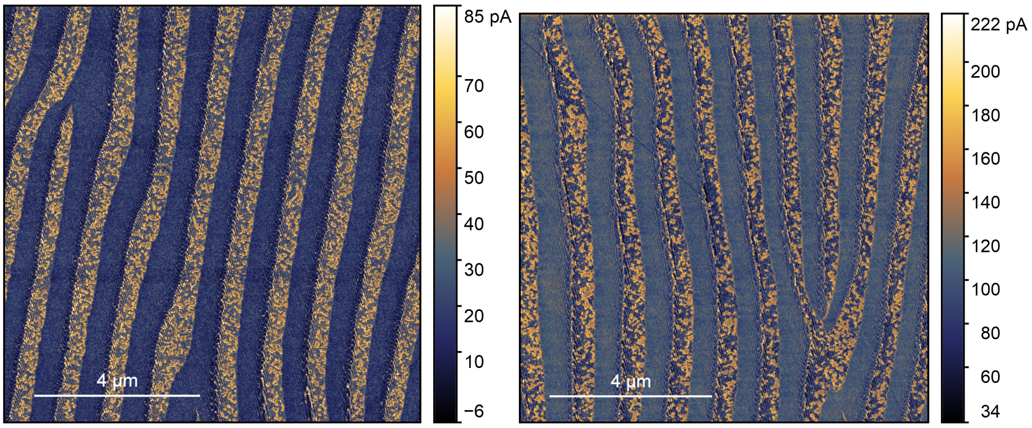
85 pA
70
60
50
40
30
20
10
−6
4 µm
222 pA
200
180
160
140
120
100
80
60
34
4 µm

Figure A.2: Post-annealing cAFM scan of sample 278, which was annealed at 300 °C for 12 hours. The sample exhibits a high number of bubble domains which are encircled by conductive domains walls. The scans were taken using diamond coated silicon tips (DEP01) and with 2 V (left) and 5 V (right) bias voltages applied to the back electrode.

A.1.3 300 °C for 24 Hours

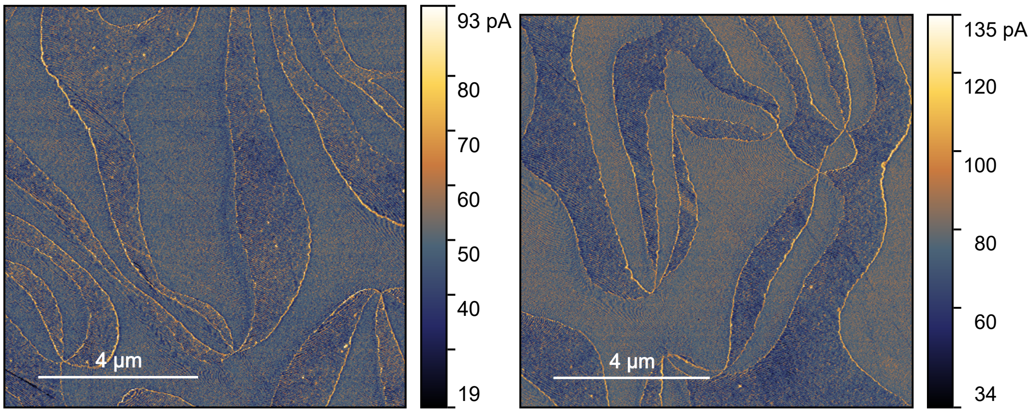
93 pA
80
70
60
50
40
19
4 µm
135 pA
120
100
80
60
34
4 µm

Figure A.3: Post-annealing cAFM scan of sample 242, which was annealed at 300 °C for 24 hours. The domain walls are conductive. The scans were taken using diamond coated silicon tips (DEP01) and with 3 V (left) and 4 V (right) bias voltages applied to the back electrode.

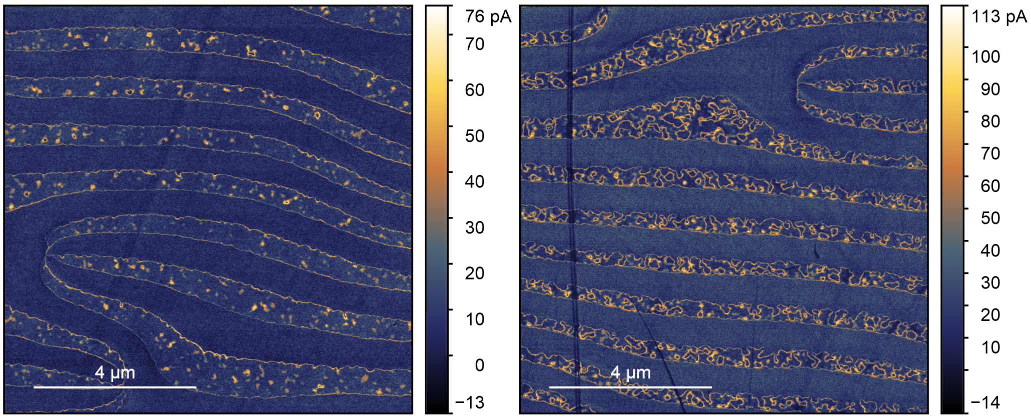
4 µm
76 pA
70
60
50
40
30
20
10
0
−13
4 µm
113 pA
100
90
80
70
60
50
40
30
20
10
−14

Figure A.4: Post-annealing cAFM scan of sample 276, which was annealed at 300 °C for 24 hours. The domain walls are conductive, and the sample has developed a variety of bubble domain morphologies depending on the scan location on the surface. The scans were taken using diamond coated silicon tips (DEP01) and with 2 V (left) and 3 V (right) bias voltages applied to the back electrode.

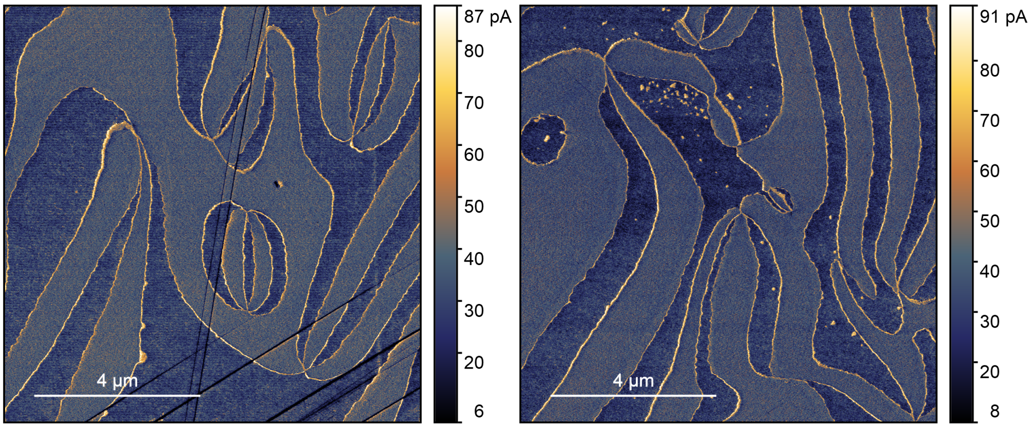
4 µm
87 pA
80
70
60
50
40
30
20
6
4 µm
91 pA
80
70
60
50
40
30
20
8

Post-annealing cAFM scan of sample 277, which was annealed at 300 °C for 24 hours. The domain walls are conductive, and a small amount of bubble domains was observed. The scans were taken using diamond coated silicon tips (DEP01) and with a 3 V bias voltages applied to the back electrode.

A.1.4 300 °C for 48 Hours

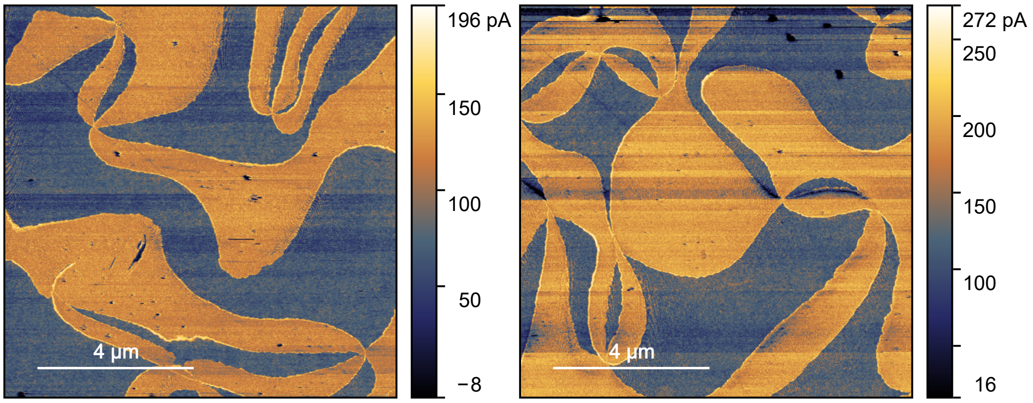
4 µm
196 pA
150
100
50
−8
4 µm
272 pA
250
200
150
100
16

Figure A.5: Post-annealing cAFM scan of sample 240, which was annealed at 300 °C for 48 hours. The domain walls are conductive. The scans were taken using diamond coated silicon tips (DEP01) and with 3 V (left) and 5 V (right) bias voltages applied to the back electrode.

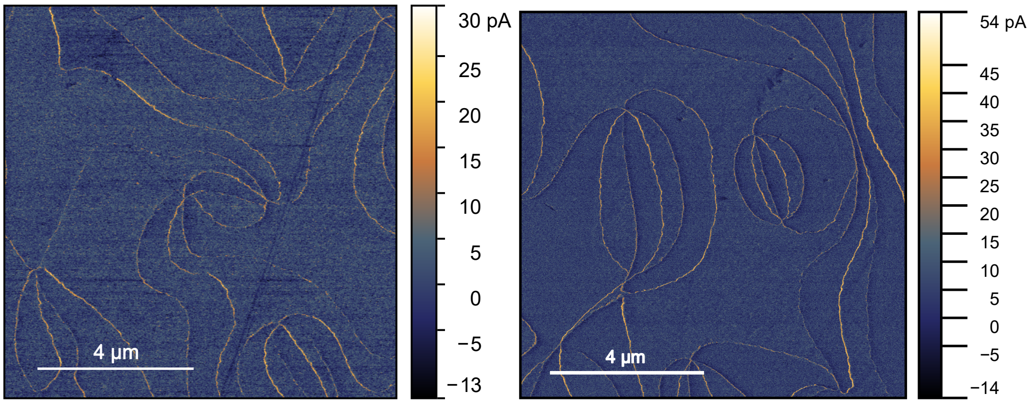
4 µm
30 pA
25
20
15
10
5
0
−5
−13
4 µm
54 pA
45
40
35
30
25
20
15
10
5
0
−5
−14

Figure A.6: Post-annealing cAFM scan of sample 273, which was annealed at 300 °C for 48 hours. The domain walls are conductive. The scans were taken using diamond coated silicon tips (DEP01) and with 3 V (left) and 4 V (right) bias voltages applied to the back electrode.

A.1.5 200 °C for 24 Hours

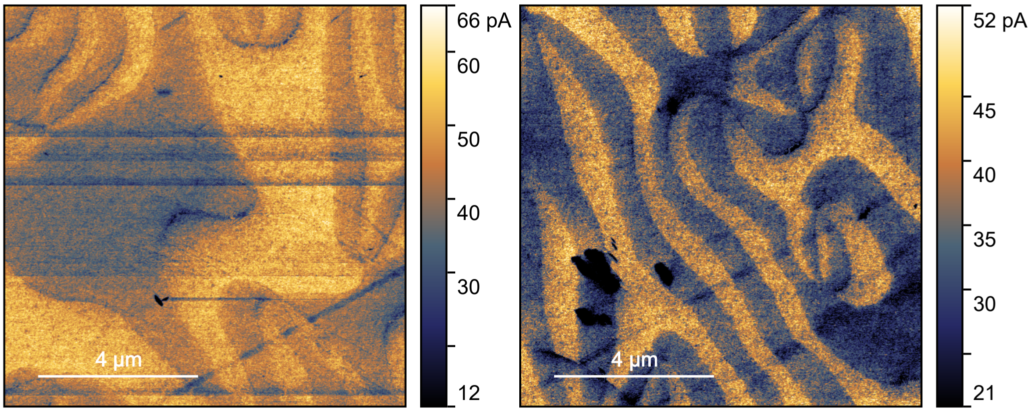
66 pA
60
50
40
30
12
4 µm
52 pA
45
40
35
30
21
4 µm

Figure A.7: Post-annealing cAFM scan of sample 246, which was annealed at 200 °C for 24 hours. The domain walls are not conductive. The scans were taken using diamond coated silicon tips (DEP01) and with a 2 V bias voltages applied to the back electrode.

A.1.6 200 °C for 48 Hours

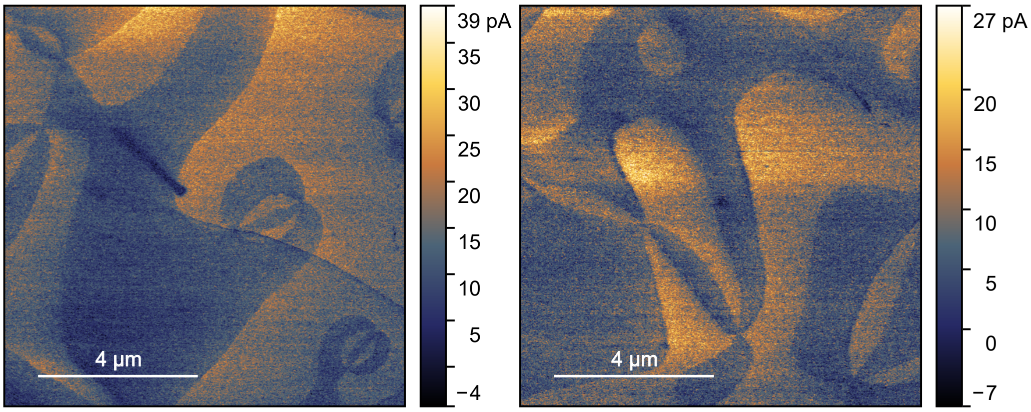
39 pA
35
30
25
20
15
10
5
−4
4 µm
27 pA
20
15
10
5
0
−7
4 µm

Figure A.8: Post-annealing cAFM scan of sample 261, which was annealed at 200 °C for 48 hours. The domain walls are not conductive. The scans were taken using diamond coated silicon tips (DEP01) and with a 2 V bias voltages applied to the back electrode.

A.2 Subsequent Annealings

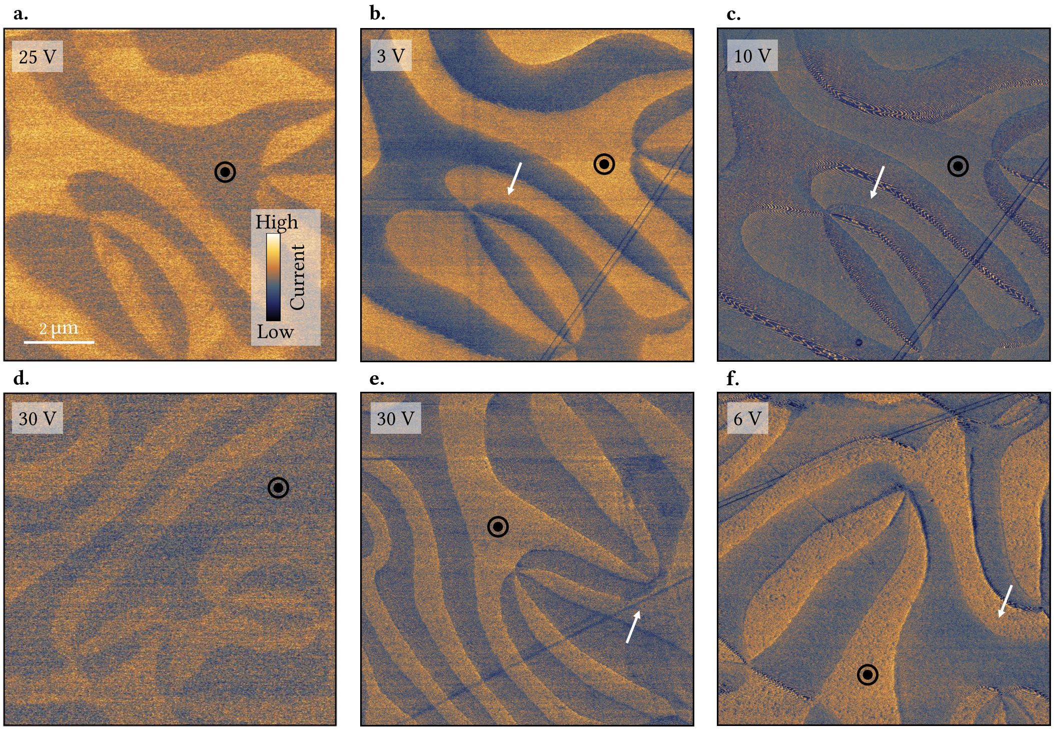

Figure A.9: cAFM scans series of subsequent annealing experiments of two separate samples. Scans **a** and **d** are taken pre-annealing, **b** and **c** are taken after annealing at 200 °C for 24 hours, and **c** and **f** are taken after a subsequent annealing at 300 °C for 24 hours. The scans were taken using diamond tips (CDT-NCHR, a) and diamond coated silicon tips (DEP01, b-f) and with the bias voltages applied to the back electrode. *Reprinted from my specialization thesis [55]*

A.3 Schottky Contrast between Domains

The following figures are additional data for Section 6.2.2, showing the increase in Schottky contrast between domain for additional samples.

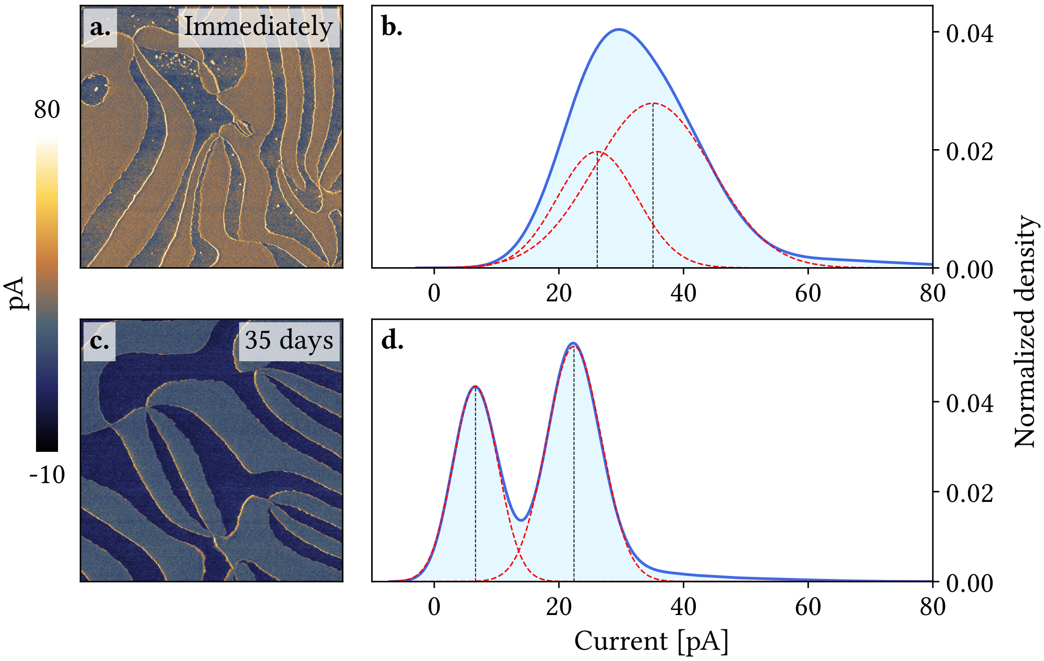

Figure A.10: cAFM scans and corresponding current histograms of a sample acquired at different times after the original annealing. **a-b.** Immeaditely after annealing. **c-d.** 35 days after annealing. The histograms are fitted with two Gaussian functions to represent the two dominant populations of each scan. The peak of each Gaussian curve is marked with a black dotted line. The images have dimensions $10 \times 10\ \mu m^2$ and were acquired using a diamond coated silicon tip (DEP01) and with a 3 V bias voltage applied to the back electrode.

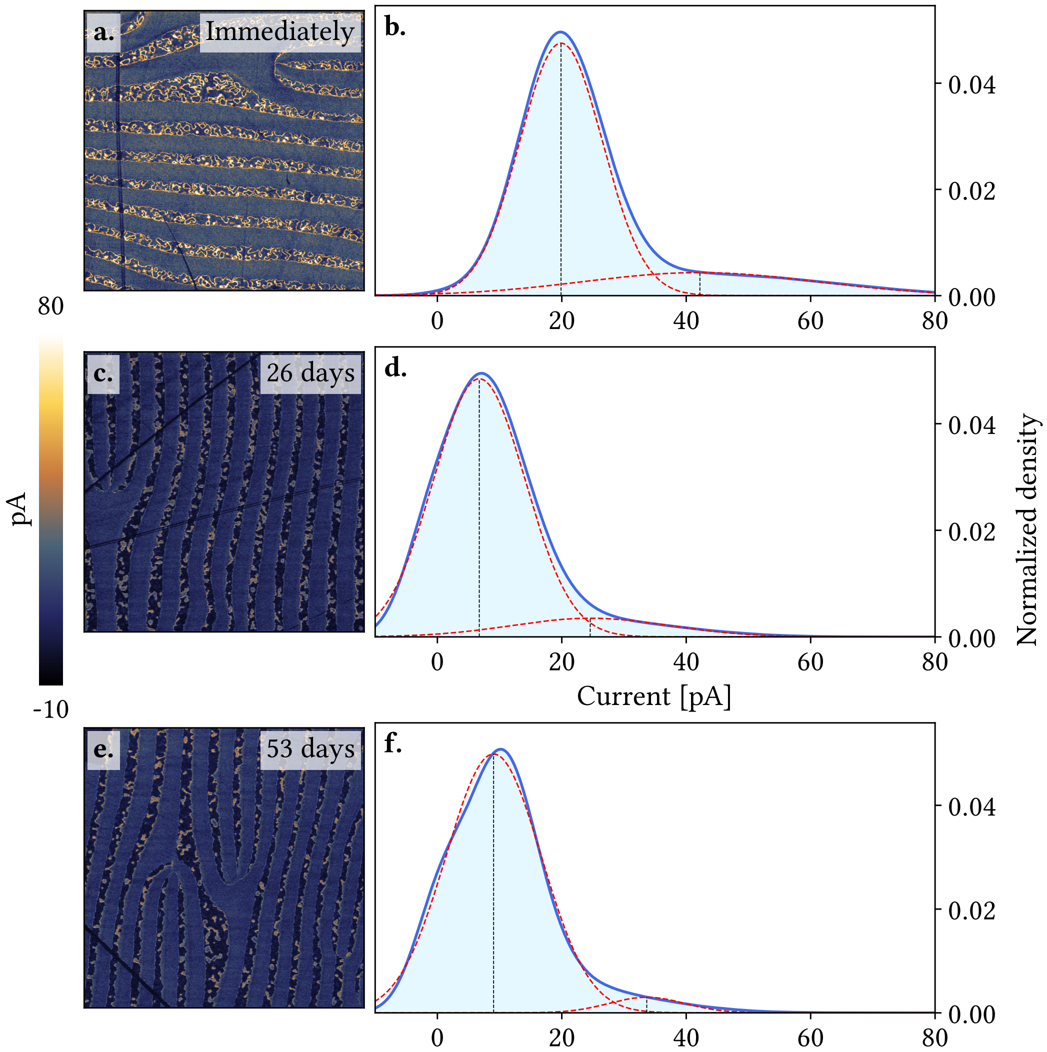

Figure A.11: cAFM scans and corresponding current histograms of a sample acquired at different times after the original annealing. **a-b.** Immeaditely after annealing. **c-d.** 26 days after annealing. **e-f.** 53 days after annealing. The histograms are fitted with two Gaussian functions to represent the two dominant populations of each scan. However, although the Schottky contrast in this scan series is visible to eye, it can not be inferred from the current histograms, and the Gaussian fit rather identified the contribution from the domain as a dominant contribution in all scans. The peak of each Gaussian curve is marked with a black dotted line. The images have dimensions 10×10 µm^2 and were acquired using a diamond coated silicon tip (DEP01) and with a 3 V bias voltage applied to the back electrode.

Appendix B: Scientific Communication

During the work on this project, I have had the opprtunity to participate in several scientific conferences. In two of these I have presented posters with my own work. These posters are included here in this section.

The first poster was presented at the Norwegian NanoSymposium in Trondheim November 28th 2023, and includes a summary of my project thesis. These results are also included in Appendix A.1 and A.2

The second poster was presented at the German Physical Society's (DPG, Deutsche Physikalische Gesellschaft) spring meeting on March 25th 2024. The presentation was part of the division of Crystalline Solids and their Microstructure (KFM, Kristalline Festkörper und deren Mikrostruktur). This poster covered the findings presented in Chapter 5 if this thesis.

Finally, the abstract used for both poster persentations is included.

Oxygen-driven Nano-Engineering for Functional Ferroelectric Domain Walls

Egil Ytterli Tokle[1], Leonie Richarz[1], Edith Bourret[2], Zewu Yan[2,3], and Dennis Meier[1]

[1] NTNU Norwegian University of Science and Technology, Department of Materials Science and Engineering, Trondheim, Norway
[2] Lawrence Berkeley National Laboratory, Berkeley, CA, USA
[3] ETH Zürich, Zürich, Switzerland

egilyt@stud.ntnu.no

Concept Overview and Goal

Ferroelectric Domain Walls

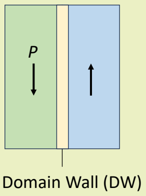

Conductive Atomic Force Microscopy (cAFM)

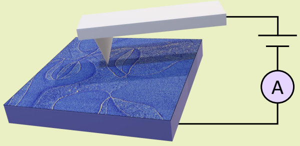

Oxygen Defects and DW Conductance[1]

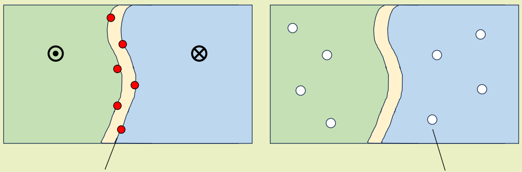

Oxygen Interstitials
→ Enhanced DW conductance

Oxygen Vacancies
→ Reduced DW conductance

- DW conductance in $ErMnO_3$ is shown to be enhanced by annealing in reducing atmosphere (e.g. N_2).[2]
- *This study*: Investigate the effect of annealing temperature and dwell time on DW conductance.

Temperature Dependence

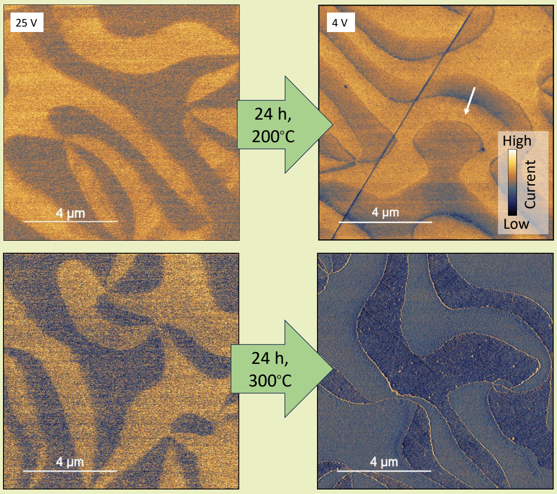

- 200°C: Anisotropically insulating DWs
- 300°C: Conductive DWs
- Both: Required voltage needed for current contrast is significantly reduced

Subsequent Annealings

- Annealings performed on an already annealed sample do not yield the same result as on an unannealed sample.

- 200°C: Same as above
- 300°C: No conductive DWs
  - Moiré effects are strongly enhanced.

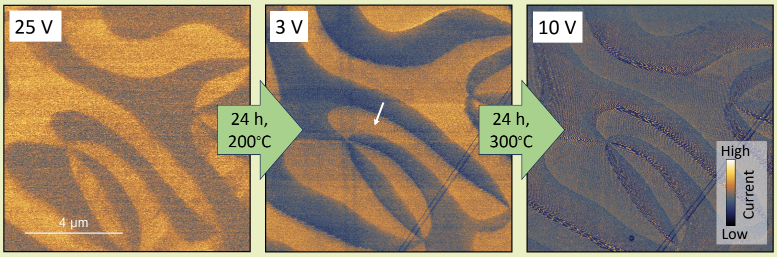

Dwell Time Dependence

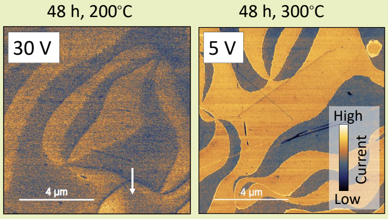

- Dwell time has little qualitative effect on the DW conductance after a certain limit.

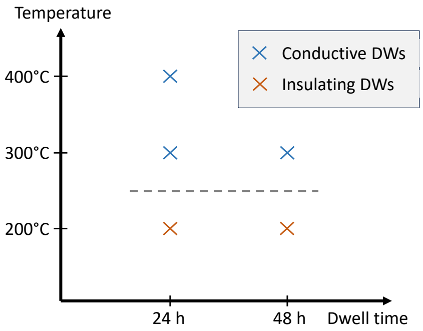

---

[1] Schultheiß et al., 2020, Appl. Phys. Lett., 116, 262903
[2] Richarz et al. in preparation

Interplay between Defects and Ferroelectric Domain Wall Properties

Egil Ytterli Tokle[1], Leonie Richarz[1], Edith Bourret[2], Zewu Yan[2,3], and Dennis Meier[1]

[1] NTNU Norwegian University of Science and Technology, Department of Materials Science and Engineering, Trondheim, Norway
[2] Lawrence Berkeley National Laboratory, Berkeley, CA, USA
[3] ETH Zurich, Zurich, Switzerland

egilyt@stud.ntnu.no

Introduction

- Neutral ferroelectric domain walls (DWs) are promising candidates for novel electronic devices due to their unique conduction properties and small size.
- In $ErMnO_3$, the conductance of these DWs can be tuned by **annealing**.
- Previous studies have shown that annealing can reversably change the DW conductance from insulating to conducting.[1]
- The changes are attributed to **oxygen defects** accumulating or depleting at the DW.

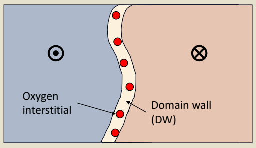

Oxygen interstitials aggregate at the domain wall.

⬇

Enhanced DW conductance[2]

---

[1] Richarz et al. *in preparation*
[2] Schultheiß et al., *Appl. Phys. Lett.*, **116**, 262903 (2020)

Controlling DW Conductance by Annealing

As grown:

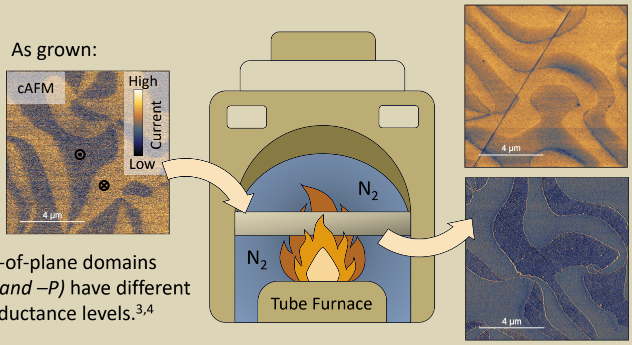

Out-of-plane domains *(+P and –P)* have different conductance levels.[3,4]

***200 °C**, 24 h:*
Insulating DWs

***300 °C**, 24 h:*
Conductive DWs

---

[3] Wu et al. *Phys. Rev. Lett.* **104**, 217601 (2010)
[4] Meier et al., *Nature Materials* **11**, 284–288 (2012)

Preferred Reoxidation of Neutral Domain Walls

- Annealings performed on an already annealed sample do not yield the same result as on an as-grown sample.

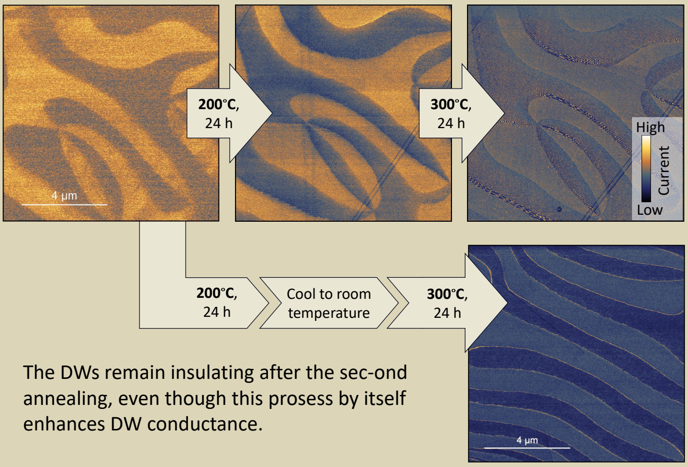

- The DWs remain insulating after the sec-ond annealing, even though this prosess by itself enhances DW conductance.
- However, performing the same two annealings while **continuously** keeping the sample in N_2 gives enhanced DW conductance, as is expected for the second annealing.

Hypothesis:

- Oxygen concentration is reduced universally throughout the sample.
- DWs **reoxidize** when exposed to air after annealing.

The hypothesis is consistent with reduced potential energy for oxygen interstitials at neutral DWs predicted by DFT.[2,5]

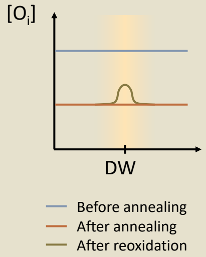

---

[2] Schultheiß et al., *Appl. Phys. Lett.*, **116**, 262903 (2020)
[5] Skjærvø et al., *Nat Commun* **7**, 13745 (2016)

Effect of Self-Poling

- Domains can **self-pole** during annealing due to an electric field induced by the oxygen concentration gradient at the surface.[6]

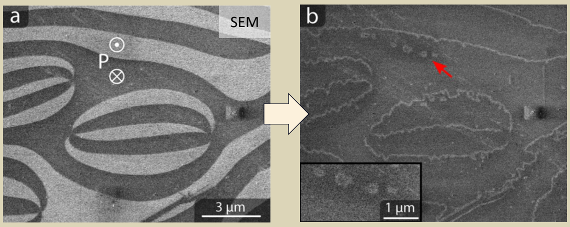

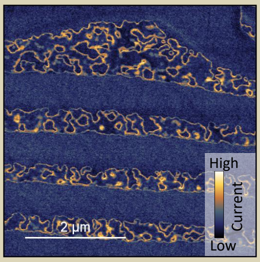

- The conductance follows the path of the **new** DW when poling occurs during the annealing process.
- This supports the reoxidation hypo-thesis, where conductance appears after the movement of the DWs.

---

[6] Wang et al., *APL Mater.* **3**, 041505 (2015)

Conclusion

- Changing the **defect chemistry** of the samples can significantly change the domain wall conductance
- Enhanced domain wall conductance after annealing in N_2 at 300 °C is likely caused by **reoxidation** of the domain walls after the annealing.
- Annealing experiments allow to tune the conductance of neutral domain walls in $ErMnO_3$ and provide insight into the underlying defect chemistry.

NTNU Norwegian University of Science and Technology

FACET

Contribution submission to the conference Berlin 2024

Interplay between Defects and Ferroelectric Domain Wall Properties — Egil Y. Tokle[1], Leonie Richarz[1], Edith Bourret[2], Zewu Yan[2,3], and Dennis Meier[1] — [1]NTNU Norwegian University of Science and Technology, Trondheim, Norway — [2]Lawrence Berkeley National Laboratory, Berkeley, CA, USA — [3]ETH Zurich, Switzerland

Ferroelectric domain walls are natural interfaces separating volumes with different orientation of the spontaneous polarization. These walls can display fundamentally different conduction properties than the surrounding material. For instance, the conductance at domain walls in hexagonal manganites can range from insulating to highly conducting relative to the ferroelectric domains. Interestingly, the transport behavior correlates with the oxygen off-stoichiometry of the system. In previous studies, we observed that annealing in reducing atmosphere can significantly increase the relative domain wall conductance.

In this work, we systematically study the influence of different annealing parameters – such as annealing temperature and dwell time – and monitor the impact on the electronic transport behavior of domain walls $Er(Mn,Ti)O_3$, using conducting atomic force microscopy. Our results provide new insights into the underlying microscopic mechanisms and give detailed guidelines for property engineering at the level of the domain walls.

Part:	**KFM**
Type:	**Poster**
Topic:	**Focus: (Multi)ferroic states: From interfaces to heterostructures**
Email:	**egilyt@stud.ntnu.no**

Appendix C: Bubble Domain Paper

The work on the bubble domains presented in Chapter 6 has also been compiled into a paper format, which I have been working on in parallel with the thesis. The paper is titled *"Generation and Control of Nanoscal Improper Ferroelectric Bubble Domains"*, and we hope to be able to publish it by the end of the year. In this appendix, I present the latest draft of the paper. Please keep in mind that the following is still a rough draft in the early stages of writing, and we will continue to work on it after the completion of the thesis.

Generation and Control of Nanoscale Improper Ferroelectric Bubble-Domains

Egil Ytterli Tokle,[1] Leonie Richarz,[1] Ruben Dragland,[1] Zewu Yan,[2, 3] Edith Bourret,[3] and Dennis Meier[1]
[1] *Department of Material Sciences and Engineering, Norwegian University of Science and Technology (NTNU), Trondheim, Norway*
[2] *ETH Zurich, Zurich, Switzerland*
[3] *Lawrence Berkeley National Laboratory, Berkeley, CA, USA*

(Dated: 13 June 2024)

Lorem ipsum dolor sit amet, consectetuer adipiscing elit. Ut purus elit, vestibulum ut, placerat ac, adipiscing vitae, felis. Curabitur dictum gravida mauris. Nam arcu libero, nonummy eget, consectetuer id, vulputate a, magna. Donec vehicula augue eu neque. Pellentesque habitant morbi tristique senectus et netus et malesuada fames ac turpis egestas. Mauris ut leo. Cras viverra metus rhoncus sem. Nulla et lectus vestibulum urna fringilla ultrices. Phasellus eu tellus sit amet tortor gravida placerat. Integer sapien est, iaculis in, pretium quis, viverra ac, nunc. Praesent eget sem vel leo ultrices bibendum. Aenean faucibus. Morbi dolor nulla, malesuada eu, pulvinar at, mollis ac, nulla. Curabitur auctor semper nulla. Donec varius orci eget risus. Duis nibh mi, congue eu, accumsan eleifend, sagittis quis, diam. Duis eget orci sit amet orci dignissim rutrum.

I. INTRODUCTION

Ferroelectric nanoscale bubble domains have attracted increasing attention in recent years[1–10]. Typically, bubbles are accompanied by complex topological structures that combine both Néel and Bloch characteristics, such as polar skyrmions, bimerons[1] and hopfions[3]. The topologies are stabilized by the low-dimensional environments of thin films[6–8] and high-quality heterostructures[1,2,4,5,9] that allow for better control over the ferroelectricity and depolarization fields. In addition, bubble domains have been reported to form even in bulk ferroelectrics[10]. Such bubbles are movable in electric fields[7], and a range of applications is suggested similarly to their more intensely studied magnetic counterparts.

... interesting spatially memristive behaviour, and possible applications in multiferroic topotronics.

However, all this work has been conducted on proper ferroelectrics. We now show a similar phenomenon in $\mathrm{ErMnO_3}$, expanding the field to improper ferroelectrics. Furthermore, this work provides insight into the migration behavior of the domain walls and the extrinsic transport mechanisms.

For this, we use the hexagonal manganite $\mathrm{Er(Mn,Ti)O_3}$ as a model system. In this improper ferroelectric, the uniaxial polarization arises as a secondary effect from a structural position. As a consequence, $\mathrm{Er(Mn,Ti)O_3}$ exhibits an unusual domain structure, with the domain walls meandering between topologically protected vortex points[11].

II. BUBBLE DOMAINS

We start by investigation the as-grown domain structure of the material. Conventionally, piezoresponce force microscopy (PFM) is a common technique for studying the domain structure of ferroelectrics. Figure 1(a) shows the ferroelectric domain structure of $\mathrm{ErMnO_3}$ with different contrast in the two domains due to the polarization direction dependent piezoresponse of the material. Alternatively, conducting atomic microscopy can give similar information about the domain structure with polarization normal to the surface. Figure 1(b) shows a cAFM scan of the same area as in Figure 1(a), where the domain contrast is created by altered Schottky barriers induced by the out-of-plane component of the polarization. Besides providing a domain contrast that can be correlated to the polarization direction, cAFM also reveals the electrical characteristics of the domain walls, with conductive and insulating walls appearing brighter and darker than the surrounding domains, respectively.

Annealing the sample to induce conductivity in the domain walls allows for easier detection of nanoscale domain features, which are accentuated by these domain walls.

Such domain features include bubble domains that appear in the up domain, as shown in Figure 1(c). A well-documented effect in the hexagonal manganites is the self-poling of domains on the surface from electric fields induced by a concentration gradient of charges. This effect can result from deviations in oxygen stoichiometry after undergoing chemical reduction or oxidation processes. When the material is annealed in a reducing $\mathrm{N_2}$ atmosphere, the surface concentration of oxygen ions decreases as oxygen exits the material, which in turn generates a downward directed electric field toward the bulk[12]. Depending on the initial off-stoichiometry of the sample, this field can reach a magnitude sufficient to alter the ferroelectric polarization of the surface up domain. Such domain growth driven by self-poling is primarily driven by two basic mechanisms: movement of the already present domain wall, and nucleation of new domains (as in Figure 1(c)). These bubble domains are visible as dots or loops of conductive domain walls filled with an area with similar contrast to the opposite domain. With this, we have a perfect model system to study bubble domains and their conductive properties in cAFM.

The formation of these bubble domains does not show any correlation with the annealing temperature or dwell time used to enhance the domain wall conduction, and is

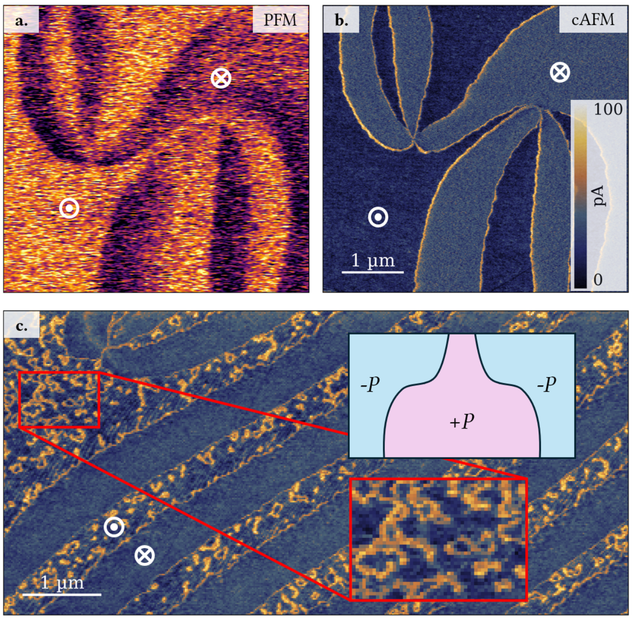

FIG. 1. (a) Vertical PFM image of out-of-plane ferroelectric domains in $ErMnO_3$. The direction of the ferroelectric domains are indicated. (b) cAFM image of the same area as (a), showing domain contrast as well as conduction state of the ferroelectric domain walls. (c) cAFM scan showing bubble domains induced by reductive annealing. The inset shows a schematic of the underlying domain structure after poling of the surface, as presented in ref.[12]. The PFM scan was taken using a platinum-coated silicon tip (Spark 70 Pt). The cAFM scans were taken using diamond coated silicon tips (DEP01) and with a 3 V (a) and 4 V (b) bias voltage applied to the back electrode.

likely actuated by other factors. Electronic interactions on the ferroelectric surface are significantly influenced by the morphology of subsurface domain walls[13,14], and the domain architecture of $ErMnO_3$ is modulated by externally applied mechanical pressures[15]. We suggest that a combination of the underlying domain structure, crystal strain, and chemistry of the sample is the primary driving force determining the specific mechanism for annealing-induced self-poling of the ferroelectic domains. However, it is important to note that this suggestion remains speculative in the absence of direct experimental evidence.

III. STABILITY OF BUBBLE DOMAINS

To investigate the stability of the emergent bubble domains, we study a sample with cAFM at various times after the initial annealing. The resulting cAFM scans are visible in Figures 2(a-d). For better visibility, the down domain (not containing any bubble domains) is grayed out. From inspecting the images, we see a reduction in the surface fraction of the bubble domains with time. To quantify this decrease, in Figure 2(e) we show the current distribution of the up domains of each scan. To effectively quantify the extent of the bubble domains, a metric is defined by employing the Otsu thresholding algorithm[16] to separate the distribution of current values into the domain and domain wall contribution. The distributions are categorized into two classes using a threshold that maximizes the inter-class variance of the two sides, with the higher class representing the conductive domain walls associated with the bubble domains. In the histograms in Figure 2(e), the contribution identified as bubble domains is visually distinguished with a lighter overlay. Moreover, the area under the curve serves as a metric to quantify the percentage of the domain covered by bubble domains. Figure 2(f) shows the partition of surface area between the bubble domains and the background domain over time with error bars obtained using a bootstrapping algorithm, confirming the decrease in area covered by the bubble domains. As such, the bubble domains are shown to be metastable, and are not bounded by a topological protection present in proper ferroelectric bubble domains.

This effect can be explained by the reoxidation of the sample after annealing. After being reexposed to ambient conditions following a reducing annealing, the material will gradually revert towards the original defect chemistry in the preannealed state by absorbing oxygen from the air. As the material is refilled with oxygen ions, the electric field induced by the ionic concentration gradient at the surface is neutralized, destabilizing the bubble domain. Consequently, the spatial prevalence of the bubble domains is reduced.

In addition, the overall conduction of the sample is reduced over time, affecting both the background domain and the domain walls of the bubble domains. Figure 2(g) shows the average current values of the four scans, with means and uncertainties for the background domain and the domain walls associated with the bubble domains. The values are extracted from first- and second-order critical values of the distribution curves in Figure 2(e) on the basis of similar mathematical properties in the normal distribution function. Besides enhancing domain wall conductance, reductive annealing in N_2 has the additional effect of increasing the overall conductance of the material, which can be attributed to the lower concentration of oxygen ions[17]. The reduction in sample conductance can hence be considered as part of the reversal back to the defect chemistry of the preannealed state as the material reoxidizes after a sufficient amount of time.

A key characteristic of bubble domains laying the basis for this discussion is that the enhanced conductance at the domain walls vanishes concurrently with the domain walls themselves. Given that the heightened conductance at the neutral domain walls is associated with an increase in the number of negative charge carriers donated by oxygen interstitial ions[17], the passivation of the conductance necessarily suggests the simultaneous movement of oxygen defects with the domain walls. This demonstrates

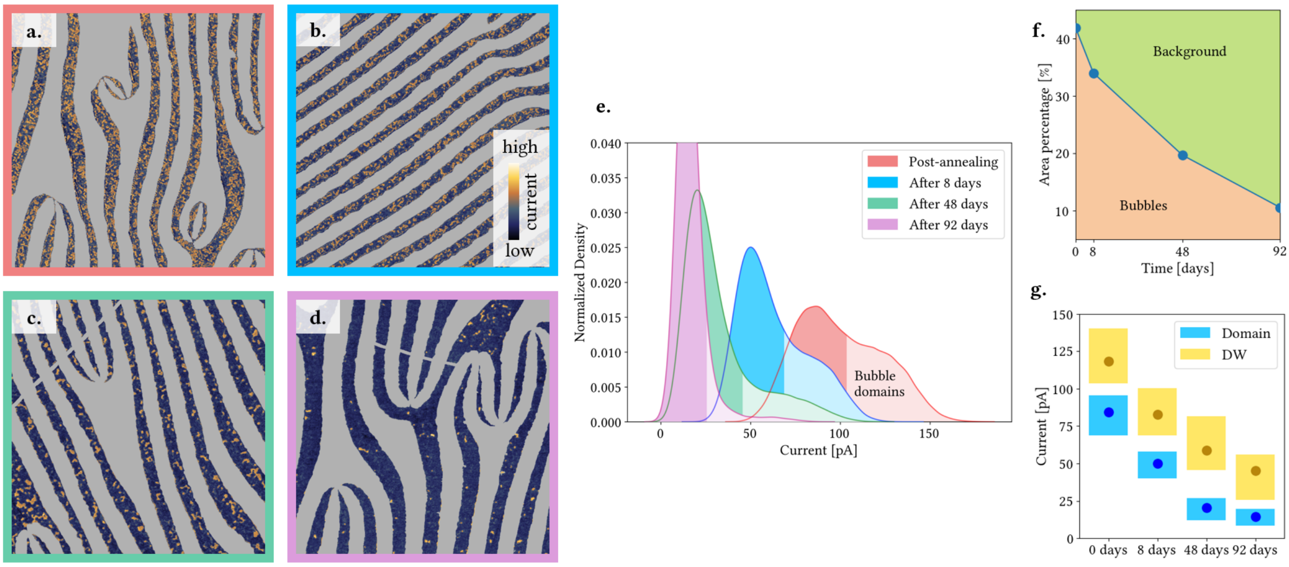

FIG. 2. (a-d) cAFM images of bubble domains in the up domain taken at various times after the initial annealing. The down domain has been removed from the data (gray areas). The images have dimensions 10 × 10 µm^2 and were acquired using a diamond coated silicon tip (DEP01) and with a 4 V bias voltage applied to the back electrode. (e) Fitted current distributions of the data in (a)-(d), with colors corresponding to the edge color of the respective scan. The curves are separated into two segments by treating the current values with the Otsu thresholding algorithm. Higher current values are associated with the domain walls surround the bubble domains. The sections representing the bubble domains are highlighted in a lighter color. (f) Spatial coverage of bubble domains decreases as a function of time. (g) Current values of the domains and domain walls extracted from the distributions in (e) for the different scans. Both the background domain and the domain walls show a reduction in conductivity over time.

the remarkable mobility of oxygen defects in the material even at room temperature[18], allowing the defects to move with the domain walls, which is less probable in other ferroelectrics[19]. As such, the walls of the neutral domain act as anchor points for oxygen defects, which then disperse throughout the material once they are no longer confined by the domain wall.

IV. CONTROL OF BUBBLE DOMAINS

In a next step, we attempt to actively manipulate the bubble domains by applying electric fields. As these emerge from an electric field gradient, it is expected that their number can be reduced by external electric fields counteracting the internal field. Previous works have been able to successfully control the surface ferroelectric domain structure of hexagonal manganites by exposing the material to electron radiation in scanning electron microscopy (SEM)[20] and transmission electron microscopy (TEM)[21,22], and ion radiation in a focused ion beam (FIB)[23]. Scanning probe techniques present another approach to local domain control[24].

We create an external electric field in the sample using cAFM, applying a bias voltage to the back electrode. The direction of this field points out from the material, antiparallel to the polarization of the bubble domains. After performing a scan over an area, we can study the impact of the applied bias in subsequent scans. Figure 3(a-b) shows two scans taken 27 days apart. The bubble domains present in the first scan (Figure 3(b)) have mostly disappeared in the latter scan (Figure 3(a), whil the primary domain structure remains intact. In comparison, the neighboring pristine area in the latter scan still exhibits a rich pattern of bubble domains, similar to the area in the former scan. The absolute current values are not comparable between Figure 3(a) and (b), as the scans are taken using different biases.

In contrast, Figure 3(c) compares cAFM data of a pristine area with an area subjected to external bias immediately prior to the scan. In this case, the overall sample conductance is reduced similarly to the previous case, however, the bubble domains are present to a similar extent to the pristine area. As such, the degradation of bubble domains is not directly caused by, but is rather accelerated by the application of external electric fields. This demonstrates a spatially and temporally memristive behavior of the bubble domains, wherein the conductance of the sample informs on the spatial extent of the applied electric fields, while the concentration of bubble domains provides insights into the temporal dimension.

For further investigation, data from the pristine and scanned regions were consolidated into the current distributions depicted in Figure 3(d). The graphs are similar to the ones shown in Figure 2(e), however, as we now draw current values from both domains, two peaks are

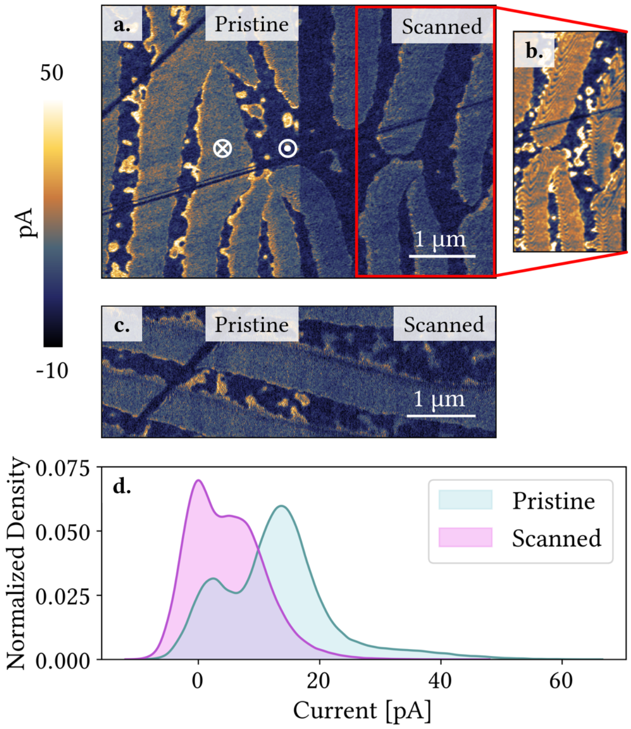

FIG. 3. (a) cAFM image containing two distinct halves: one pristine region not previously affected by external electric fields (left), and one area over which a cAFM scan has been performed at a previous date (right). Notably, the previously scanned area has lower conduction in both domains and domain walls and fewer bubble domains than the pristine area. (b) Pristine cAFM image of the scanned area in (a), taken 27 days prior. (c) cAFM image of a pristine area and an area scanned immediately prior. The images were taken using diamond coated silicon tips (DEP01) and with 3 V (a, c) and 4 V (b) bias voltages applied to the back electrode. (d) Density of current values from the two regions in (a).

apparent in the distributions, one for each domain, and with the size of each peak decided by the spatial coverage of the two domains. The impact of applying an external electric field mirrors that of letting the sample dwell in ambient conditions, creating narrower peaks centered at lower current values and with less pronounced tails at higher current values representing conductive domain walls.

Our results reveal an exceptional flexibility for manipulation of the bubble domains, and further experiments were conducted to map the possibilities to a greater extent. Figure 4(a) shows a cAFM scan with a progressively increasing voltage over the horizonthal axis from left to right, enabling the examination of the immediate effects of the applied voltage. Naturally, a higher bias enhances the current flow through the sample, manifesting as a darker color on the left and a brighter color on the right. The conduction contrast between the up and down domains inverts in the transition from low to high bias voltage, attributed to a shift in conduction mechanism between the two regimes, as reported in Ref.[25].

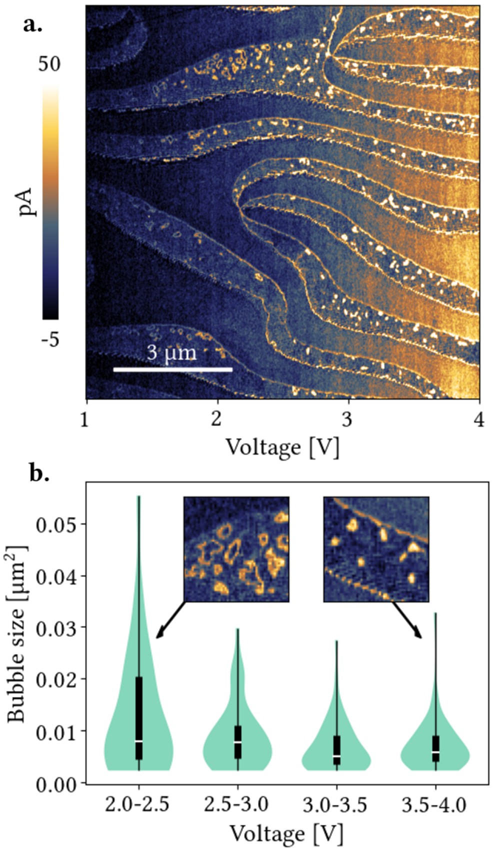

FIG. 4. Reduction of bubble domain size with increased scan bias. (a) cAFM scan with increasing bias voltage from 1 V to 4 V with evenly spaced increments of 0.1 V. The scan is performed using diamond coated silicon tips (DEP01) and with the voltage applied from the back electrode. (b) Violin plot of the bubble domain size distribution, with the median and interquartile range marked in white and a thicker central line respectively. The insets exemplify the domains found in the respective bins and show an area of 1 × 1 µm^2. A threshold of six pixels was set to eradicate contributions from noise. The sample size is $n \approx 50$ for all bins.

The bubble domains demonstrate a remarkable shift in morphology as the bias increases: at lower scan biases, the bubbles surface mostly as domain wall rings with a visible interior; while at higher biases, the bubbles are smaller and dominated by the domain wall conductance. To quantify this, we partition the scan into four regions, and present the sizes of each region in violin plot in Figure 4(b). The thickness of each violin presents the size distribution of the bubble domains of each population. The areas between 1 V and 2 V were excluded from this measurement due to the inefficiency of thresholding in the low contrast regime. The bulk of the distributions are situated closely together, with the tails extending upwards of the lower biases being significantly more pronounced.

V. CONCLUSION

In summary, we have demonstrated the appearance of bubble domains in improper ferroelectric $\mathrm{Er(Mn,Ti)O_3}$. The bubble domains demonstrate a memristive behavior with respect to previous applied bias voltages with both temporal and spatial aspects. **...**

VI. EXPERIMENTAL METHODS

High quality $\mathrm{ErMn_{1-x}Ti_xO_3}$ ($x = 0.002$) was grown using the pressurized floating zone method[26]. The crystal was oriented by Laue diffraction and cut along the [001] crystal plane, so that the polarization ($P \parallel c$) is perpendicular to the surface. The crystal was lapped and polished to achieve a high-quality surface with a topographical variation of up to ∼20 nm. To modify the domain wall conductance, the samples were annealed in N_2 at 300 °C with dwell times ranging from 12 h to 48 h. The heating and cooling rates were kept constant at $200\,^{\circ}\mathrm{C\,h^{-1}}$.

...SPM (Cypher, NT-MDT)

REFERENCES

[1] V. Govinden, P. Tong, X. Guo, Q. Zhang, S. Mantri, M. M. Seyfouri, S. Prokhorenko, Y. Nahas, Y. Wu, L. Bellaiche, T. Sun, H. Tian, Z. Hong, N. Valanoor, and D. Sando, "Ferroelectric solitons crafted in epitaxial bismuth ferrite superlattices," Nature Communications **14**, 4178 (2023).

[2] V. Govinden, S. Rijal, Q. Zhang, Y. Nahas, L. Bellaiche, N. Valanoor, and S. Prokhorenko, "Stability of ferroelectric bubble domains," Phys. Rev. Mater. **7**, L011401 (2023).

[3] V. Govinden, S. Prokhorenko, Q. Zhang, S. Rijal, Y. Nahas, L. Bellaiche, and N. Valanoor, "Spherical ferroelectric solitons," Nature Materials **22**, 553–561 (2023).

[4] Q. Zhang, L. Xie, G. Liu, S. Prokhorenko, Y. Nahas, X. Pan, L. Bellaiche, A. Gruverman, and N. Valanoor, "Nanoscale bubble domains and topological transitions in ultrathin ferroelectric films," Advanced Materials **29**, 1702375 (2017), https://onlinelibrary.wiley.com/doi/pdf/10.1002/adma.201702375.

[5] F.-H. Gong, Y.-L. Tang, Y.-J. Wang, Y.-T. Chen, B. Wu, L.-X. Yang, Y.-L. Zhu, and X.-L. Ma, "Absence of critical thickness for polar skyrmions with breaking the kittel's law," Nature Communications **14**, 3376 (2023).

[6] A. K. Yadav, C. T. Nelson, S. L. Hsu, Z. Hong, J. D. Clarkson, C. M. Schlepütz, A. R. Damodaran, P. Shafer, E. Arenholz, L. R. Dedon, D. Chen, A. Vishwanath, A. M. Minor, L. Q. Chen, J. F. Scott, L. W. Martin, and R. Ramesh, "Observation of polar vortices in oxide superlattices," Nature **530**, 198–201 (2016).

[7] S. Prokhorenko, Y. Nahas, V. Govinden, Q. Zhang, N. Valanoor, and L. Bellaiche, "Motion and teleportation of polar bubbles in low-dimensional ferroelectrics," Nature Communications **15**, 412 (2024).

[8] Y. Nahas, S. Prokhorenko, Q. Zhang, V. Govinden, N. Valanoor, and L. Bellaiche, "Topology and control of self-assembled domain patterns in low-dimensional ferroelectrics," Nature Communications **11**, 5779 (2020).

[9] S. Das, Y. L. Tang, Z. Hong, M. A. P. Gonçalves, M. R. McCarter, C. Klewe, K. X. Nguyen, F. Gómez-Ortiz, P. Shafer, E. Arenholz, V. A. Stoica, S.-L. Hsu, B. Wang, C. Ophus, J. F. Liu, C. T. Nelson, S. Saremi, B. Prasad, A. B. Mei, D. G. Schlom, J. Íñiguez, P. García-Fernández, D. A. Muller, L. Q. Chen, J. Junquera, L. W. Martin, and R. Ramesh, "Observation of room-temperature polar skyrmions," Nature **568**, 368–372 (2019).

[10] J. Yin, H. Zong, H. Tao, X. Tao, H. Wu, Y. Zhang, L.-D. Zhao, X. Ding, J. Sun, J. Zhu, J. Wu, and S. J. Pennycook, "Nanoscale bubble domains with polar topologies in bulk ferroelectrics," Nature Communications **12**, 3632 (2021).

[11] T. Choi, Y. Horibe, H. T. Yi, Y. J. Choi, W. Wu, and S.-W. Cheong, "Insulating interlocked ferroelectric and structural antiphase domain walls in multiferroic $\mathrm{YMnO_3}$," Nature Materials **9**, 253–258 (2010).

[12] X. Wang, F.-T. Huang, R. Hu, F. Fan, and S.-W. Cheong, "Self-poling with oxygen off-stoichiometry in ferroelectric hexagonal manganites," APL Materials **3**, 041505 (2015), https://pubs.aip.org/aip/apm/article-pdf/doi/10.1063/1.4908159/14557383/041505_1_online.pdf.

[13] J. He, M. Zahn, I. Ushakov, L. Richarz, U. Ludacka, E. Roede, Z. Yan, E. Bourret, I. Kézsmárki, G. Catalan, and D. Meier, "Non-destructive tomographic nanoscale imaging of ferroelectric domain walls," Advanced Functional Materials (2024), 10.1002/adfm.202314011.

[14] E. D. Roede, K. Shapovalov, T. J. Moran, A. B. Mosberg, Z. Yan, E. Bourret, A. Cano, B. D. Huey, A. T. J. van Helvoort, and D. Meier, "The third dimension of ferroelectric domain walls," Advanced Materials **34**, 2202614 (2022), https://onlinelibrary.wiley.com/doi/pdf/10.1002/adma.202202614.

[15] O. W. Sandvik, A. M. Müller, H. W. Ånes, M. Zahn, J. He, M. Fiebig, T. Lottermoser, T. Rojac, D. Meier, and J. Schultheiß, "Pressure control of nonferroelastic ferroelectric domains in $\mathrm{ErMnO_3}$," Nano Letters **23**, 6994–7000 (2023).

[16] N. Otsu, "A threshold selection method from gray-level histograms," IEEE Transactions on Systems, Man, and Cybernetics **9**, 62–66 (1979).

[17] L. Richarz, "in prep," (2024).

[18] E. R. Østli, "Optimization of chemical composition of novel manganite oxides for oxygen permeable membranes," (2015).

[19] I. Stolichnov, M. Iwanowska, E. Colla, B. Ziegler, I. Gaponenko, P. Paruch, M. Huijben, G. Rijnders, and N. Setter, "Persistent conductive footprints of 109° domain walls in bismuth ferrite films," Applied Physics Letters **104**, 132902 (2014), https://pubs.aip.org/aip/apl/article-pdf/doi/10.1063/1.4869851/14293409/132902_1_online.pdf.

[20] J. Li, H. X. Yang, H. F. Tian, S.-W. Cheong, C. Ma, S. Zhang, Y. G. Zhao, and J. Q. Li, "Ferroelectric annular domains in hexagonal manganites," Phys. Rev. B **87**, 094106 (2013).

[21] M.-G. Han, Y. Zhu, L. Wu, T. Aoki, V. Volkov, X. Wang, S. C. Chae, Y. S. Oh, and S.-W. Cheong, "Ferroelectric switching dynamics of topological vortex domains in a hexagonal manganite," Advanced Materials **25**, 2415–2421 (2013), https://onlinelibrary.wiley.com/doi/pdf/10.1002/adma.201204766.

[22] Z. Chen, X. Wang, S. P. Ringer, and X. Liao, "Manipulation of nanoscale domain switching using an electron beam with omnidirectional electric field distribution," Phys. Rev. Lett. **117**, 027601 (2016).

[23] E. D. Roede, A. B. Mosberg, D. M. Evans, E. Bourret, Z. Yan, A. T. J. van Helvoort, and D. Meier, "Contact-free reversible switching of improper ferroelectric domains by electron and ion irradiation," APL Materials **9**, 021105 (2021), https://pubs.aip.org/aip/apm/article-pdf/doi/10.1063/5.0038909/13783633/021105_1_online.pdf.

[24] L. Kuerten, S. Krohns, P. Schoenherr, K. Holeczek, E. Pomjakushina, T. Lottermoser, M. Trassin, D. Meier, and M. Fiebig, "Local control of improper ferroelectric domains in $\mathrm{ymno_3}$," Phys. Rev. B **102**, 094108 (2020).

[25] W. Wu, J. R. Guest, Y. Horibe, S. Park, T. Choi, S.-W. Cheong, and M. Bode, "Polarization-modulated rectification at ferroelectric surfaces," Phys. Rev. Lett. **104**, 217601 (2010).

[26] Z. Yan, D. Meier, J. Schaab, R. Ramesh, E. Samulon, and E. Bourret, "Growth of high-quality hexagonal ermno3 single crystals by the pressurized floating-zone method," Journal of

Crystal Growth **409**, 75–79 (2015).

[27] D. Meier, J. Seidel, A. Cano, K. Delaney, Y. Kumagai, M. Mostovoy, N. A. Spaldin, R. Ramesh, and M. Fiebig, “Anisotropic conductance at improper ferroelectric domain walls,” Nature Materials **11**, 284–288 (2012).

[28] S. Ghara, K. Geirhos, L. Kuerten, P. Lunkenheimer, V. Tsurkan, M. Fiebig, and I. Kézsmárki, “Giant conductivity of mobile non-oxide domain walls,” Nature Communications **12**, 3975 (2021).

[29] J. Schultheiß, J. Schaab, D. R. Småbråten, S. H. Skjærvø, E. Bourret, Z. Yan, S. M. Selbach, and D. Meier, “Intrinsic and extrinsic conduction contributions at nominally neutral domain walls in hexagonal manganites,” Applied Physics Letters **116**, 262903 (2020), https://pubs.aip.org/aip/apl/article-pdf/doi/10.1063/5.0009185/14533060/262903_1_online.pdf.

[30] W. Wu, Y. Horibe, N. Lee, S.-W. Cheong, and J. R. Guest, “Conduction of topologically protected charged ferroelectric domain walls,” Phys. Rev. Lett. **108**, 077203 (2012).

[31] I. Stolichnov, L. Feigl, L. J. McGilly, T. Sluka, X.-K. Wei, E. Colla, A. Crassous, K. Shapovalov, P. Yudin, A. K. Tagantsev, and N. Setter, “Bent ferroelectric domain walls as reconfigurable metallic-like channels,” Nano Letters **15**, 8049–8055 (2015).

[32] S. C. Chae, N. Lee, Y. Horibe, M. Tanimura, S. Mori, B. Gao, S. Carr, and S.-W. Cheong, “Direct observation of the proliferation of ferroelectric loop domains and vortex-antivortex pairs,” Phys. Rev. Lett. **108**, 167603 (2012).

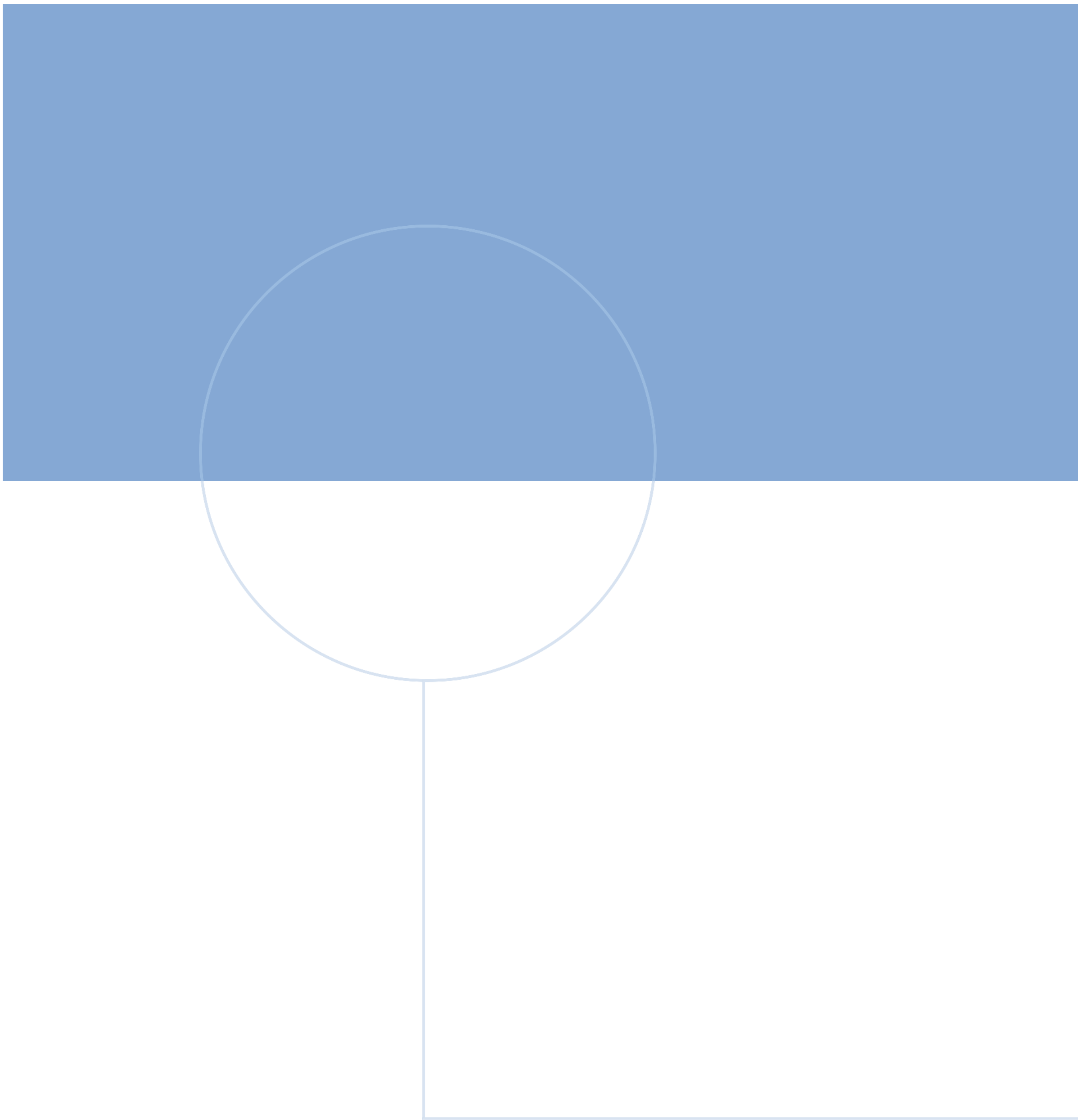

NTNU

Norwegian University of
Science and Technology